Indexed in: EMBASE/Excerpta Medica,
SciELO, BIBLAT, MIAR, DOAJ,
ASCI-Database, Latindex
Preserved in: CLOCKSS

JMeXFRI

Journal of the Mexican Federation of Radiology and Imaging

J Mex Fed Radiol Imaging

Volume 5. Number 1, January-March 2026
ISSN: 2938-1215
eISSN: 2696-8444

PERMANYER
www.permanyer.com

Official Journal of the

FEDERACIÓN MEXICANA DE RADIOLOGÍA E IMAGEN, A.C

WWW.JMeXFRI.COM

JMeXFRI

Journal of the Mexican Federation of Radiology and Imaging

J Mex Fed Radiol Imaging

Volume 5. Number 1, January-March 2026

ISSN: 2938-1215

eISSN: 2696-8444

The *Journal of the Mexican Federation of Radiology and Imaging* (JMeXFRI) is the official journal of the Federacion Mexicana de Radiologia e Imagen. The aim of the journal is to disseminate scientific knowledge and technological developments for innovation in diagnostic and therapeutic radiology with original articles on basic and clinical aspects of modern radiology in an international context with global impact. JMeXFRI is published in American English with 4 issues per year (print and online) and the first issue was published in the first quarter of 2022. Articles undergo a rigorous, double-blind peer-review process. Publication of articles in JMexFRI is free of charge and all published articles are open access.

The journal publishes the following types of manuscripts: *Full Research Article, Pictorial Essay, Brief Research Article, Technical Note, In-Depth Review, Case Report, Images in Radiology, and Editorial.*

EDITORIAL BOARD

EDITOR-IN-CHIEF

Mauricio Figueroa-Sanchez, M.D.
Department of Imaging, Hospital Angeles Andares. Zapopan, Jal., Mexico

ASSOCIATE EDITORS

Gerardo E. Ornelas-Cortinas, M.D.
Centro Universitario de Imagen Diagnostica, Hospital Universitario "Dr. Jose E. Gonzalez", Monterrey, N.L., Mexico

Araceli Cue-Castro, M.D.
Turnitin - iThenticate Evaluation, JMeXFRI, Mexico City, Mexico

Martha M. Ruiz-Ballesteros, M.D., M.Sc.
Radiology Department, Hospital Joya, Guadalajara, Jal., Mexico

Beatriz Gonzalez-Ulloa, M.D.
Department of Breast Imaging, Diagnostico Especializado por Imagen, Guadalajara, Jal., Mexico

Ana M. Contreras-Navarro, M.D., M.Sc., Ph.D.
Scientific Writing Workshop, JMeXFRI, Zapopan, Jal., Mexico

David Garza-Cruz, M.D.
Department of Radiology, Hospital Angeles, Torreon, Coah., Mexico

J. Mario Bernal-Ramirez, M.D.
Department of Medical Clinics, Centro Universitario de Ciencias de la Salud, Universidad de Guadalajara, Guadalajara, Jal., Mexico

Dante R. Casale-Menier, M.D.
Department of Radiology and Imaging, Hospital Angeles, Ciudad Juarez, Chih., Mexico

SCIENTIFIC TRANSLATOR EDITOR

Sergio Lozano-Rodriguez, M.D.
Research Office of the Vice Dean, Hospital Universitario "Dr. Jose E. Gonzalez", Monterrey, N.L., Mexico

Arturo Hernandez-Medina, Ph.D.
Department of Magnetic Resonance Imaging, Angeles Lomas Hospital, Huixquilucan, State of Mexico, Mexico

BIOSTATISTICS ADVISERS

Cesar N. Cristancho-Rojas, M.D., M.Sc.
School of Public Health, Oregon Health & Science University, Portland, OR., USA

Arturo Hernandez-Medina, Ph.D.
Department of Magnetic Resonance Imaging Angeles Lomas Hospital, Huixquilucan State of Mexico, Mexico

DESIGN ADVISER

Jorge Mendez-Palacios, B.Sc.
Design Area, JMeXFRI. Zapopan, Jal., Mexico

NATIONAL EDITORIAL BOARD

HEAD AND NECK RADIOLOGY

Mario A. Campos-Coy, M.D.
Centro Universitario de Imagen Diagnostica,
Hospital Universitario "Dr. Jose E. Gonzalez",
Monterrey, N.L., Mexico

Eduardo D. Sarda-Inman, M.D.
Diagnostico Especializado por Imagen,
Zapopan, Jal., Mexico

GASTROINTESTINAL RADIOLOGY

Araceli Cue-Castro, M.D.
Department of Computed Tomography,
Hospital General "Dr. Enrique Cabrera" SEDESA,
Mexico City, Mexico

Adrian Negreros-Osuna, M.D., Ph.D.
Departamento de Radiologia,
Hospital Regional ISSSTE Monterrey,
Monterrey, N.L., Mexico

Oscar A. Chavez-Barba, M.D.
Department of Radiology,
Antiguo Hospital Civil de Guadalajara
"Fray Antonio Alcalde",
Guadalajara, Jal., Mexico

Martha M. Ruiz-Ballesteros, M.D., M.Sc
Radiology Department, Hospital Joya,
Guadalajara, Jal., Mexico

OBSTETRIC AND GYNECOLOGIC RADIOLOGY

Dante R. Casale-Menier, M.D.
Department of Radiology and Imaging,
Hospital Angeles,
Ciudad Juarez, Chih., Mexico

Roberto J. Carrales-Cuellar, M.D.
Department of Ecographic Diagnosis,
Radiologia Especializada,
Guadalajara, Jal., Mexico

BREAST RADIOLOGY

David F. Perez-Montemayor, M.D.
General Direction,
Centro de Imagenologia Integral IMAX,
Tampico, Tamps., Mexico

Beatriz Gonzalez-Ulloa, M.D.
Department of Breast Imaging,
Diagnostico Especializado por Imagen,
Guadalajara, Jal., Mexico

Margarita L. Garza-Montemayor, M.D.
Departamento de Imagen Diagnostica,
Centro de Cancer de Mama,
Hospital Zambrano Hellion, Tec Salud,
Monterrey, N.L., Mexico

Karla M. Nuñez-Barragan, M.D.
Women's Imaging Department,
Doctors Hospital East Auna
Monterrey, N. L., Mexico

Yazmin A. Ramirez-Galvan, M.D., Ph.D.
Breast Imaging Section
Department of Radiology and Imaging,
University Hospital
"Dr. Jose Eleuterio Gonzalez"
Monterrey, N.L. Mexico

NUCLEAR AND MOLECULAR MEDICINE

Hugo E. Solis-Lara, M.D.
Centro de Imagen Molecular,
Hospital Christus Muguerza Alta Especialidad,
Monterrey, N.L., Mexico

NEURORADIOLOGY

Jorge Paz-Gutierrez, M.D.
Department of Magnetic Resonance,
Centro Medico Puerta de Hierro,
Zapopan, Jal., Mexico

Azalea Garza-Baez, M.D.
Department of Radiology and Imaging,
Hospital Zambrano Hellion, Tecnologico de Monterrey,
Monterrey, N.L., Mexico

Perla M. Salgado-Lujambio, M.D.
Direccion de Enseñanza, Instituto Nacional
de Neurologia y Neurocirugia "Manuel Velasco Suarez"
Mexico City, Mexico

Rebeca de J. Ramos-Sanchez, M.D.
Department of Neuroimaging, Instituto Nacional
de Neurologia y Neurocirugia "Manuel Velasco Suarez"
Mexico City, Mexico

PEDIATRIC RADIOLOGY

Aida Perez-Lara, M.D.
Department of Radiology, Hospital Español,
Mexico City, Mexico

Martha M. Ruiz-Ballesteros, M.D., M.Sc
Radiology Department, Hospital Joya,
Guadalajara, Jal., Mexico

MUSCULOSKELETAL RADIOLOGY

Oscar A. Chavez-Barba, M.D.
Department of Radiology, Antiguo Hospital Civil
de Guadalajara "Fray Antonio Alcalde",
Guadalajara, Jal., Mexico

J. Francisco Diaz-Fernandez, M.D.
Department of Radiology,
Hospital General "Agustin O'Horan",
Merida, Yuc., Mexico

CHEST AND CARDIOVASCULAR RADIOLOGY

Sergio A. Criales-Vera, M.D.
Department of Radiology and Imaging,
Instituto Nacional de Cardiologia "Ignacio Chavez",
Mexico City, Mexico

Harold Goerne, M.D.
Department of Radiology, Hospital de Pediatria,
Instituto Mexicano del Seguro Social,
Guadalajara, Jal., Mexico

Luis F. Alva-Lopez, M.D.
Department of Radiology, Hospital Medica Sur,
Mexico City, Mexico

GENITOURINARY RADIOLOGY

Sergio B. Peregrina-Gonzalez, M.D.
Consultorio de Imagen,
Guadalajara, Jal., Mexico

Araceli Cue-Castro, M.D.
Department of Computed Tomography,
Hospital General
"Dr. Enrique Cabrera" SEDESA,
Mexico City, Mexico

Adrian Negreros-Osuna, M.D.
Departamento de Radiologia,
Hospital Regional ISSSTE Monterrey,
Monterrey, N.L., Mexico

Benjamin Conde-Castro, M.D.
Faculty of Medicine,
Universidad Nacional Autónoma de Mexico,
Mexico City, Mexico

ULTRASOUND

Victor M. Rodriguez-Peralta, M.D.
Department or Radiology,
Fundacion de Cancer de Mama (FUCAM),
Oaxaca, Oax., Mexico

David Garza-Cruz, M.D.
Department of Radiology, Hospital Angeles,
Torreon, Coah., Mexico

Manuel Hernandez-Cruz, M.D.
Area de Ultrasonido,
Unidad de Ultrasonido Diagnostico,
Puebla, Pue. Mexico

VASCULAR AND INTERVENTIONAL RADIOLOGY

Guillermo Elizondo-Riojas, M.D., Ph.D.
Centro Universitario de Imagen Diagnostica,
Hospital Universitario "Dr. Jose E. Gonzalez",
Monterrey, N.L., Mexico

Raul A. De Luna-Vega. M.D.
Centro Universitario de Imagen Diagnostica,
Hospital Universitario "Dr. Jose E. Gonzalez",
Monterrey, N.L., Mexico

ARTIFICIAL INTELLIGENCE

Guillermo Elizondo-Riojas, M.D., Ph.D.
Centro Universitario de Imagen Diagnostica,
Hospital Universitario "Dr. Jose E. Gonzalez",
Monterrey, N.L., Mexico

Adrian Negreros-Osuna, M.D.
Departamento de Radiología,
Hospital Regional ISSSTE Monterrey,
Monterrey, N.L., Mexico

J. Mario Bernal-Ramirez, M.D.
Department of Medical Clinics,
Centro Universitario de Ciencias de la Salud,
Universidad de Guadalajara,
Guadalajara, Jal., Mexico

Benjamin Conde-Castro, M.D.
Faculty of Medicine,
Universidad Nacional Autonoma de México,
Mexico City, Mexico

JUNIOR EDITORIAL BOARD

J. Mario Bernal-Ramirez, M.D.
Department of Medical Clinics,
Centro Universitario de Ciencias de la Salud,
Universidad de Guadalajara,
Guadalajara, Jal., Mexico

Ana K. Luna-Marroquin, M.D.
Centro Universitario de Imagen Diagnostica,
Hospital Universitario "Dr. Jose E. Gonzalez",
Monterrey, N.L., Mexico

M. Lourdes Garcia-Colmenero, M.D.
Departamento de Radiologia,
CID Centro de Imagen y Diagnostico
Guadalajara, Jal., Mexico

Xavier A. Gonzalez-Ballesteros, M.D.
Departamento de Radiologia,
Hospital San Angel Inn Universidad,
Ciudad de Mexico, Mexico

Adriana Parada-Gallardo, M.D.
Department of Radiology,
Hospital General de Zapopan,
Zapopan, Jal., Mexico

A. Sofia Sanchez-Gomez, M.D.
Department of Radiology,
Grupo RIO Centro Integral de Diagnostico Medico
Guadalajara, Jal., Mexico

INTERNATIONAL EDITORIAL BOARD

HEAD AND NECK RADIOLOGY

Richard H. Wiggins, M.D.
Department of Radiology and Imaging Sciences,
School of Medicine, University of Utah,
Salt Lake City, UT., USA

Amy Juliano, M.D.
Department of Radiology, Massachusetts Eye and Ear,
Harvard Medical School,
Boston, MA., USA

GASTROINTESTINAL RADIOLOGY

Luis Martí-Bonmatí, M.D., PH.D.
Grupo de Investigación Biomédica en Imagen (GIBI230)
Instituto de Investigación
Sanitaria La Fe Área Clínica de Imagen Médica,
Hospital Universitario y Politécnico La Fe,
Valencia, Spain

Jorge A. Soto, M.D.
Department of Radiology,
Boston Medical Center,
Boston, MA., USA

Jorge Elias Jr. Ph.D.
Departamento de Imagenes Medicas,
Oncologia e Hematologia,
Faculdade de Medicina Ribeirao Preto,
Universidade Sao Paulo Ribeirao Preto,
Sao Paolo, Brazil

Valdair F. Muglia, M.D.
Faculdade de Medicina de Ribeirão Preto,
Universidade de São Paulo, Ribeirão Preto,
Sao Paolo, Brazil

Carlo Catalano, M.D.
Department of Diagnostic Radiology
La Sapienza University of Rome
Rome, Italy

OBSTETRIC AND GYNECOLOGIC RADIOLOGY

Luciana Pardini Chamie, M.D., Ph.D.
Centro de Diagnostico Ultrasonografico
Especializado en Imagen de la Mujer,
Sao Paolo, Brazil

BREAST RADIOLOGY

Javier Romero-Enciso, M.D.
Department of Radiology,
Fundacion Santa Fe,
Bogota, Colombia

NUCLEAR AND MOLECULAR MEDICINE

Begoña Martinez-Sanchis, M.D.
Department of Nuclear Medicine,
Hospital Universitario y Politecnico La Fe,
Valencia, Spain

Cesar N. Cristancho-Rojas, M.D., M.Sc.
School of Public Health,
Oregon Health & Science University,
Portland, OR., USA

NEURORADIOLOGY

Roy F. Riascos-Castaneda, M.D.
Department of Radiology and Neurosurgery,
Memorial Hermann Hospital System,
Houston, TX., USA

Rafael Rojas-Jasso, M.D.
Department of Radiology, Beth Israel,
Deaconess Medical Center,
Boston, MA., USA

Henrique Carrete Jr., M.D., Ph.D.
Department of Diagnostic Imaging,
Universidad de Sao Paulo,
Sao Paulo, Brazil

Carlos Torres, M.D.
Department of Diagnostic Imaging,
The Ottawa Hospital,
Ottawa, Canada

Carla M. Garcia-Moreno, M.D.
Diagnostic Imaging Department,
Hospital Juravinsky, McMaster University,
Hamilton, Ontario, Canada

Josep Munuera, M.D.
Diagnostic Imaging Department,
Hospital de la Santa Creu i Sant Pau,
Universitat Politecnica de Catalunya,
Barcelona, Spain

MUSCULOSKELETAL RADIOLOGY

Javier Fernandez-Jara, M.D.
Department f Radiology,
Hospital Universitario Sanitas La Zarzuela,
Madrid, Spain

Jose Luis del Cura, M.D.
Radiodiagnosis Service,
Hospital Universitario Donostia,
San Sebastian-Donostia, Spain

Diego F. Lemos, M.D.
Department of Radiology,
University of Vermont Medical Center,
Burlington, VT, USA

PEDIATRIC RADIOLOGY

George Bisset, M.D.
Department of Radiology, Children's Hospital
Pennsylvania, PA., USA

Sara Reis Teixeira, M.D., Ph.D.
Department of Radiology, Children's Hospital
Pennsylvania, PA. USA

CHEST AND CARDIOVASCULAR RADIOLOGY

Fernando R. Gutierrez, M.D.
Department of Radiology and Cardiothoracic Imaging,
The Mallickrodt Institute of Radiology,
St. Louis, MO., USA

Jorge Carrillo-Bayona, M.D.
Department of Radiology,
Hospital Universitario Mayor,
Bogota, Colombia

Carlos S. Restrepo, M.D.
Department of Cardiothoracic Radiology,
Texas University,
San Antonio, TX., USA

Sebastian Rossini, M.D.
Department of Radiology,
Instituto Radiologico Mater Dei,
Buenos Aires, Argentina

Santiago Martinez-Jimenez, M.D.
Department of Radiology,
Saint Luke´s Hospital of Kansas City,
Kansas City, KS., USA

L. Antonio Sosa-Lozano, M.D.
Department of Cardiothoracic Radiology,
Medical College of Wisconsin,
Milwaukee, WI., USA

GENITOURINARY RADIOLOGY

Daniela Stoisa, M.D.
Department of Radiology, Diagnostico Medico Oroño,
Rosario, Santa Fe, Argentina

Valdair F. Muglia, M.D.
Faculdade de Medicina de Ribeirao Preto,
Universidade de Sao Paulo Ribeirao Preto,
Sao Paulo, Brazil

ULTRASOUND

Edward G. Grant, M.D.
Department of Radiology, USC Norris Cancer Center,
Los Angeles, CA., USA

Juan P. Niedmann-Espinosa, M.D.
Department of Ecotomography,
Clinica Alemana de Santiago,
Santiago de Chile, Chile

VASCULAR AND INTERVENTIONAL RADIOLOGY

Manuel Cifrian-Perez, M.D., Ph.D.
Imaging Clinic Department,
Hospital Universitario y Politecnico La Fe,
Valencia, Spain

ARTIFICIAL INTELLIGENCE

Luis Martí-Bonmatí, M.D., Ph.D.
Grupo de Investigación Biomédica en Imagen (GIBI230)
Instituto de Investigación Sanitaria La Fe
Área Clínica de Imagen Médica,
Hospital Universitario y Politécnico La Fe
Valencia, Spain

Leonor Cerda-Alberich, Ph.D
Imaging Clinic Department,
Hospital Universitario y Politecnico La Fe,
Valencia, Spain

Felipe Campos Kitamura, M.D., Ph.D.
Dasalnova, Dasa,
Sao Paulo, Brazil

WEBSITE ADMINISTRATION COMMITTEE

David Garza-Cruz, M.D.
Coordinator, Department of Radiology, Hospital Angeles,
Torreon, Coah., Mexico

Ana Karen Luna-Marroquin, M.D.
Head and Neck Radiology Section
Centro Universitario de Imagen Diagnostica,
Hospital Universitario "Dr. Jose E. Gonzalez",
Monterrey, N.L., Mexico

Hugo E. Solis-Lara, M.D.
Gastrointestinal Radiology Section and Nuclear
And Molecular Medicine Section
Centro de Imagen Molecular,
Hospital Christus Muguerza Alta Especialidad,
Monterrey, N.L., Mexico

Dante R. Casale-Menier, M.D.
Gynecology and Obstetrics Radiology Section
Genitourinary Radiology Section
Department of Radiology and Imaging,
Hospital Angeles,
Ciudad Juarez, Chih., Mexico

Beatriz Gonzalez-Ulloa, M.D.
Breast Radiology Section
Department of Breast Imaging,
Diagnostico Especializado por Imagen,
Guadalajara, Jal., Mexico

Yazmin A. Ramirez-Galvan, M.D., Ph.D.
Breast Radiology Section
Breast Imaging Section
Department of Radiology and Imaging,
University Hospital "Dr. Jose Eleuterio Gonzalez"
Monterrey, N.L. Mexico

Rebeca de J. Ramos-Sanchez, M.D.
Neuroradiology Section
Department of Neuroimaging, Instituto Nacional
de Neurologia y Neurocirugia "Manuel Velasco Suarez"
Mexico City, Mexico

Aida Perez-Lara, M.D.
Pediatric Radiology Section Department of Radiology,
Hospital Español, Mexico City, Mexico

Gerardo E. Ornelas-Cortinas, M.D.
Musculoskeletal Radiology Section
Centro Universitario de Imagen Diagnostica,
Hospital Universitario "Dr. Jose E. Gonzalez",
Monterrey, N.L., Mexico

Cesar N. Cristancho-Rojas, M.D., M.Sc.
Chest and Cardiovascular Radiology Section
School of Public Health,
Oregon Health & Science University,
Portland, OR., USA

J.M. Ignacio Lopez-Mendez, M.D.
Ultrasound Section
Department of Radiology and Imaging,
Hospital de Especialidades, CMNO
Instituto Mexicano del Seguro Social,
Guadalajara, Jal., Mexico.

Mauricio Figueroa-Sanchez, M.D.
Vascular and Interventional Radiology Section
Department of Radiology,
Antiguo Hospital Civil de Guadalajara
"Fray Antonio Alcalde",
Guadalajara, Jal., Mexico

J. Mario Bernal-Ramirez, M.D.
Artificial Intelligence Radiology Section
Department of Medical Clinics,
Centro Universitario de Ciencias de la Salud,
Universidad de Guadalajara,
Guadalajara, Jal., Mexico

Diana Camorlinga-Ornelas, M.D
General Radiology Section, Imaging Department
Hospital General Regional Num. 2
Mexican Social Security Institute
Ciudad Juarez, Chih., Mexico.

GRAPHICAL ABSTRACTS COMMITTEE

Martha M. Ruiz-Ballesteros, M.D., M.Sc
Coordinator, Radiology Department,
Hospital Joya, Guadalajara, Jal., Mexico

Oscar A. Chavez-Barba, M.D.
Department of Radiology,
Antiguo Hospital Civil de Guadalajara
"Fray Antonio Alcalde",
Guadalajara, Jal., Mexico

Adriana Parada-Gallardo, M.D.
Department of Radiology,
Hospital General de Zapopan,
Zapopan, Jal., Mexico

J.M. Ignacio Lopez-Mendez, M.D.
Department of Radiology and Imaging,
Hospital de Especialidades, CMNO
Instituto Mexicano del Seguro Social,
Guadalajara, Jal., Mexico.

Juan Pablo Lopez-Gutierrez, M.D.
Department of Radiology and Imaging,
Hospital General de Zona 3,
Instituto Mexicano del Seguro Social
Aguascalientes, Ags., Mexico

Gerardo Llamas-Linares, M.D.
Centro Universitario de Imagen Diagnostica,
Hospital Universitario "Dr. Jose E. Gonzalez",
Monterrey, N.L., Mexico

Alejandra I. Castillo-Cervantes, M.D.
Centro Universitario de Imagen Diagnostica,
Hospital Universitario "Dr. Jose E. Gonzalez",
Monterrey, N.L., Mexico

A. Sofia Sanchez-Gomez, M.D.
Department of Radiology,
Grupo RIO Centro Integral de Diagnostico Medico,
Guadalajara, Jal., Mexico

SOCIAL MEDIA COMMITTEE

Guillermo Elizondo-Riojas, M.D., Ph.D.
Centro Universitario de Imagen Diagnostica,
Hospital Universitario "Dr. Jose E. Gonzalez",
Monterrey, N.L., Mexico

Oscar A. Chavez-Barba, M.D.
Department of Radiology,
Antiguo Hospital Civil de Guadalajara
"Fray Antonio Alcalde",
Guadalajara, Jal., Mexico

J. Mario Bernal-Ramirez, M.D.
Department of Medical Clinics,
Centro Universitario de Ciencias de la Salud,
Universidad de Guadalajara,
Guadalajara, Jal., Mexico

Adriana Parada-Gallardo, M.D.
Department of Radiology,
Hospital General de Zapopan,
Zapopan, Jal., Mexico

A. Sofia Sanchez-Gomez, M.D.
Department of Radiology,
Grupo RIO Centro Integral de Diagnostico Medico.
Guadalajara, Jal., Mexico

RADIOLOGICAL AND CLINICAL CORRELATION BOARD

GASTROENTEROLOGY

Linda E. Muñoz-Espinosa, M.D., Ph.D.
Liver Unit, Hospital Universitario
"Dr. Jose E. Gonzalez",
Monterrey, N.L., Mexico

David Marti-Aguado, M.D., Ph.D.
Servicio Medicina Digestiva,
Hospital Clinico Universitario,
Valencia, Spain

GASTROINTESTINAL AND GENERAL SURGERY

Carlos Nuño-Guzman, M.D., M.Sc.
Department of Surgery, Antiguo Hospital Civil
de Guadalajara "Fray Antonio Alcalde",
Guadalajara, Jal., Mexico

NEUROLOGY

Jose L. Ruiz-Sandoval, M.D., M.Sc.
Department of Neurology, Antiguo Hospital Civil
de Guadalajara "Fray Antonio Alcalde",
Guadalajara, Jal., Mexico

RHEUMATOLOGY

Monica Vazquez del Mercado-Espinosa, M.D., Ph.D.
Division of Medicine,
Nuevo Hospital Civil de Guadalajara,
Guadalajara, Jal., Mexico.

CARDIOLOGY-PNEUMOLOGY

Jose M. Hernandez, M.D.
Department of Ecocardiography,
Doctors Hospital,
Monterrey, N.L., Mexico

PATHOLOGICAL ANATOMY

Marco A. Ponce-Camacho, M.D., Ph.D.
Department of Cytopathology, Doctors Hospital,
Monterrey, N.L., Mexico

ENDOCRINOLOGY

Jesus Zacarias Villarreal-Perez, M.D.
Department of Endocrinology,
Hospital Universitario "Dr. Jose E. Gonzalez",
Monterrey, N.L., Mexico

HEMATOLOGY

Carlos R. Best-Aguilera, M.D.
Department of Hematology,
Hospital General de Occidente. Secretaria de Salud
Zapopan, Jal., Mexico

GYNECOLOGICAL UROLOGY

Patricia I. Velazquez-Castellanos, M.D., M.Sc.
Department of Gynecology and Obstetrics,
Antiguo Hospital Civil de Guadalajara
"Fray Antonio Alcalde",
Guadalajara. Jal., Mexico

PEDIATRIC NEUROLOGY

Daniel Perez-Rulfo Ibarra, M.D., Ph.D.
Departamento de Pediatria,
Antiguo Hospital Civil de Guadalajara
"Fray Antonio Alcalde",
Guadalajara, Jal., Mexico

Follow us

https://linkedin.com/company/jmexfri

https://instagram.com/jmexfri

https://facebook.com/jmexfri

https://youtube.com/@jmexfri

https://x.com/jmexfri

Original papers should be deposited in their electronic version through the following URL:

https://publisher.jmexfri.permanyer.com

online
Manuscript
Submission

PERMANYER
www.permanyer.com

Permanyer Mexico
Temistocles, 315
Col. Polanco, Del. Miguel Hidalgo
11560 Ciudad de Mexico
mexico@permanyer.com

Permanyer
Mallorca, 310 – Barcelona (Cataluña), España
permanyer@permanyer.com

www.permanyer.com

ISSN: 2696-8444
Ref.: 11908AMEX261

Journal of the Mexican Federation
of Radiology and Imaging

EDITORIAL

Radiology and artificial intelligence: the radiologist as a leader in the era of medical informatics

Roy Riascos

Department of Diagnostic and Interventional Imaging, Division of Neuroradiology, UTHealth Houston. Houston, Texas. United States of America

Radiology has historically been at the forefront of every technological revolution that has shaped modern medicine[1]. The introduction of computed tomography (CT), followed by magnetic resonance imaging (MRI) and later functional and molecular techniques, transformed the way we study the nervous system and redefined the role of the specialist[2]. Today, we are facing an equally profound change, although less tangible at first glance in the digital revolution and the rise of artificial intelligence (AI). This transformation is not limited to adding new imaging modalities, but rather fundamentally reshapes how we conceive, process, and apply the data obtained from each study. What is changing now is the identity of the specialist who uses the technology. In modern imaging practice the radiologist is the clinical architect of information flow responsible for integrating multimodal data, guiding informatics strategy, and safeguarding the transparency, quality, and equity of new technologies.

The volume of information generated by modern imaging studies has grown exponentially[1,2]. A brain MRI exam may include diffusion sequences, perfusion maps, tractography, functional connectivity, and spectroscopy, in addition to traditional structural images. CT imaging, for its part, produces thousands of slices with increasingly fine resolution, iterative reconstructions, and multiparametric studies that reveal not only anatomy but also physiology and dynamics. This abundance of data represents an extraordinary opportunity, but also a challenge in the real time integration, prioritization, and translation of this information into clinically actionable decisions. The radiologist must embrace a role centered on transforming this ocean of data into applicable knowledge that directly impacts patients lives, shifting from passive image interpretation to active orchestration of diagnostic insight[2].

In this context, AI emerges as a powerful tool. Algorithms can segment tumors, calculate hemorrhage volumes, identify ischemic penumbras in a matter of seconds, and prioritize studies according to urgency[3]. However, it is essential to remember that these systems are statistical models trained on massive datasets and lack clinical judgment. Most commercially available algorithms have received preliminary authorizations based on data provided by their manufacturers, but they lack robust clinical studies demonstrating real world impact or improved patient outcomes[4]. This is where the radiologists responsibility becomes clear because they must supervise, validate, and contextualize the results generated by these tools to ensure their use provides true clinical value rather than a false sense of diagnostic certainty.

Before expanding the clinical use of AI, it is essential to recognize and mitigate its biases[2]. Among the most common is selection bias, which occurs when the training data do not represent the population in which the model will be deployed[2]. Another frequent issue is shortcut learning, where the algorithm relies on spurious correlations such as artifacts or scanner labels instead of true pathological features[5]. Hidden stratification may also arise, masking systematic errors within clinically important subgroups even when overall performance appears high. Demographic imbalance can further lead to uneven performance across gender,

Corresponding author:
Roy Riascos
E-mail: roy.f.riascos@ut.tmc.edu

Received for publication: 29-11-2025
Accepted for publication: 13-12-2025
DOI: 10.24875/JMEXFRI.25000035

Available online: 16-04-2026
J Mex Fed Radiol Imaging. 2026;5(1):1-3
www.JMeXFRI.com

age, or ethnic groups[6]. Finally, dataset shift describes the loss of accuracy that occurs when imaging protocols, equipment or disease prevalence differ from those in the original training population[2]. These sources of bias represent failure modes that can silently undermine clinical safety if left unaddressed. The radiologist, due to their clinical training and experience, is uniquely positioned to identify these risks and to ensure that each tool is validated locally, compared against the institutions experts, and continuously monitored in its performance.

Even when bias is carefully addressed, a second layer of challenge emerges in the real cost and complexity of implementing these tools in practice[7]. Another critical aspect is the cost of deploying the technology. Adopting AI does not simply mean purchasing a software license. The real cost includes integration with Vendor Neutral Archive (VNA) and Picture Archiving and Communication System (PACS) and Radiology Information System (RIS) systems, the required computing infrastructure, staff training, technical support, and continuous monitoring to prevent performance degradation[2,7]. In addition, the benefit should not be measured solely in diagnostic accuracy but in clear measurable clinical outcomes, such as reduced treatment times in stroke care, decreased variability in tumor interpretation, improved prediction of treatment response or fewer errors in emergency settings. Implementing a technology without a defined and measurable outcome turns AI into an expensive solution.

Alongside cost and infrastructure, a third challenge becomes evident in how these systems are organized within the clinical ecosystem[7]. In this sense, it is essential to think in terms of platforms rather than isolated applications. Purchasing tools designed for a single task may seem appealing, but it carries the risk of creating silos that fragment practice and hinder integration. The long term vision should be oriented toward interoperable platforms such as VNA, algorithm orchestration layers and clinical Machine learning operations (MLOps) environments that allow models to be swapped, new solutions to be tested in parallel, and continuity to be maintained without disrupting workflow. Through this platform based approach can AI become a sustainable clinical ally rather than an additional burden for the radiologist.

Building on these infrastructural and organizational barriers, AI must also meet several practical requirements to function safely and effectively at the point of care[4]. The first is real clinical accuracy, which depends on demonstrating that the algorithm's performance compares favorably with local radiologists and that it adapts to the specific population served at each center. The second is ease of integration, meaning the technology must fit seamlessly into PACS-RIS workflows and everyday clinical practice without creating additional burdens for the specialist. The third is ecosystem acceptance, as no tool will succeed unless it generates trust among clinicians, administrators, and patients. Achieving this requires accuracy, transparency, insight into how the model reaches conclusions and a communication strategy that clearly conveys both the capabilities and limitations of the technology.

As these technological and workflow demands intensify, the global shortage of radiologists forces us to rethink how clinical work is distributed. The solution cannot be simply to train more specialists, as the learning curve is long and demand is growing even faster. We must build teams in which the radiologist leads clinical interpretation and decision-making, while advanced technologists handle post-processing and image quality, data engineers ensure algorithm ingestion and monitoring, and quality coordinators oversee safety and regulatory compliance. This model does not diminish the radiologists role, rather, it allows them to concentrate on the tasks that still rely most heavily on human judgment such as clinical synthesis, interdisciplinary communication, and strategic leadership in technological integration.

Beyond institutional workflows, the global landscape also offers strategic opportunities, particularly for regions whose diversity can serve as a stress test for emerging technologies. Latin America represents a privileged setting for this process of validation and innovation. The genetic and epidemiological diversity of our region, together with the heterogeneity of our health systems, offers the opportunity to test algorithms in complex and challenging environments. Actively participating in multicenter projects will not only strengthen the technology but also position our institutions as international leaders in research and development of AI applied to radiology. To achieve this, it is essential for our specialists to take an active role rather than remaining passive recipients of technologies developed in other contexts.

Finally, no technological advance can be considered successful if it fails to meet fundamental ethical and equity standards. Ethics and equity must permeate this entire process. The implementation of AI in radiology must ensure data privacy and anonymization, establish mandatory medical supervision protocols to prevent automated decisions without clinical judgment, promote transparency toward patients, and verify that algorithm performance is consistent across different population subgroups. Neglecting these aspects can not only compromise patient safety but also compromise the trust that sustains the discipline as a whole.

The conclusion is clear: AI will not replace radiologists, but it will transform their practice. The specialist who understands medical informatics, leads integrated platforms, identifies biases, and critically evaluates outcomes will be the one who sets the course in the coming years. Far from being a threat, we are facing a historic opportunity to reaffirm the radiologists role as a cornerstone of integrated diagnosis in modern medicine. The key is to embrace this revolution with enthusiasm, grounded in responsibility, discernment, and genuine leadership.

Funding

The author declares that he has not received funding for this study.

Conflicts of interest

The author declares no conflicts of interest.

Ethical considerations

Protection of human subjects and animals. The author declares that no experiments on humans or animals were performed for this research.

Confidentiality, informed consent, and ethical approval. This study does not involve personal patient data, medical records, or biological samples, and does not require ethical approval. SAGER guidelines do not apply.

Declaration on the use of artificial intelligence. The authors declare that no generative artificial intelligence was used in the writing or creation of the content of this manuscript.

REFERENCES

1. Thrall JH, Li X, Li Q, Cruz C, Do S, Dreyer K, et al. Artificial Intelligence and Machine Learning in Radiology: Opportunities, Challenges, Pitfalls, and Criteria for Success. J Am Coll Radiol. 2018;15(3 Pt B):504-508. doi: 10.1016/j.jacr.2017.12.026.
2. European Society of Radiology (ESR). What the radiologist should know about artificial intelligence – an ESR white paper. Insights Imaging. 2019;10(1):44. doi: 10.1186/s13244-019-0738-2.
3. Erickson BJ, Korfiatis P, Akkus Z, Kline TL. Machine Learning for Medical Imaging. RadioGraphics. 2017;37(2):505-515. doi: 10.1148/rg.2017160130.
4. Park SH, Han K. Methodologic Guide for Evaluating Clinical Performance and Effect of Artificial Intelligence Technology for Medical Diagnosis and Prediction. Radiology. 2018;286(3):800-809. doi: 10.1148/radiol.2017171920.
5. Geirhos R, Jacobsen JH, Michaelis C, Zemel R, Brendel W, Bethge M, et al. Shortcut learning in deep neural networks. Nat Mach Intell. 2020;2(11):665-673. doi: 10.1038/s41586-020-2649-2.
6. Larrazabal AJ, Nieto N, Peterson V, Milone DH, Ferrante E. Gender imbalance in medical imaging datasets produces biased classifiers for computer-aided diagnosis. Proc Natl Acad Sci. 2020;117(23):12592-12594. doi: 10.1073/pnas.1919012117.
7. Sendak M, Gao M, Brajer N, Balu S, Nichols M, Lin A, et al. A path for translation of machine learning products into healthcare delivery. EMJ Innov [Internet]. 2020 [cited 20 Nov 2025];4(1):19-25. Available from: https://www.emjreviews.com/innovations/article/a-path-for-translation-of-machine-learning-products-into-healthcare-delivery/.

JMeXFRI

Journal of the Mexican Federation
of Radiology and Imaging

Check for updates

IN-DEPTH REVIEW

Imaging evaluation of progressive collapsing foot deformity

Alfonso E. Maldonado-Morillo[1]*, *Alex Esnaola-Braceras*[2], *Danilo E. Salazar-Chiriboga*[1], *Gonzalo Moreno-Zamarro*[1] *and Javier Fernandez-Jara*[1]

[1]Radiodiagnostic Service, Hospital Universitario Fundacion Jimenez Diaz. Madrid; [2]Radiodiagnostic Service, Hospital Universitario de Galdakao, Bilbao. Spain

ABSTRACT

Progressive collapsing foot deformity (PCFD), previously known as adult-acquired flatfoot deformity, is a complex multifactorial condition characterized by medial arch collapse, hindfoot valgus, and forefoot abduction. Imaging plays a central role in diagnosis, staging, and treatment planning by providing objective assessment of structural and functional abnormalities. Weight-bearing radiography remains the first-line modality for evaluating global alignment and key angular parameters. However, complementary techniques such as ultrasound, computed tomography (CT), weight-bearing CT (WBCT), and magnetic resonance imaging (MRI) are essential for assessing soft tissue integrity, three-dimensional bone relationships, and early pathological changes. Recent advances, including WBCT and artificial intelligence-based tools, have improved diagnostic accuracy and reproducibility. This review provides a comprehensive and practical overview of imaging findings in PCFD, emphasizing the role of each modality, key radiological measurements, and their clinical relevance. The integration of multimodality imaging is essential for accurate diagnosis, classification, and therapeutic decision-making.

Keywords: *Progressive collapsing foot deformity. Flatfoot deformity. Saltzman view. Posterior tibial tendon. Spring ligament.*

INTRODUCTION

Progressive collapsing foot deformity (PCFD), formerly known as adult-acquired flatfoot deformity, is a complex and dynamic condition characterized by progressive failure of the medial longitudinal arch, hindfoot valgus, and forefoot abduction. This condition includes a broad spectrum of structural and functional abnormalities involving osseous alignment, ligamentous integrity, and tendon dysfunction – most notably of the posterior tibial tendon[1,2].

Imaging plays a central role in the diagnosis, staging, and management of PCFD by allowing objective characterization of deformity components and providing essential information for treatment planning. Weight-bearing radiography remains the cornerstone of initial assessment, enabling evaluation of global alignment and standardized angular measurements. However, due to the multifactorial nature of the deformity, complementary imaging modalities – including ultrasound, computed tomography (CT), weight-bearing CT (WBCT), and magnetic resonance imaging (MRI) – are often required to assess soft tissue integrity, three-dimensional bone relationships, and early or subtle pathological changes[1,3-5].

Despite advances in imaging techniques, variability persists in clinical practice regarding the optimal use and interpretation of each modality, particularly across

***Corresponding author:**
Alfonso E. Maldonado-Morillo
E-mail: alfmald21@gmail.com

Received for publication: 05-12-2025
Accepted for publication: 15-01-2026
DOI: 10.24875/JMEXFRI.M26000126

Available online: 16-04-2026
J Mex Fed Radiol Imaging. 2026;5(1):4-14
www.JMeXFRI.com

Table 1. New consensus group classification for PCFD[9]

Component	Description
A	Hindfoot valgus
B	Midfoot or forefoot abductus
C	Forefoot supination, varus, or medial column instability
D	Peritalar subluxation or dislocation
E	Ankle instability

PCFD: progressive collapsing foot deformity.

different stages of the disease. Additionally, the integration of emerging technologies, such as WBCT and artificial intelligence-based measurement tools, is reshaping the diagnostic approach and improving reproducibility. The purpose of this review is to provide a comprehensive and practical overview of imaging findings in PCFD, highlighting the role of each modality, key radiological parameters, and their clinical implications. Emphasis is placed on correlating imaging features with deformity components and current classification systems, to facilitate accurate diagnosis and guide therapeutic decision-making[1,3-5].

RADIOGRAPHIC EXAMINATION

Standard radiographic projections – including anteroposterior (AP), lateral, AP ankle, and axial hindfoot views – allow systematic assessment of forefoot abduction, medial arch collapse, and hindfoot valgus alignment. Since the mid-20th century, several authors have described and standardized angular parameters of the foot using plain radiography to quantify medial arch collapse and hindfoot deformity. Classic works by Gentili et al. (1996) and Lamm et al. (2016) established the foundations for geometric evaluation using principal axes[6,7]. Currently, this classical geometric framework has evolved into artificial intelligence-based tools, such as automated bone measurement platforms, which standardize angular measurements and improve precision and reproducibility.

Anteroposterior radiograph

The weight-bearing AP foot projection allows assessment of midfoot and forefoot alignment and is essential for detecting forefoot abduction and hindfoot valgus within the classification framework of PCFD. This projection is particularly useful for identifying the type B component[8,9] (Table 1).

Talo-first metatarsal angle (Meary angle) (Figure 1): this angle evaluates alignment between the hindfoot and forefoot and is a key indicator of forefoot abduction in acquired flatfoot deformity. It is formed by the intersection of the longitudinal axis of the talus and that of the first metatarsal. On the AP projection, progressive deformity is reflected by increasing lateral deviation of the first metatarsal axis relative to the talar axis[5,10]. Under normal conditions, both axes are parallel or show minimal lateral divergence. Axis divergence may be graded as mild (> 4°), moderate (> 15°), or severe (> 30°)[11].

Talonavicular coverage angle (TCA) (Figure 1): the talonavicular coverage angle is one of the most widely used parameters on weight-bearing AP radiographs for evaluating forefoot abduction and talonavicular joint incongruity. It is defined as the angle formed by lines connecting the medial and lateral articular margins of the talar head and the navicular[5,10-12]. In normal alignment, both articular surfaces are nearly parallel (approximately 0°). Increasing values indicate progressive loss of congruency and lateral displacement of the forefoot. The cutoff points for the TCA vary among authors: several series consider values greater than 7° to be pathological[5,10,11], while other place normal values below 15-20°[12]. Based on this variability, values greater than 7-20° represent a significant alteration of medial alignment. Higher TCA values have been associated with posterior tibial tendon rupture (starting at 26°) and with sinus tarsi impingement, for which a cutoff value of 41.2° has been described, with a positive predictive value of 100%[13].

Talocalcaneal angle (Kite angle) (Figure 1): the talocalcaneal angle is a classic measurement obtained on weight-bearing AP radiographs and reflects the coronal relationship between the talar and calcaneal axes. It is formed by a line drawn along the longitudinal axis of the talar neck and head and another line parallel to the lateral border of the calcaneus or along the longitudinal axis of the hindfoot, depending on the technical description used[6,7,10]. Normal values are generally reported between approximately 17° and 40°[6,7,10]. Angles greater than 35-40° are typically associated with hindfoot valgus, whereas values below approximately 25° suggest hindfoot varus alignment[10,14].

Lateral radiograph

The weight-bearing lateral radiographic projection enables objective quantification of the sagittal behavior of the medial longitudinal arch and the talo-first

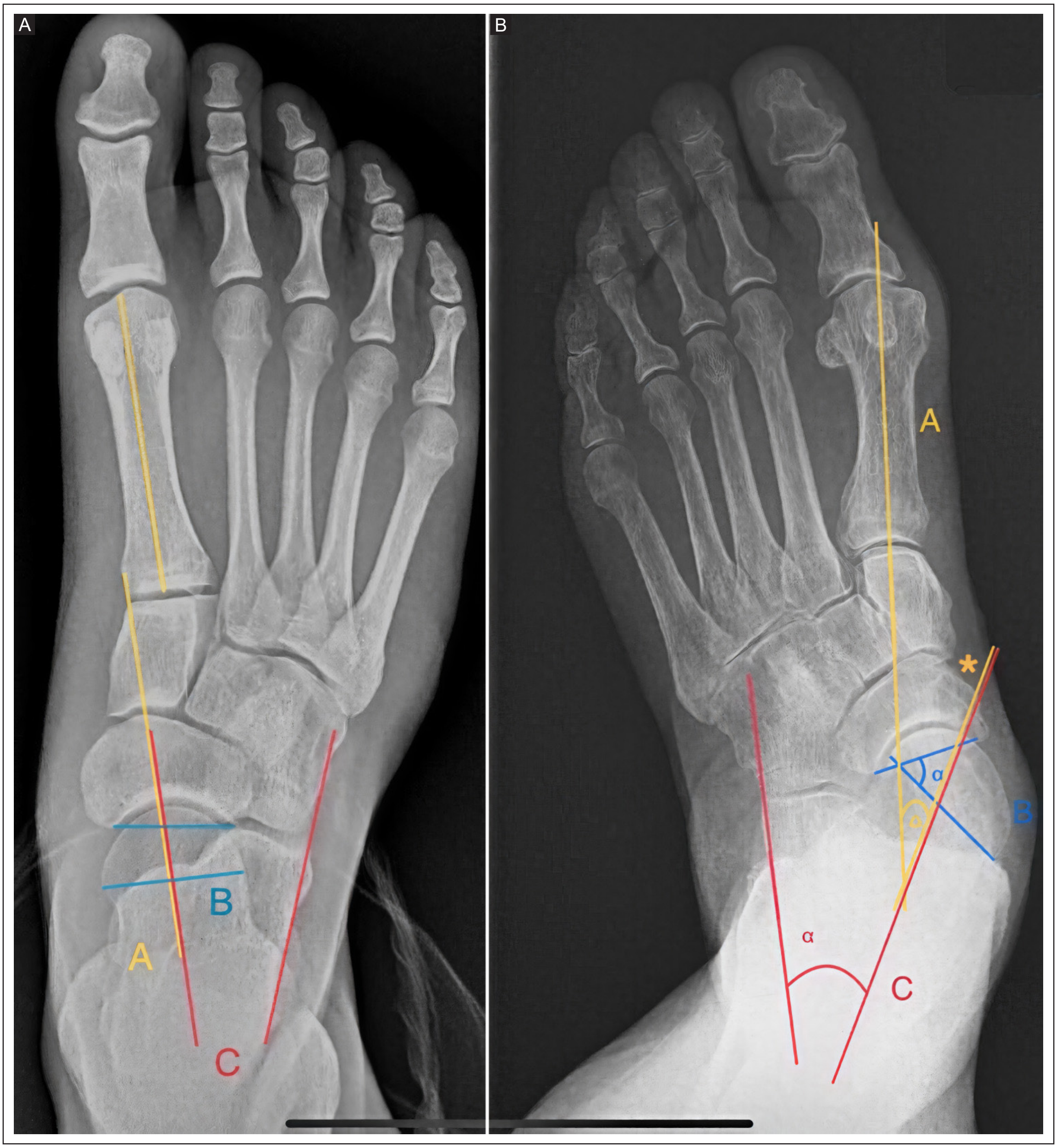

Figure 1. A: normal AP foot radiograph showing the talo-first metatarsal angle (yellow A), talonavicular coverage angle (blue B), and talocalcaneal angle (red C). **B:** same angles and color coding on an AP radiograph with deformity. The orange asterisk indicates insertional enthesopathy of the PTT as an indirect radiographic sign.

AP: anteroposterior; PTT: posterior tibial tendon.

metatarsal relationship using well-established parameters[10,15]. This projection is especially useful for evaluating type C deformity within the PCFD classification, which corresponds to forefoot supination or medial column instability, typically indicated by disruption of the Meary angle[8]. Additionally, it may provide information regarding type D deformity, as significant overlap between the talar and calcaneal silhouettes (talocalcaneal overlap, TCO) may suggest subtalar subluxation with hindfoot valgus and, in advanced stages, subfibular impingement due to calcaneofibular contact, reflecting painful subtalar instability[9].

Meary angle (Figure 2): also known as the talo-first metatarsal (T1MT) angle, this is one of the most widely

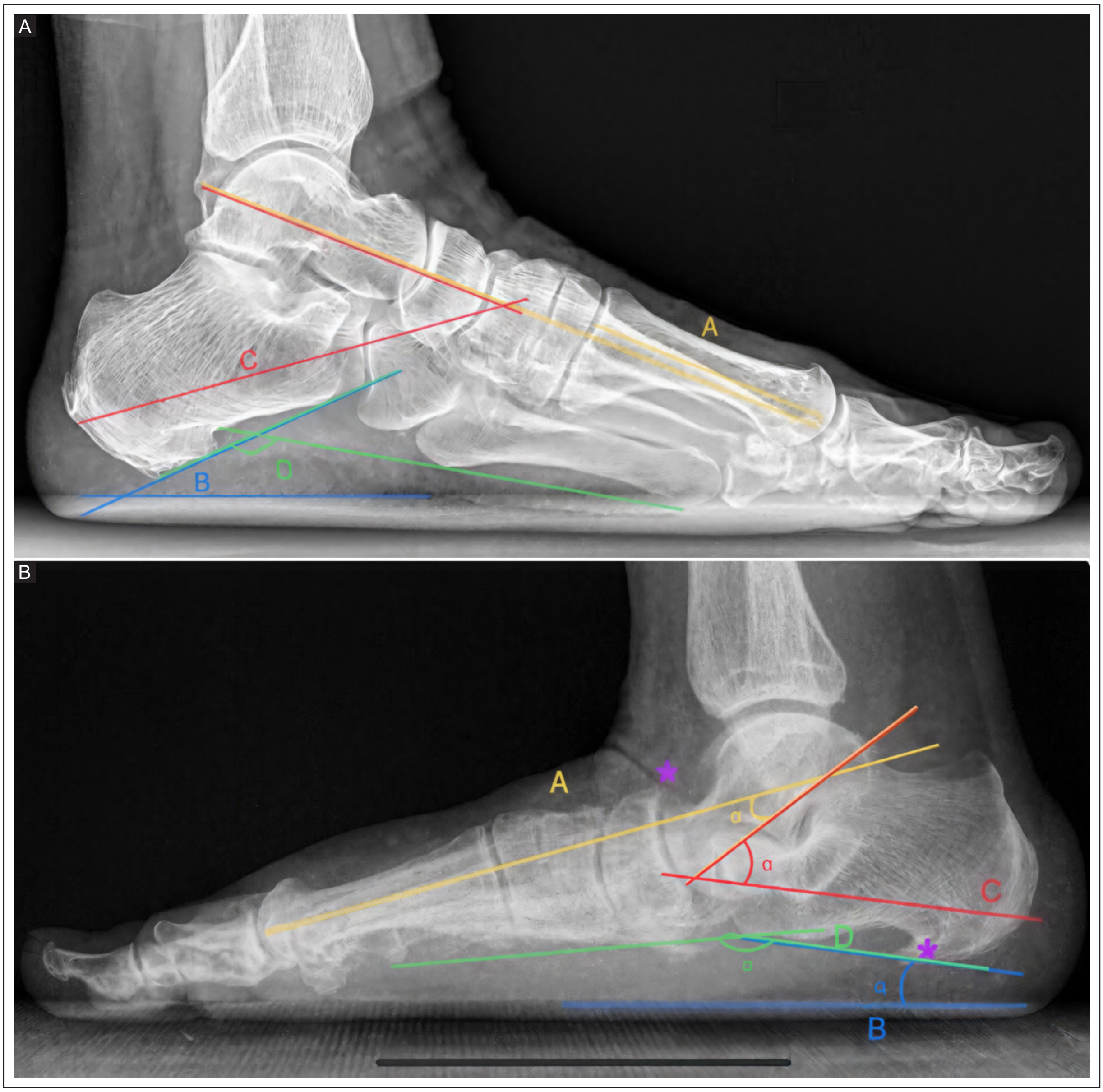

Figure 2. A: normal lateral foot radiograph showing the Meary angle (yellow A), calcaneal pitch angle (blue B), talocalcaneal angle (red C), and calcaneus-fifth metatarsal angle (green D). **B:** same angles and color coding on a lateral radiograph with deformity. Purple asterisks indicate a talar beak and calcaneal spur as an indirect radiographic signs.

used and reproducible parameters on weight-bearing lateral radiographs for assessing medial longitudinal arch collapse. It is defined by the intersection of the longitudinal axis of the talar body and neck with that of the first metatarsal[10]. Although slight variations in reported values exist[7,12,16], widely accepted criteria define 0° as normal, > 4° as mild deformity, > 15° as moderate, and > 30° as severe[5,10,11]. The Meary angle has also been associated with posterior tibial tendon dysfunction[17], demonstrates high reliability for evaluating arch height[16], and shows excellent diagnostic reproducibility[14].

Calcaneal pitch angle (Figure 2): the calcaneal pitch is another commonly used parameter, defined as the angle between a horizontal line (parallel to the ground) and the inferior surface of the calcaneus, reflecting hindfoot orientation relative to the supporting surface[6,10]. Normal values are typically between 20° and 30°, while values below approximately 18-20° indicate medial arch collapse or flatfoot deformity[5,10,11]. Decreased calcaneal pitch has been associated with posterior tibial tendon tears and is considered one of the most representative radiographic indicators of medial arch support failure[17]. It also demonstrates high reproducibility and reliability[14].

Calcaneus-fifth metatarsal angle (C5MA) (Figure 2): this angle evaluates the relationship between the calcaneus and the fifth metatarsal, both components of the lateral column. It is defined by the intersection between the plantar surface of the calcaneus and the inferior border of the fifth metatarsal. Normal values range from 150° to 165°, while values greater than 170° suggest lateral column insufficiency or collapse[10,11].

Medial cuneiform-fifth metatarsal distance (MC-5MT): although not a direct measure of the medial arch, this parameter provides complementary information. It represents the distance between the inferior border of the medial cuneiform and the base of the fifth metatarsal[12]. Normal values are approximately 17-18 mm, whereas values below approximately 6 mm are associated with deformity or lateral column collapse[12,13,16].

Talocalcaneal angle (Figure 2)**:** on the lateral projection, the talocalcaneal (Kite) angle is formed between the longitudinal axis of the hindfoot and the midline of the talus. It is typically increased in pronated feet, with values below 45° considered normal and values above 45° considered abnormal[11].

Costa-Bartani angle**:** defined by two lines: one from the calcaneal tuberosity to the inferior aspect of the talonavicular joint, and another from this point to the inferior border of the first metatarsal head. Normal values range from 120° to 130°, with values above 130° considered pathological[18].

Saltzman view

Axial hindfoot projections are essential for radiographic evaluation. In the current classification of PCFD, these views assess type A deformity, corresponding to hindfoot valgus (Table 1)[9]. Among these, the hindfoot alignment view (HAV), described by Saltzman and el-Khoury (1995), was a major advancement by standardizing coronal evaluation of the tibio-calcaneal axis under weight-bearing conditions, enabling reproducible quantification of calcaneal displacement relative to the tibial axis[19].

This projection allows measurement of the hindfoot moment arm (HMA), defined as the shortest distance between the longitudinal axis of the tibia – determined by bisecting the tibial diaphysis at 10 and 15 cm above the ankle – and the most inferior point of the calcaneus[11,19]. Normal values generally range from –3 mm to +10 mm, while values greater than 10 mm indicate hindfoot valgus deformity[11,12]. In advanced deformities, markedly increased HMA values have been associated with calcaneofibular impingement, highlighting the clinical utility of this parameter in detecting lateral overload[13]. Several modifications of the original method have been proposed. One of the most relevant is the hindfoot alignment angle (HAA)[20], which complements the HMA by quantifying the angular relationship between the tibial and calcaneal axes. This parameter shows a strong correlation with HMA and effectively differentiates alignment abnormalities[20]. It is defined as the angle between the longitudinal axis of the tibia and the axis of the calcaneal tuberosity[11]. In normal subjects, mean values are 5.6° ± 0.4°, and values near 22.5° ± 4.9° are seen in cases of deformity[11,20].

Anteroposterior ankle radiograph

The weight-bearing AP ankle projection assesses tibiotalar alignment and detects instability or secondary degenerative changes. It is particularly relevant in the type E component of the PCFD classification, where progressive valgus deformity compromises the deltoid ligament, resulting in valgus tilting of the talus on weight-bearing radiographs[9] (Table 1).

Talar tilt (TT) (Figure 3): defined as the angle between the tibial plafond and the talar dome on the AP ankle projection. It has a narrow normal range, typically between –1.5° and +1.5°[15]. Values greater than 5° are considered pathological and indicate tibiotalar valgus alignment, often associated with deltoid ligament insufficiency[17].

Tibiotalar surface angle (Figure 3): the tibiotalar surface angle evaluates talar alignment in the coronal plane. It is measured between the longitudinal axis of the tibia – defined by a line passing through points located 8 and 13 cm proximal to the distal articular surface – and the articular surface of the talar dome on weight-bearing radiographs[21]. Normal values are typically close to 87-89°, while values exceeding approximately 94° indicate pathological valgus alignment and may reflect significant failure of the deltoid ligament complex[21].

Other radiographic findings

In addition to allowing measurement of alignment angles, plain radiography provides valuable information on other osseous and articular findings that may indicate chronicity or underlying causes of the deformity.

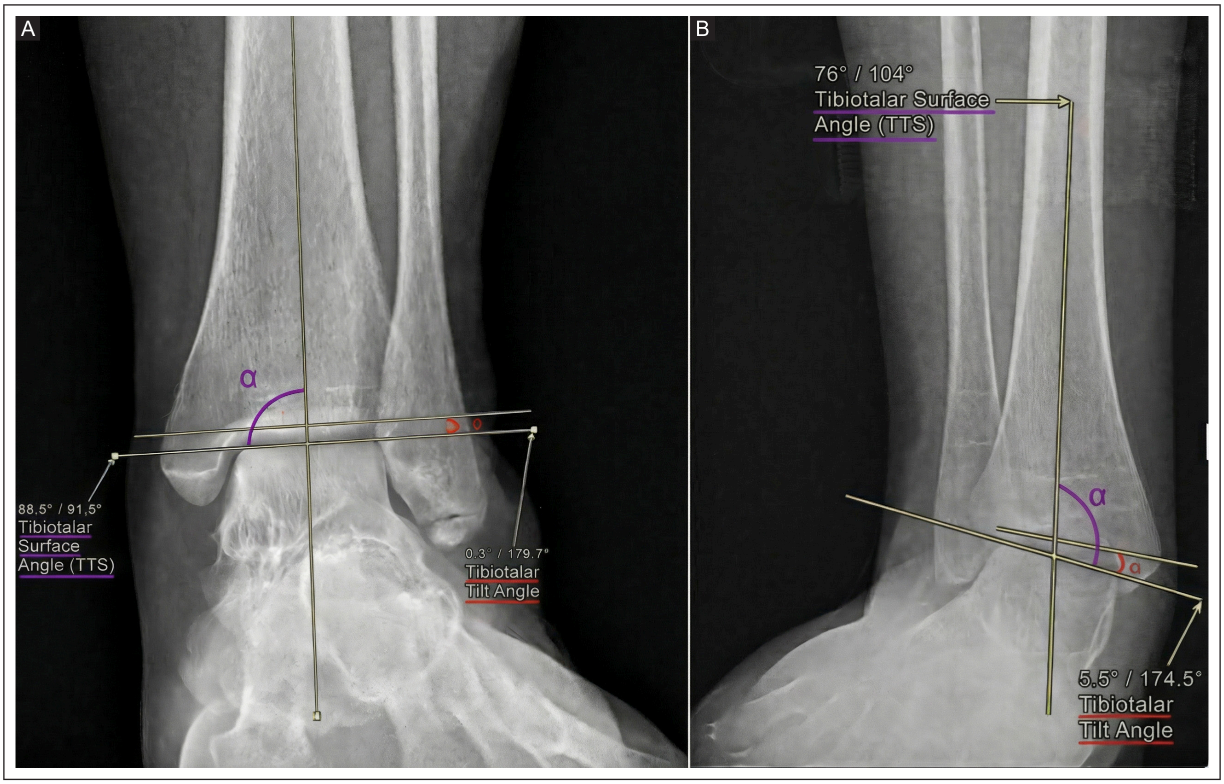

Figure 3. A: weight-bearing AP ankle radiograph with normal values. The tibiotalar surface angle is shown in purple, and the talar tilt (tibiotalar tilt angle) is shown in red. **B:** same angles and color coding on an AP radiograph with deformity.

AP: anteroposterior.

The most relevant include:

Calcaneal spur (Figure 2): an exophytic bony growth at the calcaneal tuberosity, typically located at the insertion of the plantar fascia.

Talar beak (Figure 2): an exophytic bony prominence or osteophyte at the dorsal aspect of the talar head, corresponding to the capsular insertion of the talonavicular joint.

Navicular enthesopathy (Figure 1): cortical irregularity or hypertrophic changes at the navicular tuberosity, which may reflect chronic traction of the posterior tibial tendon or associated tendinopathy[10,22].

Tibial spurs: these may appear as a secondary sign of posterior tibial tendon dysfunction and are best visualized on lateral projections, as they are often located in the retromalleolar region[22].

Accessory navicular: present in a minority of adults, this comprises three anatomical types. Types II and III are more frequently associated with pain and flatfoot valgus deformity, as they alter the insertion angle of the posterior tibial tendon and increase stress across the synchondrosis. Type II is the most common symptomatic variant[10,15].

Coalitions and other congenital anomalies: weight-bearing radiographs may show indirect signs of tarsal coalition, including characteristic osseous contours and bridging patterns suggestive of abnormal joint connections (C-sign, anteater sign)[23].

ULTRASOUND

Ultrasound is a valuable tool for evaluating the integrity of the posterior tibial tendon (PTT) and other soft tissue structures. Its superficial course allows optimal assessment with high-frequency linear transducers. Ultrasound is relatively low-cost and often more accessible than MRI; however, it requires an experienced musculoskeletal sonographer.

Ultrasound provides detailed visualization of tendon fibers, allows Doppler (color or power) assessment, and enables dynamic evaluation. It also permits the use of provocative maneuvers to reproduce pain, as well as assessment of friction phenomena or anterior subluxation in cases of flexor retinaculum injury[10,11,22]. Some authors propose ultrasound as the initial imaging modality, as it may be slightly more accurate than 3T MRI in diagnosing PTT dysfunction. MRI can be reserved for inconclusive cases or for detecting bone marrow edema and other secondary findings[24].

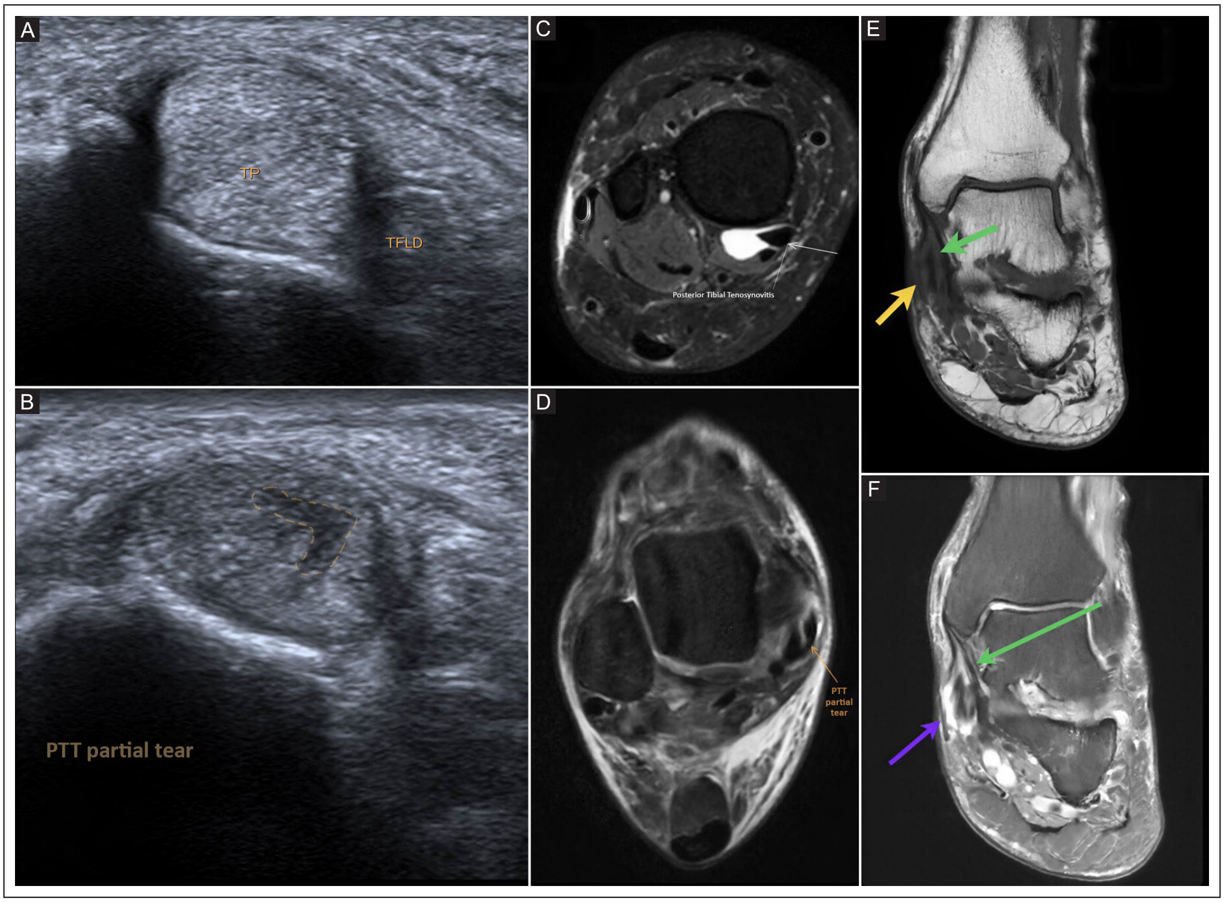

Figure 4. A: thickening of the posterior tibial tendon consistent with tendinosis. **B:** linear hypoechoic defect within the PTT, consistent with a partial tear. **C:** axial fluid-sensitive MRI sequence demonstrating tenosynovitis. **D:** axial fluid-sensitive MRI sequence showing a linear intratendinous defect consistent with a partial tear. **E-F:** coronal MRI T1-weighted and fluid-sensitive sequences, respectively. Yellow and purple arrows indicate disruption of the fibrillar pattern of the posterior tibial tendon, consistent with a partial tear. On the fluid-sensitive MRI sequence, associated tenosynovitis is also observed. The green arrow highlights the deltoid ligament, which appears thickened, consistent with a sprain.

MRI: magnetic resonance imaging; PTT: posterior tibial tendon.

Posterior tibial tendon and flexor retinaculum: the superficial course of the posterior tibial tendon allows optimal ultrasound evaluation with high-resolution linear transducers[22].

Normal tendon: the tendon appears with a homogeneous, hyperechoic fibrillar pattern, well defined and with uniform echogenicity. Comparison with the asymptomatic contralateral side may help detect subtle changes in tendon thickness or echotexture in early stages[22].

Tenosynovitis: characterized by anechoic or hypoechoic fluid surrounding the tendon and thickening of the tendon sheath, typically greater than 7 mm. On transverse imaging, this produces a central hyperechoic structure surrounded by an anechoic or hypoechoic halo[10].

Tendinosis (Figure 4): demonstrates tendon thickening with heterogeneous echotexture and possible loss of the normal fibrillar pattern[15].

Tears (Figure 4): these may be partial, appearing as hypoechoic clefts within the fibrillar pattern, or complete, with total loss of tendon continuity[24].

Spring ligament (plantar calcaneonavicular ligament): ultrasound can assist in evaluating the spring ligament by positioning the probe inferior to the medial malleolus, with one end over the sustentaculum tali and the other slightly angled toward the talar head[25]. Ultrasound reliably identifies tears of the superomedial bundle, the most relevant component of the ligament complex. These may present as thickening greater than 4 mm with hypoechoic areas, or as thinning below 2 mm[24]. Additionally, absence of visualization of the structure deep to the posterior tibial tendon along its course over the talar head may suggest ligament rupture (Figure 3)[22].

Other supporting structures of the medial arch: the plantar fascia, due to its superficial location, is readily assessed with ultrasound and may show thickening and irregularity in degenerative conditions. In contrast, the sinus tarsi, due to its depth and orientation, and the deltoid ligament complex, due to its anatomical complexity and typically late involvement, have limited evaluation with ultrasound and are more accurately assessed with MRI[10].

COMPUTED TOMOGRAPHY

Conventional CT

Conventional CT is the most useful imaging modality for evaluating osseous abnormalities in flatfoot deformity. It is especially valuable in cases of tarsal coalition, as it allows precise localization of the coalition by assessing the joint in multiple planes. Additionally, conventional CT facilitates the detection of advanced degenerative changes and is useful for preoperative planning[15]. However, its main limitation is that images are acquired under non-weight-bearing conditions, which prevents assessment of the effect of gravity on foot alignment and may underestimate certain deformities[8,11].

Weight-bearing CT

The introduction of WBCT represents a significant advancement, as it enables three-dimensional evaluation of the foot skeleton in a physiological position under the influence of gravity and muscular forces. This provides a more comprehensive assessment of bone displacement and rotational alignment under load, allowing a more detailed analysis of characteristic findings in PCFD[8]. International consensus supports the use of WBCT when available, particularly for surgical planning[3,5].

The main abnormalities to assess include sinus tarsi impingement, increased valgus inclination of the posterior facet of the subtalar joint, subtalar subluxation involving the posterior and/or middle facets, and subfibular impingement[3]. WBCT has been shown to modify the classification of PCFD by increasing the detection of types B, C, and D – associated with forefoot abduction, medial arch collapse, and peritalar subluxation – compared with conventional radiography[26] (Table 1). In contrast, types A and E are better characterized using standard radiographs. Furthermore, significant subtalar subluxation and sinus tarsi impingement have been observed exclusively in symptomatic feet, suggesting that these parameters may serve as key imaging biomarkers to differentiate pathological flatfoot deformities from asymptomatic variants[27].

MAGNETIC RESONANCE IMAGING

MRI is considered the most comprehensive modality for evaluating flatfoot deformity, as it provides excellent assessment of supporting soft tissue structures and adequate evaluation of osseous anatomy, including detection of tarsal coalitions[15]. Recommended sequences include T1-weighted images for anatomical assessment and fluid-sensitive sequences (T2- or proton density-weighted with fat suppression, or short tau inversion recovery STIR) to evaluate edema and inflammatory changes in soft tissues[11,15]. Commonly used protocols include sagittal T1-weighted images, sagittal STIR sequences, axial proton density and T2-weighted images with fat suppression, as well as coronal planes tailored to ankle evaluation[11].

Posterior tibial tendon: under normal conditions, the posterior tibial tendon (PTT) is the most medial and largest of the three flexor tendons, with an ovoid morphology and a diameter approximately twice that of the flexor digitorum longus[10,15,22]. It demonstrates homogeneous low signal intensity on all sequences[15], with a typical transverse diameter ranging from 7 to 11 mm[10]. Recognized pitfalls include physiological thickening of the tendon (< 2 mm) at its distal insertion and the presence of a small amount of noncircumferential fluid within the tendon sheath, both considered normal findings[15,28]. Pathologic changes are best evaluated on fluid-sensitive sequences. MRI demonstrates high sensitivity (95%) and specificity (100%) for detecting PTT pathology, with excellent overall diagnostic accuracy (96%)[15,28].

Tenosynovitis (Figure 4): characterized by fluid or synovial proliferation distending the tendon sheath, surrounding the tendon circumferentially (thickness > 2 mm or involving more than 50% of its circumference), often with adjacent soft tissue edema, while the tendon maintains its morphology and low signal intensity[10,11,15,27]. As the tendon sheath typically ends 1-2 cm proximal to the navicular, fluid surrounding the tendon distal to this point should be described as paratenonitis[10,15,28].

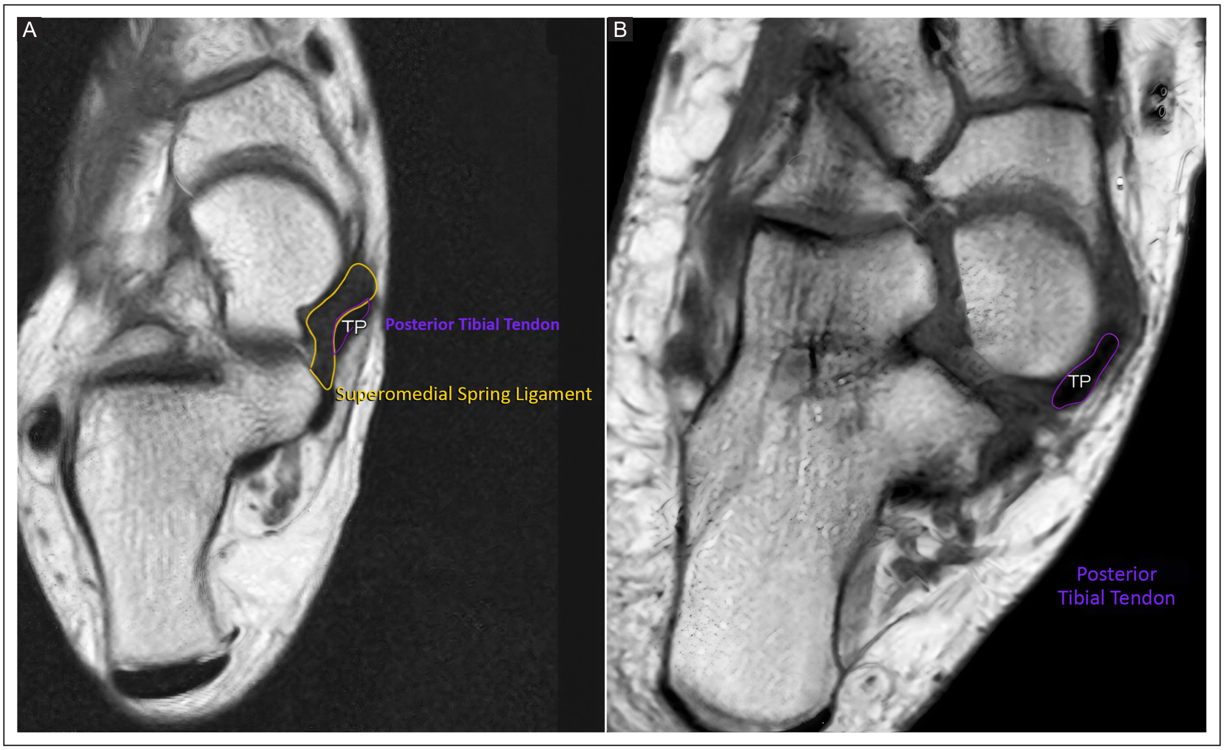

Figure 5. A: axial MRI T1-weighted image. The superomedial bundle of the spring ligament is highlighted in yellow, and the posterior tibial tendon in purple. The close anatomical relationship between these structures is demonstrated, as described in the text. **B:** axial MRI proton density-weighted image. Findings are consistent with complete rupture of the superomedial bundle of the spring ligament. As a result, the PTT is in direct contact with the talar head, without the normal intervening structure. This image illustrates the same findings observed on ultrasound, where the PTT lies in direct contact with the talar head due to ligament disruption.

MRI: magnetic resonance imaging; PTT: posterior tibial tendon.

Tendinosis: findings include tendon thickening, surface irregularity, and heterogeneous intratendinous signal of lower intensity than fluid. Increased signal intensity may also be observed with preservation of tendon morphology[10,11].

Tears: *Type I (mild partial tear)* (Figure 4): hypertrophic tendon (greater than twice the size of the flexor digitorum longus) with increased intrasubstance signal and longitudinal splits within a thickened tendon; these findings may be difficult to differentiate from advanced tendinosis. *Type II (moderate partial tear)*: atrophic tendon, reflecting fiber loss and attritional changes. *Type III (complete tear):* absence of the tendon or a fluid-filled gap, with possible visualization of an empty tendon sheath at the site of discontinuity[10,15,22].

The PTT undergoes an abrupt change in direction – approximately 90° around the medial malleolus – which may produce signal alterations on MRI and lead to false-positive or false-negative interpretations of partial or complete tears[23]. This corresponds to the magic angle artifact, which occurs as the tendon curves beneath the medial malleolus and may mimic tendinosis without representing true structural abnormality[10].

Spring ligament (plantar calcaneonavicular ligament): abnormalities of the spring ligament, particularly involving the superomedial bundle, may occur in isolation or, more commonly, in association with PTT dysfunction and medial arch collapse[11,15,25]. Imaging findings suggestive of injury include ligament thickening > 5-6 mm or thinning < 2 mm[10,11,25,28], along with increased signal intensity on fluid-sensitive sequences, heterogeneity, waviness, or fiber discontinuity. These changes may be associated with periligamentous edema or complete disruption of ligament fibers[10,22] (Figure 5).

OTHER FINDINGS IN DIFFERENT STRUCTURES

Sinus tarsi syndrome (Figure 6): characterized by alteration or loss of the normal fat signal within the

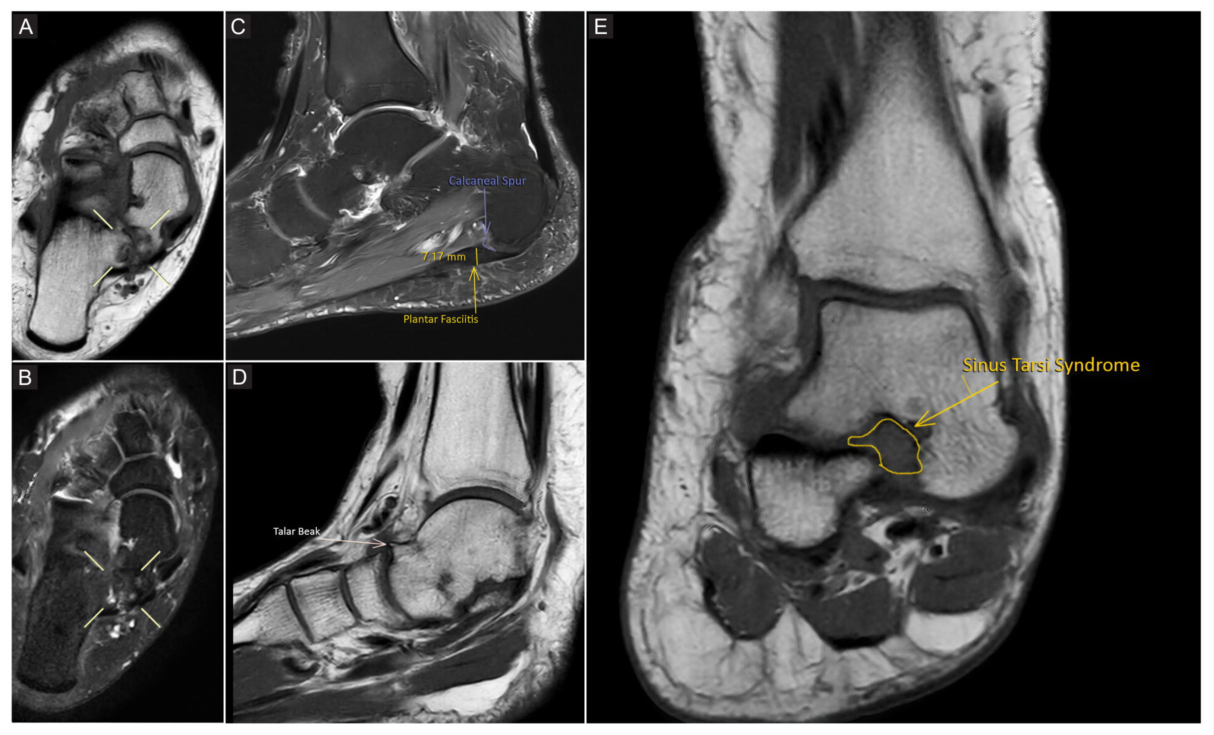

Figure 6. A-B: axial MRI T1-weighted and fluid-sensitive sequences, respectively. Findings are consistent with a non-osseous tarsal coalition. **C:** sagittal MRI fluid-sensitive sequence demonstrating thickening of the plantar fascia and the presence of a calcaneal spur as indirect signs of pathology. **D:** sagittal MRI T1- weighted sequence showing a talar beak at the dorsal aspect of the talonavicular joint as another indirect sign. **E:** coronal MRI T1-weighted sequence demonstrating loss of normal fat signal within the sinus tarsi, consistent with sinus tarsi syndrome.

MRI: magnetic resonance imaging.

sinus tarsi, replaced by edematous, inflammatory, or fibrotic tissue. This results in low signal intensity on T1-weighted images and high or variable signal on fluid-sensitive sequences, depending on the stage[10,28]. The edematous appearance may obscure the sinus tarsi ligaments[22].

Deltoid ligament complex: the deltoid ligament consists of multiple components that stabilize the ankle against valgus displacement of the talus[15], and MRI is the modality of choice for its evaluation[10,15]. Under normal conditions, the ligament appears as low- to intermediate-signal bands that widen distally, best visualized on axial and coronal planes. Degenerative changes or partial tears show loss of normal fat striations, signal heterogeneity, and architectural distortion, while high-grade tears demonstrate fiber discontinuity or fluid-filled gaps[10].

Plantar fascia (Figure 6): MRI shows thickening (> 4 mm), irregularity, and heterogeneous signal at the calcaneal insertion of the fascia, often associated with perifascial and bone marrow edema[10]. Degenerative tears usually involve the central band near the calcaneus – often following corticosteroid injections – while traumatic tears tend to occur more distally[10].

Bone marrow edema and impingement: in talocalcaneal impingement, bone marrow edema, cystic changes, or sclerosis may be seen at the opposing surfaces of the lateral process of the talus and the lateral wall of the calcaneus. Subfibular impingement may present as low-signal soft tissue interposition on both T1- and T2-weighted images or as direct osseous contact, with or without associated bone marrow edema[28]. Reactive edema may also be identified in the distal tibial retromalleolar groove or at the navicular insertion of the PTT[22].

CONCLUSION

Imaging evaluation of PCFD integrates complementary modalities that allow objective assessment of medial arch collapse, forefoot abduction, and hindfoot valgus, correlating imaging findings with the different components of the current classification. Weight-bearing radiography remains the initial cornerstone for assessing overall alignment, while ultrasound provides precise and dynamic evaluation of tendinous and ligamentous structures. WBCT offers three-dimensional characterization of the skeletal anatomy and improves detection of peritalar subluxation. MRI remains the most comprehensive modality, integrating soft tissue abnormalities with associated osseous changes, and plays a key role in diagnosis and therapeutic planning.

Acknowledgment

The authors thank Professor Ana M. Contreras-Navarro for her guidance in preparing this scientific paper.

Funding

The authors declare that they have not received funding.

Conflicts of interest

The authors declare no conflicts of interest.

Ethical considerations

Protection of human subjects and animals. The authors declare that no experiments on humans or animals were performed for this research.

Confidentiality, informed consent, and ethical approval. The authors have obtained approval from the Ethics Committee for the analysis of routinely collected and anonymized clinical data; therefore, individual informed consent was not required. Relevant ethical recommendations have been followed.

Declaration on the use of artificial intelligence. The authors declare that no generative artificial intelligence was used in the writing or creation of the content of this manuscript.

REFERENCES

1. Myerson MS, Thordarson DB, Johnson JE, Hintermann B, Sangeorzan BJ, Deland JT, et al. Classification and nomenclature: progressive collapsing foot deformity. Foot Ankle Int. 2020;41(10):1271-1276. doi: 10.1177/1071100720950722.
2. Deland JT. Adult-acquired flatfoot deformity. J Am Acad Orthop Surg. 2008;16(7):399-406. doi: 10.5435/00124635-200807000-00005.
3. de Cesar-Netto C, Myerson MS, Day J, Ellis SJ, Hintermann B, Johnson JE, et al. Consensus for the use of weightbearing CT in the assessment of progressive collapsing foot deformity. Foot Ankle Int. 2020;41(10):1277-1282. doi: 10.1177/1071100720950734.
4. Barg A, Bailey T, Richter M, de Cesar Netto C, Lintz F, Burssens A, et al. Weightbearing computed tomography of the foot and ankle: emerging technology topical review. Foot Ankle Int. 2018;39(3):376-386. doi: 10.1177/1071100717740330.
5. Lôbo CFT, Pires EA, Bordalo-Rodrigues M, de Cesar-Netto C, Godoy-Santos AL. Imaging of progressive collapsing foot deformity with emphasis on the role of weightbearing cone beam CT. Skeletal Radiol. 2022;51(6):1127-1141. doi: 10.1007/s00256-021-03942-1.
6. Gentili A, Masih S, Yao L, Seeger LL. Pictorial review: foot axes and angles. Br J Radiol. 1996;69(826):968-974. doi: 10.1259/0007-1285-69-826-968.
7. Lamm BM, Stasko PA, Gesheff MG, Bhave A. Normal foot and ankle radiographic angles, measurements, and reference points. J Foot Ankle Surg. 2016;55(5):991-998. doi: 10.1053/j.jfas.2016.05.005.
8. Lalevée M, Dagneaux L, Lintz F, de Cesar-Netto C. Flatfoot: new diagnostic modalities. Orthop Traumatol Surg Res. 2026;112(1S):104415. doi: 10.1016/j.otsr.2025.104415.
9. Hong VY, Lee DC, Smith RW, Harris TG. So What exactly is progressive collapsing foot deformity? J Am Acad Orthop Surg. 2025;33(16):e940-e948. doi: 10.5435/JAAOS-D-24-01499.
10. Flores DV, Mejía-Gómez C, Fernández-Hernando M, Davis MA, Pathria MN. Adult acquired flatfoot deformity: anatomy, biomechanics, staging, and imaging findings. Radiographics. 2019;39(5):1437-1460. doi: 10.1148/rg.2019190046.
11. Polichetti C, Borruto MI, Lauriero F, Caravelli S, Mosca M, Maccauro G, et al. Adult acquired flatfoot deformity: a narrative review about imaging findings. Diagnostics (Basel). 2023;13(2):225. doi: 10.3390/diagnostics13020225.
12. Henry JK, Shakked R, Ellis SJ. Adult-acquired flatfoot deformity. Foot Ankle Orthop. 2019;4(1):2473011418820847. doi: 10.1177/2473011418820847.
13. Kim J, Rajan L, Fuller R, Sofka C, Cororaton A, Demetracopoulos C, et al. Radiographic cutoff values for predicting lateral bony impingement in progressive collapsing foot deformity. Foot Ankle Int. 2022;43(9):1219-1226. doi: 10.1177/10711007221099010.
14. Yildiz K, Cetin T. Interobserver reliability in the radiological evaluation of flatfoot (Pes Planus) deformity: a cross-sectional study. J Foot Ankle Surg. 2022;61(5):1065-1070. doi: 10.1053/j.jfas.2022.01.021.
15. Lin YC, Kwon JY, Ghorbanhoseini M, Wu JS. The hindfoot arch: what role does the imager play? Radiol Clin North Am. 2016;54(5):951-968. doi: 10.1016/j.rcl.2016.04.012.
16. Younger AS, Sawatzky B, Dryden P. Radiographic assessment of adult flatfoot. Foot Ankle Int. 2005;26(10):820-825. doi: 10.1177/107110070502601006.
17. Lin YC, Mhuircheartaigh JN, Lamb J, Kung JW, Yablon CM, Wu JS. Imaging of adult flatfoot: correlation of radiographic measurements with MRI. AJR Am J Roentgenol. 2015;204(2):354-359. doi: 10.2214/AJR.14.12645.
18. Herráiz-Hidalgo L, Carrascoso-Arranz J, Recio-Rodríguez M, Jiménez-de la Peña M, Cano-Alonso R, Álvarez-Moreno E, et al. Posterior tibial tendon dysfunction: what other structures are involved in the development of acquired adult flat foot? Radiologia. 2014;56(3):247-56. Spanish. doi: 10.1016/j.rx.2011.12.006.
19. Saltzman CL, el-Khoury GY. The hindfoot alignment view. Foot Ankle Int. 1995;16(9):572-576. doi: 10.1177/107110079501600911.
20. Williamson ER, Chan JY, Burket JC, Deland JT, Ellis SJ. New radiographic parameter assessing hindfoot alignment in stage II adult-acquired flatfoot deformity. Foot Ankle Int. 2015;36(4):417-423. doi: 10.1177/1071100714558846.25380772.
21. Sripanich Y, Barg A. Imaging of peritalar instability. Foot Ankle Clin. 2021;26(2):269-289. doi: 10.1016/j.fcl.2021.03.003.
22. Kong A, Van Der Vliet A. Imaging of tibialis posterior dysfunction. Br J Radiol. 2008;81(970):826-386. doi: 10.1259/bjr/78613086.
23. Monteagudo MM, Martínez-de-Albornoz P. Progressive collapsing foot deformity. is there really a johnson and strom stage I? Foot Ankle Clin. 2021;26(3):443-463. doi: 10.1016/j.fcl.2021.05.002.
24. Arnoldner MA, Gruber M, Syré S, Kristen KH, Trnka HJ, Kainberger F, et al. Imaging of posterior tibial tendon dysfunction-Comparison of high-resolution ultrasound and 3T MRI. Eur J Radiol. 2015;84(9):1777-1781. doi: 10.1016/j.ejrad.2015.05.021.
25. Bastias GF, Dalmau-Pastor M, Astudillo C, Pellegrini MJ. Spring ligament instability. Foot Ankle Clin. 2018;23(4):659-678. doi: 10.1016/j.fcl.2018.07.012.
26. Barbachan-Mansur NS, Lalevée M, Lee HY, Ehret A, Fayed A, Mann TS, et al. Influence of weightbearing computed tomography in the progressive collapsing foot deformity classification system. Foot Ankle Int. 2023;44(2):125-129. doi: 10.1177/10711007221141898.
27. de Cesar-Netto C, Barbachan-Mansur NS, Talaski G, Jasper RP, Schmidt E, de Carvalho KAM, et al. From asymptomatic flatfoot to progressive collapsing foot deformity: peritalar subluxation is the main driver of symptoms. J Bone Joint Surg Am. 2025;107(18):2060-2068. doi: 10.2106/JBJS.24.01619.
28. Mengiardi B, Pinto C, Zanetti M. Spring ligament complex and posterior tibial tendon: mr anatomy and findings in acquired adult flatfoot deformity. Semin Musculoskelet Radiol. 2016;20(1):104-115. doi: 10.1055/s-0036-1580616.

JMeXFRI

Journal of the Mexican Federation of Radiology and Imaging

Check for updates

FULL RESEARCH ARTICLE

Radial sclerosing lesions diagnosed by percutaneous breast biopsy: histologic upgrade rate and management implications

*Valeria Belden-Reyes[1,2,a], Maria Guerra-Ayala[3,a], Leyla J. Alanis-Soto[3], Gabriela S. Gomez-Macias[4], Yara G. Flores-Raymundo[4] and Margarita L. Garza-Montemayor[3]**

[1]Department of Diagnostic Imaging, San Jose Hospital and Zambrano Hellion Hospital, Tec Salud; [2]School of Medicine and Health Sciences, Tecnologico de Monterrey; [3]Breast Diagnostic Imaging Center; [4]Breast Pathology Center. San Jose Hospital and Zambrano Hellion Hospital, Tec Salud. Monterrey, Nuevo Leon, Mexico

[a]These authors contributed equally.

ABSTRACT

Introduction: *Management of benign radial sclerosing lesions (RSLs) remains controversial, with no consensus on surgical excision. The aims of this study were to compare the rate of histologic underestimation of high-risk lesions or carcinomas associated with benign RSLs based on breast biopsy method and to determine the upgrade of RSLs after surgical excision, when performed, or during imaging follow-up.* **Material and methods:** *This retrospective cohort study analyzed RSLs in women who underwent percutaneous breast biopsy followed by surgical excision or at least 24 months of imaging surveillance***.** *RSLs were detected by mammography, ultrasound (US) and/or magnetic resonance imaging (MRI) and were confirmed histopathologically. Diagnostic methods included percutaneous ultrasound core needle biopsy (US-CNB), ultrasound vacuum-assisted biopsy (US-VAB), stereotactic vacuum-assisted biopsy (VAB) and/or surgical excision. Histologic diagnoses were benign RSLs, RSLs with high-risk lesions or breast cancer associated.* **Results:** *Ninety-seven women with 97 RSLs were included — 75 with US-CNB and 22 with VAB. The upgrade rate varied by biopsy method. With US-CNB, 8 (10.7%) lesions were upgraded to high-risk lesions after surgical excision and one (1.3%) was upgraded to carcinoma in situ (CIS). Another case (1.3%) had a percutaneous diagnosis of high-risk RSL was upgraded to microinvasive cancer***.** *There were no upgrades to high-risk lesions or cancer in 12 US-VAB cases. All remained stable during follow-up (n = 10, 83.3%) or were confirmed benign surgically (n = 2, 16.7%). Of the 10 RSLs sampled with stereotactic VAB, one (10.0%) was upgraded to a high-risk lesion.* **Conclusion:** *In our study, US-VAB demonstrated no histologic underestimation of malignancy compared with US-CNB or stereotactic VAB. Given this low risk, semiannual imaging for two years is a safe alternative to surgical excision in patients with RSLs diagnosed on percutaneous biopsy.*

Keywords: *Radial sclerosis lesion. Architectural distortion. Breast imaging. Histologic underestimation. Vacuum-assisted breast biopsy. Ultrasound vacuum-assisted biopsy.*

INTRODUCTION

Radial scars and complex sclerosing lesions, often referred to as radial sclerosing lesions (RSLs), are breast lesions with a central fibroelastic core surrounded by entrapped ducts and lobules. Their imaging appearance is architectural distortion[1]. Benign RSL imaging features overlap with those of malignancy and are often targets for imaging-guided biopsy because of their suspicious appearance[1-8]. RSLs can be identified in isolation or associated with atypia or other high-risk lesions with intrinsic malignant potential, increasing the risk of carcinoma and affecting RSL prognosis and management[1].

The increased use of digital breast tomosynthesis (DBT) has led to higher detection of RSLs, prompting renewed discussion of its clinical significance and

***Corresponding author:**
Margarita L. Garza-Montemayor
E-mail: magalygarzam@gmail.com

Received for publication: 04-08-2025
Accepted for publication: 10-10-2025
DOI: 10.24875/JMEXFRI.M26000121

Available online: 16-04-2026
J Mex Fed Radiol Imaging. 2026;5(1):15-24
www.JMeXFRI.com

appropriate management[1,9]. Surgical excision of RSLs has traditionally been recommended due to concerns that associated high-risk lesions or carcinomas might be missed with insufficient sampling[5]. Recent evidence suggests that benign RSLs without atypia have a low underestimation rate, especially when vacuum-assisted biopsy (VAB) is performed[4,9]; this method can be performed with various imaging modalities, including ultrasound (US), stereotaxy, DBT, contrast-enhanced mammography, and magnetic resonance imaging (MRI)[10].

Clinical recommendations for optimal benign RSL management are inconsistent[1,5]. Some authors support routine surgical excision in selected cases after a percutaneous diagnosis of RSLs[3,6,7,11], others advocate conservative approaches, especially when adequate sampling and absence of atypia are ensured[4,5]. In Mexico, there is little data to support evidence-based decisions in this context[12]. The aims of this study were to compare the rate of histologic underestimation of high-risk lesions or carcinomas associated with benign RSLs based on breast biopsy method and to determine the upgrade of RSLs after surgical excision, when performed, or during imaging follow-up.

MATERIAL AND METHODS

This retrospective cohort study was conducted between 2019 and 2022 at the Breast Imaging Departments of San José Hospital and Zambrano Hellion Hospital, Tec Salud, in Monterrey, Nuevo León, Mexico. Inclusion criteria were women aged over 20 with a histopathologic diagnosis of RSL by surgical excision and/or imaging examination follow-up of at least 24 months**.** Cases in which RSL was an incidental finding on histopathologic examination or in which no follow-up data were available were excluded. Informed consent was waived due to the retrospective nature of the study and the use of data obtained during routine clinical care. The Institutional Research and Ethics Committees approved this study.

Study development and variables

We retrospectively reviewed all RSL cases identified by mammography, US, or MRI and confirmed by core needle biopsy (CNB) or VAB using electronic image records from a Picture Archiving and Communication System (PACS) (Carestream, Philips, Rochester, NY, USA).

Age, Breast Imaging Reporting and Data System (BI-RADS) categories, and histopathology results of percutaneous and excisional biopsies were recorded. Women diagnosed with benign RSLs were enrolled in a systematic imaging follow-up protocol of two years. Patients with benign RSLs associated with high-risk lesions or breast carcinoma were referred for definitive surgical treatment.

Image acquisition and analysis

Mammograms were performed using either the Selenia Dimensions™ system (Hologic, Inc., Bedford, MA, USA) or the IMS Giotto Tomo Digital Mammography system (IMS, Sasso Marconi, BO, Italy). After mammography, a US examination of the breast was performed using the iU22, EPIC 7G, or EPIC 7W systems (Philips Co., Bothell, WA, USA) equipped with linear multifrequency transducers. Imaging examination was performed in grayscale, color Doppler, and power Doppler US modes. BI-RADS 5th Edition categories were assigned based on mammography and US findings[13].

Breast biopsy

US-guided percutaneous biopsies (US-CNB and US-VAB) and stereotactic-VAB or excisional biopsy with a marking clip were included. US-CNB was performed with a 12-gauge core needle, obtaining a minimum of ten cores per lesion. VABs were performed with a vacuum-assisted 10-gauge biopsy needle under US or stereotactic guidance. All percutaneous biopsies were performed in a minor procedure unit with topical anesthesia. All CNB and VAB biopsies were performed by breast radiologists averaging 16 years of experience (range 7 to 25 years).

Excisional biopsies were performed by a breast surgeon under general anesthesia in an operating room. The tissue samples were submitted to the Department of Pathology for histopathologic evaluation by a breast pathology subspecialist (GGM) with 13 years of experience. Histopathology results were classified as benign, high-risk lesions – including atypical ductal hyperplasia, papillary lesions, and lobular neoplasia – or malignant breast lesions.

Statistical analysis

Numeric variables are described using measures of central tendency and dispersion (standard deviation). Categorical variables are reported as absolute frequencies and percentages. The association between categorical variables was examined using the chi-square test.

A p value < 0.05 was statistically significant. SPSS version 25 (IBM Corp., Armonk, NY, USA) was used for statistical analyses.

RESULTS

We examined 4,715 percutaneous biopsies performed during the study period. One hundred and ten cases were identified as RSL by percutaneous biopsy. Thirteen RSLs were excluded because of ipsilateral breast cancer (n = 9) or no images were available (n = 4). We included 97 women with 97 RSLs. Asymptomatic women were referred from the screening program (n = 61, 62.9%) or a diagnostic examination (n = 36, 37.1%).

Comparison of percutaneous biopsy methods and histopathologic diagnosis in 97 women with RSLs

The patients' ages ranged from 24 to 73 years, with a mean of 47.8 ± 9.5 years (range 24 to 73) (Table 1). RSLs were identified as architectural distortion alone or, in some cases, were associated with calcifications, focal asymmetry, a mass, or non-mass lesions. According to the BI-RADS classification, most lesions were 4B (n = 77, 79.4%), followed by 4A (n = 11, 11.3%) and 4C (n = 9, 9.3%). All 97 women with a diagnosis of RSL underwent a percutaneous biopsy. The most common method was US-CNB (n = 75, 77.3%) followed by US-VAB (n = 12, 12.4%), and stereotactic VAB (n = 10, 10.3%).

Histopathology of percutaneous biopsies showed benign RSLs in 77 (79.4%) of 97 cases. High-risk RSLs were identified in 18 (18.6%), mainly papillary lesions (n = 9) and atypical ductal hyperplasia (n = 7). Carcinoma in situ (CIS) was found in 1 (1.0%) case, and microinvasive carcinoma in 1 (1.0%) case of RSL.

Sixty-eight (70.1%) of the 97 women underwent surgical excision with wire localization. Benign RSLs were confirmed in 45 (66.2%) cases, while high-risk RSLs were found in 19 (27.9%), CIS in 3 (4.4%), and malignant microinvasive carcinoma in 1 (1.5%).

Figures 1 and 2 show breast architectural distortion on mammography of an asymptomatic 46-year-old woman. Contrast-enhanced breast MRI shows a non-mass lesion associated with architectural distortion. A US-CNB was performed, and the histopathologic diagnosis was benign RSL.

Table 1. Comparison of percutaneous biopsy methods and histopathology diagnosis in 97 women with RSL

Description	Parameter
Age (years), mean ± SD (min-max)	47.8 ± 9.5 (24-73)
BI-RADS, n (%)	
4A	11 (11.3)
4B	77 (79.4)
4C	9 (9.3)
Percutaneous biopsy method, n (%)	
US-CNB	75 (77.3)
US-VAB	12 (12.4)
Stereotactic VAB	10 (10.3)
Histopathologic diagnosis by percutaneous biopsy, n (%)	
Benign RSL	77 (79.4)
RSL with associated high-risk lesions	18 (18.6)
RSL with associated CIS	1 (1.0)
RSL with associated microinvasive carcinoma	1 (1.0)
Histopathology diagnosis after surgical excision[a], n (%)	
Benign RSL	45 (66.2)
RSL with associated high-risk lesions	19 (27.9)
RSL with associated CIS	3 (4.4)
RSL with associated microinvasive carcinoma	1 (1.5)

[a]Only 68 (70.1%) of 97 women.
BI-RADS: Breast Imaging Reporting and Data System; RSL: radial sclerosing lesion; US-CNB: ultrasound-guided core needle biopsy; US-VAB: ultrasound-guided vacuum-assisted biopsy; VAB: vacuum-assisted biopsy; CIS: carcinoma in situ.

Upgrade rate of RSLs related to the percutaneous breast biopsy method

Regarding biopsy methods, 75 (77.3%) of the 97 RSLs were sampled using ultrasound-guided 12-gauge spring-loaded core needle devices (US-CNB), while 12 (12.4%) cases were performed using US-VAB, and 10 (10.3%) with stereotactic VAB (Table 2). Sixty-eight (70.1%) of the 97 cases underwent surgical excision, and 29 (29.9%) underwent semiannual imaging examination for at least 24 months. None of the RSLs that were followed with imaging showed suspicious interval changes of RSL upgrade. They were classified as benign at the end of the follow-up period.

The overall histologic upgrade rate for benign RSL varied by biopsy method. In US-CNB, 8 (10.7%) of 75 RSLs were upgraded to high-risk after surgical excision, one (1.3%) was upgraded to CIS, and another (1.3%) had a percutaneous diagnosis of a high-risk

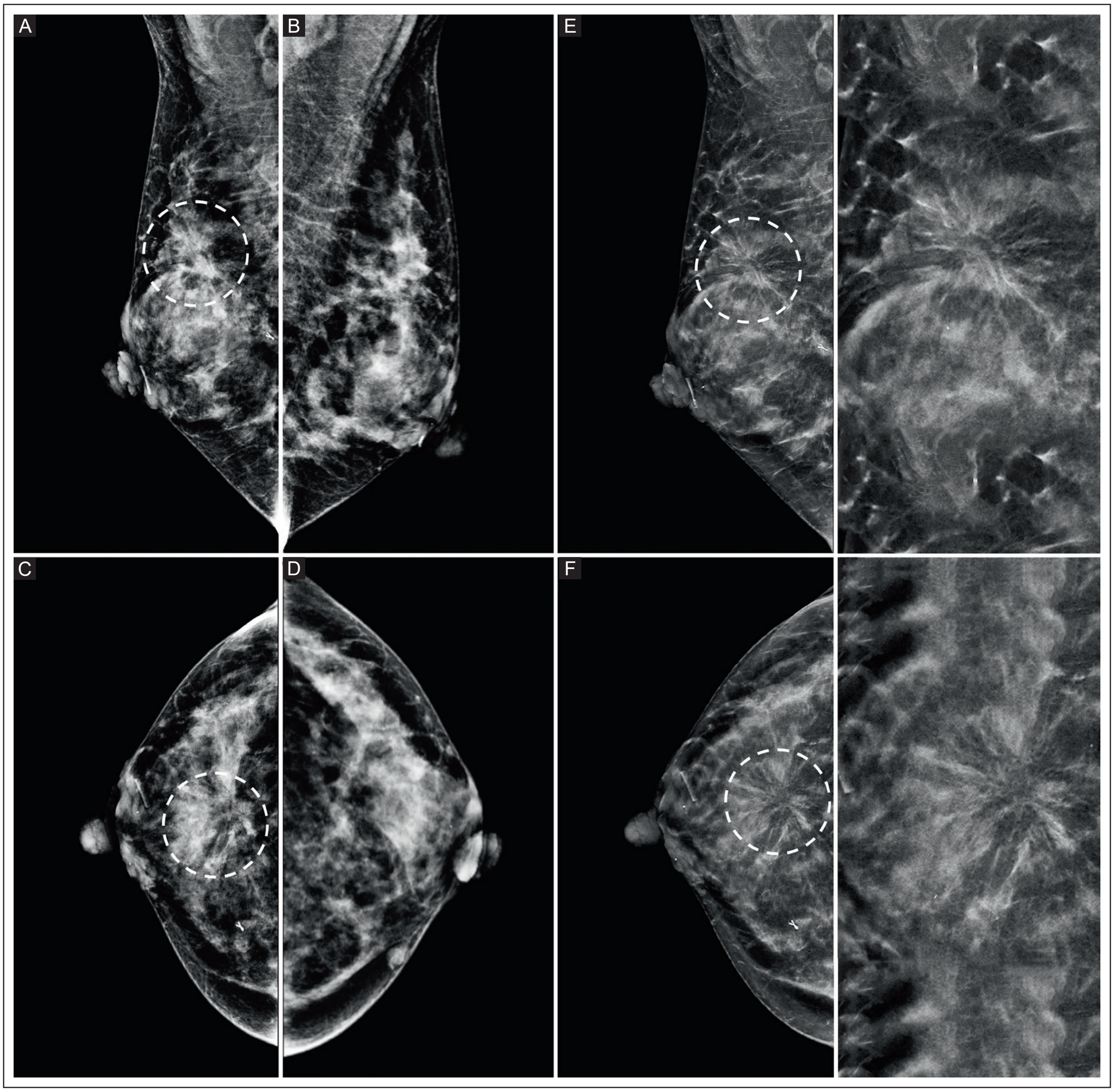

Figure 1. An asymptomatic 46-year-old woman with a positive family risk factor for breast cancer. She had a history of a percutaneous biopsy of the right breast that reported a benign intraductal papilloma, BI-RADS 4A. **A, B, C, D:** bilateral mammography, MLO and CC views of the right breast show extremely dense breast tissue (category d) with an area of architectural distortion at the junction of the upper quadrants (dashed circles), with no suspicious lesions in the left breast. **E-F:** DBT, MLO, and CC views and digital magnifications of the right breast show better delineation of architectural distortion (dashed circles).

DBT: digital breast tomosynthesis; MLO: mediolateral oblique; CC: craniocaudal; BI-RADS: Breast Imaging Reporting and Data System.

RSL that was subsequently upgraded to microinvasive cancer.

No histologic RSL upgrades to high-risk or cancer were found in the 12 cases diagnosed with US-VAB. These lesions remained stable during follow-up (n = 10, 83.3%) or were confirmed benign after surgical excision (n = 2, 16.7%). Of the 10 RSLs sampled with stereotactic VAB, one (10.0%) was upgraded to a high-risk lesion, while none were upgraded to cancer. US-VAB was the sampling method with no histologic underestimation of high-risk lesions or malignancy compared to the other methods (US-CNB or stereotactic VAB).

Figure 3 shows a 50-year-old woman with a percutaneous CNB with architectural distortion, BI-RADS 4C, with discordance between imaging and pathology. The histopathology report identified fibrosis and non-atypical proliferative changes. Contrast-enhanced breast MRI shows a non-mass lesion with architectural

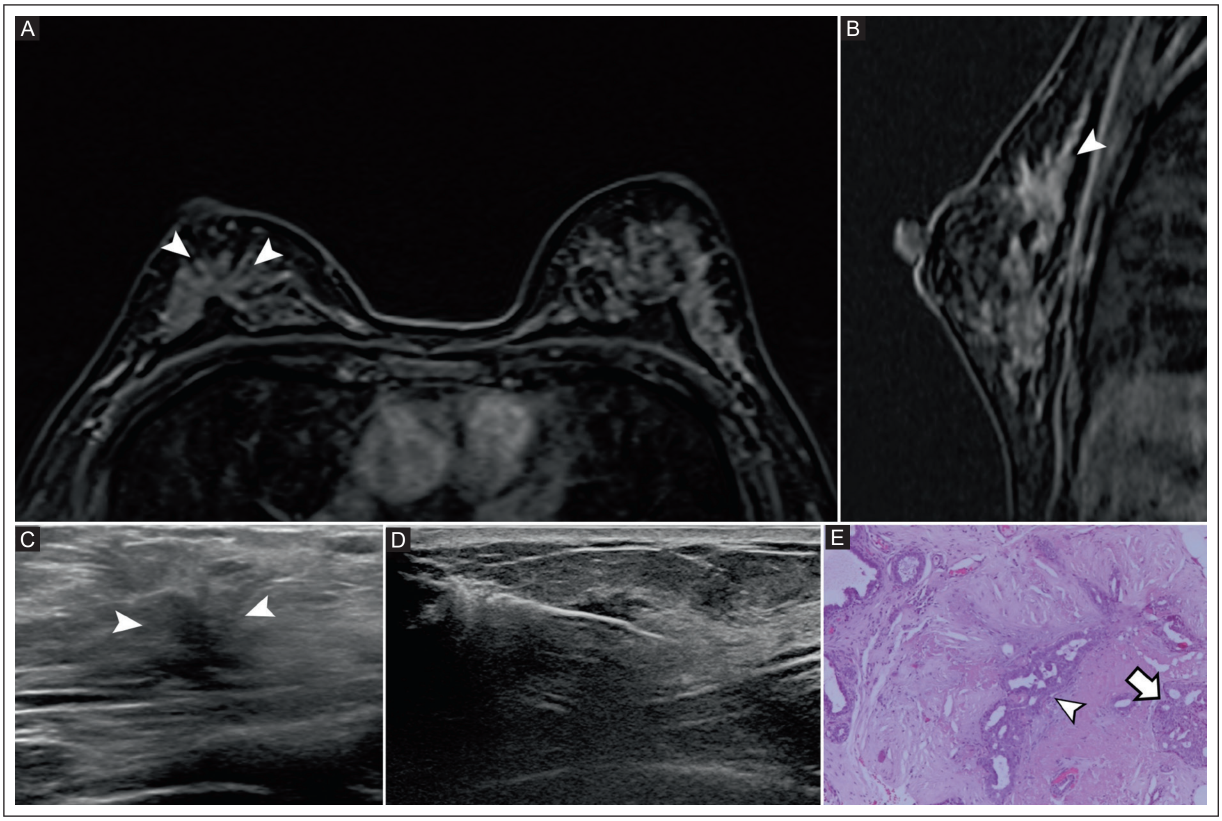

Figure 2. The same patient as in Figure 1. **A-B:** a contrast-enhanced breast MRI shows a non-mass lesion associated with architectural distortion at the junction of the upper quadrants of the right breast at 11 o'clock in the middle third of the breast (arrowheads). **C:** grayscale US, radial view, shows a poorly defined hypoechoic area with architectural distortion without posterior acoustic shadowing (arrowheads). **D:** US-CNB was performed targeting the lesion. **E:** histology section with 10X H&E staining shows distorted tubules within a background of diffuse fibrosis (arrowhead), with moderate usual ductal hyperplasia toward the periphery (arrow). The histopathology diagnosis was a benign RSL.

US-CNB: ultrasound-guided core needle biopsy; H&E: hematoxylin and eosin; RSL: radial sclerosing lesion; MRI: magnetic resonance imaging.

Table 2. Comparison of RSL histologic upgrade by percutaneous biopsy method

Description	Total (n = 97)	US-CNB (n = 75)	US-VAB (n = 12)	Stereotactic-VAB (n = 10)
No upgrade of RSLs, n (%)				
Surgical excision[a]	57	51 (68.0)	2 (16.7)	4 (40.0)
≥ 24 months imaging follow-up	29	14 (18.7)	10 (83.3)	5 (50.0)
Histologic upgrade of RSLs after surgical excision, n (%)				
RSL to risk lesion	9	8 (10.7)	0	1 (10.0)
RSL with associated risk lesion to CIS	1	1 (1.3)	0	0
RSL to microinvasive cancer	1	1 (1.3)	0	0

[a] Only 68 (70.1) of 97 women.

RSL: radial sclerosing lesion; CIS: carcinoma in situ; US-CNB: ultrasound-guided core needle biopsy; US-VAB: ultrasound-guided vacuum-assisted biopsy; VAB: vacuum-assisted biopsy.

distortion, associated with three hyperenhanced irregular solid masses. Grayscale US shows a hypoechoic mass with minimal posterior acoustic shadowing and associated architectural distortion. The diagnosis was RSL with atypical ductal hyperplasia. Figure 4 shows a mammogram of a 42-year-old woman with architectural distortion, BI-RADS 4B. Figure 5 shows a contrast-enhanced breast MRI with non-mass enhancement

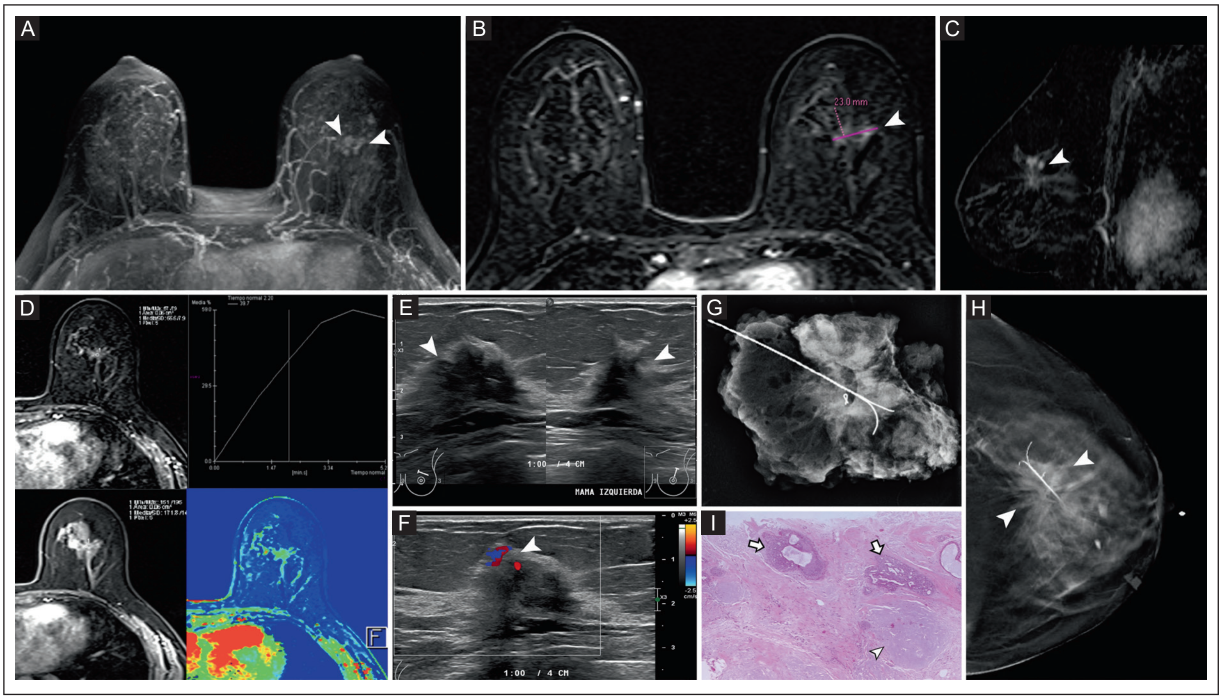

Figure 3. A 50-year-old woman with a recent percutaneous CNB of an architectural distortion in the left breast, BI-RADS 4C, with discordance between the imaging findings and the histopathology report. **A, B, C, D:** contrast-enhanced breast MRI shows a non-mass lesion with architectural distortion at 12 o'clock associated with three hyperenhanced irregular solid masses. The largest is 7 mm in diameter (arrowheads). Functional assessment shows a kinetic curve with persistent type I enhancement. **E-F:** grayscale US shows a hypoechoic mass with minimal posterior acoustic shadowing and associated architectural distortion at 12 o'clock (arrowheads). Color Doppler US examination shows minimal peripheral vascularity. **G:** X-ray of the specimen confirms excision of the targeted breast lesion. **H:** DBT, CC view of the left breast shows stereotactic VAB wire localization with accurate placement in architectural distortion (arrowheads). **I:** histologic section with H&E 5X staining shows a sclerotic stroma with tubular entrapment (arrowhead). At the periphery, there are distended ducts with focal rigid lumens and others with slit-like lumens, containing a single population of cells in focal areas (arrows). The histopathology diagnosis was RSL associated with atypical ductal hyperplasia.

DBT: digital breast tomosynthesis; CNB: core needle biopsy; CC: craniocaudal; H&E: hematoxylin and eosin; RSL: radial sclerosing lesion; BI-RADS: Breast Imaging Reporting and Data System; US: ultrasound; MRI: magnetic resonance imaging; VAB: vacuum-assisted biopsy.

with architectural distortion showing a clumped enhancement pattern. Stereotactic VAB was performed. The diagnosis was RSL with CIS.

DISCUSSION

The overall histologic upgrade rate of RSLs in our study varied by biopsy method. US-VAB was the most reliable diagnostic approach for benign RSLs with no histologic underestimation of high-risk lesions or malignancy compared with the other biopsy methods (US-CNB or stereotactic VAB). In addition, semiannual imaging follow-up for two years was a safe alternative to surgical excision in selected patients.

VAB minimizes histologic underestimation of RSLs and can reduce the need for surgical excision when appropriately used[3-5,9,14]. Ferreira et al.[7] found a significantly lower histologic upgrade rate with VAB (4.0%; 1/25) compared to CNB (23.9%; 16/67) in a retrospective study in Portugal involving 113 women with RSL diagnosed by percutaneous biopsy (p = 0.041). The authors concluded that RSLs without atypia, when adequately sampled by VAB, represent a low-risk subgroup in whom clinical surveillance could be a safe alternative, potentially avoiding surgical excision. In our study, the overall histologic upgrade rate of RSLs varied by biopsy method. RSLs sampled using US-CNB had a higher histologic upgrade rate (13.3%, 10/75 cases). With stereotactic VAB, only one lesion, which was an atypical papilloma (10.0%, 1/10 cases), was upgraded to a high-risk lesion. There was no histologic upgrade in 12 RSL cases with US-VAB, suggesting that this method may provide a more accurate histologic diagnosis. Our results are consistent with the recommendation that VAB is an ideal alternative for managing RSLs without atypia in selected cases, especially when there is concordance between

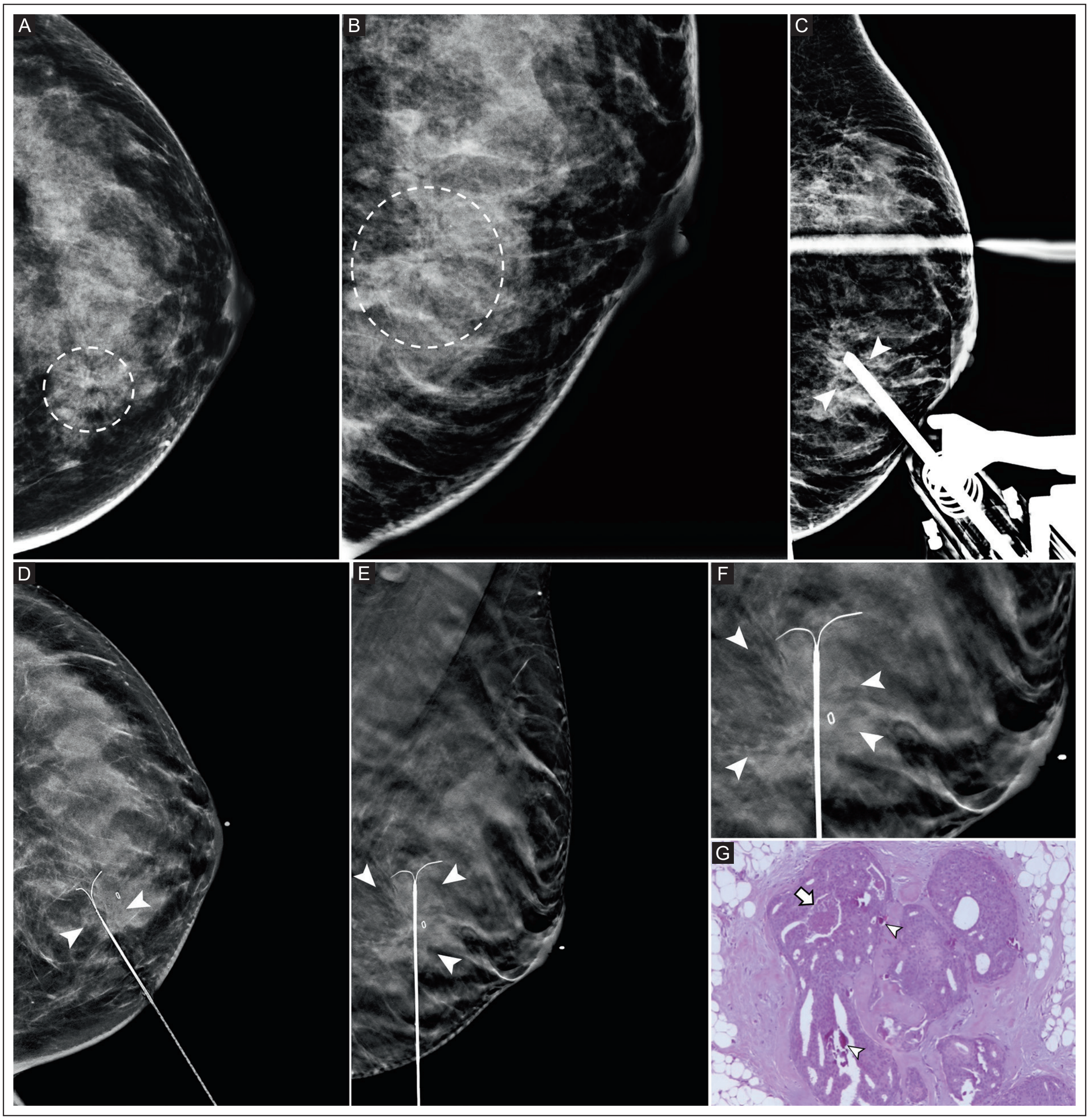

Figure 4. A 42-year-old woman with an architectural distortion seen at mammography in the left breast. **A:** mammography, CC view of the left breast, showing an area of architectural distortion in the lower inner quadrant, associated with scattered microcalcifications (dashed circle), BI-RADS 4B. **B:** a magnified CC view with left breast compression shows better delineation of the architectural distortion (dashed circle). **C:** a stereotactic VAB was performed (arrowheads). **D, E, F:** preoperative wire localization with DBT (arrowheads). **G:** histologic section with H&E 10X staining shows central sclerosis with tubular distortion and marked intraductal dilatation, along with severe atypia, focal necrosis (arrow) with microcalcifications (arrowhead), and myoepithelial cell preservation. The histopathology diagnosis was CIS-associated RSL.

DBT: digital breast tomosynthesis; CC: craniocaudal; H&E: hematoxylin and eosin; RSL: radial sclerosing lesion; CIS: carcinoma in situ; BI-RADS: Breast Imaging Reporting and Data System. VAB: vacuum-assisted biopsy.

radiologic and pathologic diagnosis[5,15]. The diagnostic reliability of VAB supports its role as a conservative approach in managing select cases of RSLs. Our results support a tailored approach to RSL management and emphasize the importance of the biopsy method in clinical decision-making. VAB could be a cost-effective alternative to the recommended excisional biopsy in certain cases[16].

With the introduction of population-based breast cancer screening programs and the increasing use of DBT, the detection rate of RSLs has increased in recent years, with a reported incidence of 0.03% to 0.09%[7].

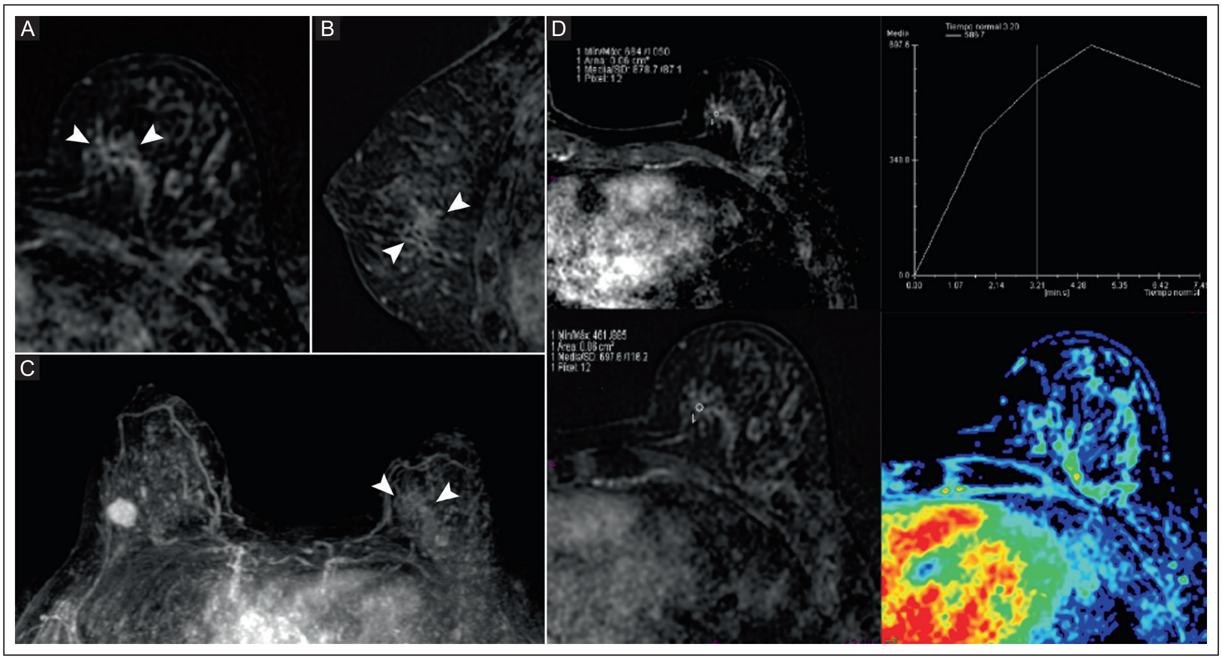

Figure 5. The same patient as in figure 4. **A-B:** contrast-enhanced breast MRI with axial and sagittal T1- weighted fat-saturated postcontrast subtraction shows non-mass enhancement with associated architectural distortion (arrowheads) at the junction of the inner quadrants of the left breast, at 3 o'clock. It shows a clumped enhancement pattern. **C:** axial MIP image shows a hyperenhanced area of architectural distortion at the junction of the inner quadrants of the left breast at 3 o'clock (arrowheads). A previously known fibroadenoma is seen in the right breast. **D:** functional MRI evaluation of the lesion shows a type 3 kinetic plateau curve. The histopathology diagnosis was CIS-associated RSL.

MIP: maximum intensity projection; MRI: magnetic resonance imaging.

On the other hand, prevalence varied in the literature, ranging from 6.2 to 29%[17]. However, the histologic upgrade rate to malignancy at surgical excision has remained low (3-6%), suggesting that the vast majority of RSLs diagnosed by CNB are benign. Only a small proportion are associated with high-risk lesions or breast malignancy[4,5]. Yan et al.[14] found benign RSLs in 117 (80.1%) of 146 RSLs in 142 American women examined with mammography and DBT, while 29 (19.9%) RSLs were associated with atypia. A low rate (0.9%) of histologic upgrade to malignancy was reported. Sherwell-Cabello et al.[12] examined 123 Mexican women in a retrospective study. They found RSL associated with breast cancer in 1.6% of cases. In our study, the prevalence of benign RSL diagnosed by percutaneous biopsy was 79.4% (n = 77), a finding comparable to other studies[4,14]. High-risk lesions were associated with RSLs in 18 cases (18.6%). Breast cancer was found in 2 (2.1%) of 97 cases, which is also comparable to other studies[2,7,14,17] that reported similar frequencies of high-risk lesions and very low rates of carcinoma associated with RSLs. The high prevalence of benign RSLs without atypia suggests that imaging examination surveillance may be appropriate[4,18].

Earlier studies by Berg et al.[8] and Aroner et al.[19] reported higher rates of discordance and upgrades in RSLs, leading to recommendations for routine excision. In 2002, Brenner et al.[6] advocated conservative management of RSLs without concomitant atypia. They found that there was no increase in malignancy when lesions were sampled with VAB or CNB using at least 12 cores. If these conditions were not met, surgical excision is recommended[6]. Later reports,[4,7,18] have shown that the accuracy of CNB can improve with modern imaging methods and multidisciplinary evaluation, supporting more conservative management strategies in increasing confidence in percutaneous biopsy results[4,17,18,20,21]. Extensive samples obtained by percutaneous biopsy may spare a patient from undergoing surgical excision, as they are more representative of the lesion*.* Our study showed high concordance between US-CNB and surgical excision for benign RSLs, supporting the diagnostic reliability of percutaneous biopsy when adequately sampled[3,9]. Consensus statements and guidelines, including those by Elfgen et al.[5] and Rubio et al.[18], also advocate individualized management and acknowledge that excision may be unnecessary for benign RSLs without atypia with concordance between imaging and pathology[5,18]. Comparable results of benign RSLs diagnosed by CNB were rarely upgraded after excision[2,7,22]. CNB is a sufficient diagnostic tool in selected cases where CNB findings and imaging are concordant, suggesting that surgical excision may not provide additional diagnostic value. Benign RSLs on CNB, especially when performed by experienced breast radiologists with adequate sampling and interpreted by experienced pathologists with adequate imaging and pathologic concordance, may not require surgical excision and could continue routine clinical and close imaging follow-up.

The strengths of our study include standardized biopsy protocols, US-VAB performed by experienced breast radiologists, and systematic two-year imaging follow-up to ensure diagnostic accuracy. In addition, there was high concordance between radiology and pathology results based on the European B3 guidelines and the international consensus, supporting the safety of non-surgical management for appropriately selected patients[2,5,18]. Several limitations of our study are related to the small sample size and insufficient power to determine the statistical significance of the type of percutaneous biopsy in relation to the absence of histologic upgrading. The retrospective study design, with non-random case selection, may introduce selection bias and limit the generalizability of the results. In addition, not all benign RSLs were surgically removed in our study, preventing a full assessment of potential underestimation in the entire cohort.

CONCLUSION

Our study showed that US-VAB is a reliable diagnostic approach for benign RSLs and may reduce the risk of histologic underestimation. Furthermore, semiannual imaging surveillance of benign RSLs for at least 2 years is a safe alternative to surgical excision in selected patients with radiologic–pathologic concordance. This study provides valuable insights into the management of RSLs in a Mexican cohort and highlights the diagnostic performance of VAB, particularly in patients presenting with architectural distortion. In selected concordant cases, systematic imaging follow-up represents a reliable alternative to excision.

Acknowledgments

The authors thank Professor Ana M. Contreras-Navarro for her guidance in preparing and writing this scientific paper.

Funding

The authors declare that they have not received funding.

Conflicts of interest

The authors declare no conflicts of interest.

Ethical considerations

Protection of human subjects and animals. The authors declare that the procedures followed were in accordance with the ethical standards of the responsible committee on human experimentation and with the World Medical Association and the Declaration of Helsinki (1964) and subsequent amendments.

Confidentiality, informed consent, and ethical approval. The authors have obtained approval from the Ethics Committee for the analysis of routinely collected and anonymized clinical data; therefore, individual informed consent was not required. Relevant ethical recommendations have been followed.

Declaration on the use of artificial intelligence*.* The authors declare that no generative artificial intelligence was used in the writing or creation of the content of this manuscript.

REFERENCES

1. Manzar BZ, Phillips J, Dibble EH, Quintana LM, Lourenco AP. Imaging and management of radial scars and complex sclerosing lesions. RadioGraphics. 2023;43(10):e230022. doi: 10.1148/rg.230022.
2. Donaldson AR, Sieck L, Booth CN, Calhoun BC. Radial scars diagnosed on breast core biopsy: Frequency of atypia and carcinoma on excision and implications for management. Breast. 2016;30:201-207. doi: 10.1016/j.breast.2016.06.007.
3. Quinn EM, Dunne E, Flanagan F, Mahon S, Stokes M, Barry MJ, et al. Radial scars and complex sclerosing lesions on core needle biopsy of the breast: upgrade rates and long-term outcomes. Breast Cancer Res Treat. 2020;183(3):677-682. doi: 10.1007/s10549-020-05806-z.
4. Polat DS, Seiler SJ, Goldberg J, Arya R, Knippa EE, Goudreau SH. Radial scars without atypia diagnosed at percutaneous core needle breast biopsy: support for imaging surveillance. Eur J Breast Health. 2023;19(1):76-84. doi: 10.4274/ejbh.galenos.2022.2022-9-3.
5. Elfgen C, Leo C, Kubik-Huch RA, Muenst S, Schmidt N, Quinn C, et al. Third International Consensus Conference on lesions of uncertain malignant potential in the breast (B3 lesions). Virchows Arch. 2023;483(1): 5-20. doi: 10.1007/s00428-023-03566-x.
6. Brenner RJ, Jackman RJ, Parker SH, Evans WP 3rd, Philpotts L, Deutch BM, et al. Percutaneous core needle biopsy of RSLs of the breast: when is excision necessary? AJR Am J Roentgenol. 2002;179(5):1179-1184. doi: 10.2214/ajr.179.5.1791179.
7. Ferreira AI, Borges S, Sousa A, Ribeiro C, Mesquita A, Martins PC et al. Radial scar of the breast: Is it possible to avoid surgery? Eur J Surg Oncol. 2017;43(7):1265-1272. doi: 10.1016/j.ejso.2017.01.238.
8. Berg JC, Visscher DW, Vierkant RA, Pankratz VS, Maloney SD, Lewis JT, et al. Breast cancer risk in women with RSLs in benign breast biopsies. Breast Cancer Res Treat. 2008;108(2):167-174. doi:10.1007/s10549-007-9605-9.
9. Chou WYY, Veis DJ, Aft R. Radial scar on image-guided breast biopsy: is surgical excision necessary? Breast Cancer Res Treat. 2018;170(2): 313-320. doi: 10.1007/s10549-018-4741-y.

10. Imschweiler T, Haueisen H, Kampmann G, Rageth L, Seifert B, Rageth C, et al. MRI-guided vacuum-assisted breast biopsy: comparison with stereotactically guided and ultrasound-guided techniques. Eur Radiol. 2014; 24(1):128-135. doi: 10.1007/s00330-013-2989-5.
11. Phantana-Angkool A, Forster MR, Warren YE, Livasy CA, Sobel AH, Beasley LM, et al. Rate of radial scars by core biopsy and upgrading to malignancy or high-risk lesions before and after introduction of digital breast tomosynthesis. Breast Cancer Res Treat. 2019;173(1):23-29. doi: 10.1007/s10549-018-4973-x.
12. Sherwell-Cabello S, Maffuz-Aziz A, Domínguez-Reyes C, Peralta-Casillo G, Cavazos-García R, Rodríguez-Cuevas S. Cicatriz radial y su asociación con carcinomas mamarios: experiencia en una institución privada de enfermedades de la mama. Ginecol Obstet Mex. 2016;84(10): 621-629.
13. D'Orsi C, Sickles EA, Mendelson EB, Morris EA. Breast imaging reporting and data system: ACR BI-RADS breast imaging atlas. 5th Edition. Reston, VA. USA: American College of Radiology. 2013.
14. Yan P, DeMello L, Baird GL, Lourenco AP. Malignancy upgrade rates of radial sclerosing lesions at breast cancer screening. Radiol Imaging Cancer. 2021;3(6):e210036. doi: 10.1148/rycan.2021210036.
15. Rubio IT, Wyld L, Marotti L, Athanasiou A, Regitnig P, Catanuto G, et al. European guidelines for the diagnosis, treatment and follow-up of breast lesions with uncertain malignant potential (B3 lesions) developed jointly by EUSOMA, EUSOBI, ESP (BWG) and ESSO. Eur J Surg Oncol. 2024;50(1):107292. doi: 10.1016/j.ejso.2023.107292.
16. Bao JJ, Jaskowiak NT. Clinical management of RSL without atypia diagnosed on core needle biopsy. Ann Breast Surg. 2021;5:6. doi:10.21037/abs-20-85.
17. Martaindale S, Omofoye TS, Teichgraeber DC, Hess KR, Whitman GJ. Imaging follow-up versus surgical excision for radial scars identified on tomosynthesis-guided core needle biopsy. Acad Radiol. 2020;27(3): 389-394. doi: 10.1016/j.acra.2019.05.012.
18. Reyes A, Sun L, Ha R, Desperito E, Brown M, Francescone MA, et al. comprehensive assessment of radial scars on core needle biopsy in patients with or without breast cancer: upgrade rate and implications on management. Clin Breast Cancer. 2024;24(4):e273-e278. doi: 10.1016/j.clbc.2024.01.020.
19. Aroner SA, Collins LC, Connolly JL, Colditz GA, Schnitt SJ, Rosner BA, et al. RSLs and subsequent breast cancer risk: results from the Nurses' Health Studies. Breast Cancer Res Treat. 2013;139(1):277-285. doi: 10.1007/s10549-013-2535-9.
20. Pujara AC, Hui J, Wang LC. Architectural distortion in the era of digital breast tomosynthesis: outcomes and implications for management. Clin Imaging. 2019;54:133-137. doi: 10.1016/j.clinimag.2019.01.004.
21. Crowley C, Bahl M. Radial scars on screening digital breast tomosynthesis: upstaging rates and management strategies. AJR Am J Roentgenol. 2024;222(6):e2430845. doi: 10.2214/AJR.24.30845.
22. Grabenstetter A, Brennan SB, Jochelson MS, Brogi E, Morrow M, Tan LK, et al. Radial sclerosing lesions found on core needle biopsy: excision can be safely avoided. Histopathology. 2024;85(3):397-404. doi: 10.1111/his.15233.

JMeXFRI

Journal of the Mexican Federation
of Radiology and Imaging

Check for updates

FULL RESEARCH ARTICLE

Strain ratio elastography for predicting malignant breast lesion: a new grading classification

Roberto A. Sandoval-Villanueva[1,2,a], *Karla A. Lopez-Rodríguez*[1,2,a], *David F. Perez-Montemayor*[1,2]*
and Karla G. Garcia-Alvarez[3]

[1]Centro de Imagenologia Integral IMAX Tampico; [2]Instituto de Estudios Superiores de Tamaulipas, Universidad Anahuac; [3]Pathogen Pathology Laboratory, Hospital Beneficencia Española de Tampico. Tampico, Tamaulipas, México

[a]These authors contributed equally.

ABSTRACT

Introduction: *Strain ratio elastography (SRE) lacks a standard classification to establish a cutoff value for predicting malignant breast lesions. This study proposes a new three-grade classification based on SRE cutoff values using the LOGIQ E9 GE Healthcare system and evaluates its diagnostic performance in predicting breast lesion malignancy.* **Material and Methods***: This retrospective cross-sectional study included women with Breast Imaging Reporting and Data System (BI-RADS) breast lesions categories 4 or 5. All lesions were evaluated with conventional ultrasound (US) and strain elastography (SE) with a GE Healthcare LOGIQ E9 system. The semiquantitative three-grade classification cutoff values defined arbitrarily based on SRE were grade 1 (0-1.9, soft pattern), grade 2 (2.0-3.9, intermediate pattern), and grade 3 (4.0-6, hard pattern). Histopathologic diagnosis was the gold standard. Receiver operating characteristic (ROC) analysis was used to compare SRE cutoffs ≥ 2 and ≥ 4.* **Results:** *Of 173 breast lesions, 73 (42.0%) were benign, and 100 (58.0%) were malignant. Benign lesions were primarily grade 1 (42.0%) and 2 (33.0%), while 71% of malignant lesions were grade 3 ($p < 0.001$). The median SRE cutoff value was higher in malignant (5.2) than in benign lesions (2.4) ($p < 0.001$). A cutoff ≥ 2 showed high sensitivity (93.0%) and low specificity (42.4%) for predicting malignant breast lesions, whereas a value ≥ 4 showed a sensitivity of 71.0%, a specificity of 75.3%, and an accuracy of 72.8%.* **Conclusion***: The proposed SRE three-grade classification demonstrated that a grade 3 hard pattern (cutoff ≥ 4) as defined by the GE Healthcare LOGIQ E9 system achieved good diagnostic performance for predicting malignant BI-RADS 4 or 5 breast lesions; it is useful for characterizing breast lesions.*

Keywords: *Ultrasound elastography. Strain elastography. Breast cancer. Breast Imaging Reporting and Data System.*

INTRODUCTION

Ultrasound (US) elastography is a non-invasive method for assessing tissue stiffness. It is used as a supplement to US to improve diagnostic performance, and it is available as a feature on many US units[1]. There are currently two elasticity measurement methods: strain elastography (SE), which measures tissue stiffness via lesion compressibility, and shear wave elastography, which measures the propagation speed of shear waves as they pass through tissue. An acoustic force produces these waves. Stiffness is typically displayed as a color scale or grayscale. There are three semiquantitative SE stiffness measures: the elastography-to-B-mode length (E/B) ratio, a 5-point color scale (elasticity score), and a strain ratio elastography (SRE) cutoff value. The Breast Imaging Reporting and Data System (BI-RADS) v2025 includes a lexicon that defines criteria and descriptors for elasticity assessment[1].

***Corresponding author:**
David F. Perez-Montemayor
E-mail: dfperez@prodigy.net.mx

Received for publication: 24-10-2025
Accepted for publication: 13-12-2025
DOI: 10.24875/JMEXFRI.M26000123

Available online: 16-04-2026
J Mex Fed Radiol Imaging. 2026;5(1):25-35
www.JMeXFRI.com

Elastography techniques and stiffness values vary by US vendor[1]. Moreover, SRE cutoff values differ between equipment brands[2-9]. A systematic review and meta-analysis were performed to determine the optimal SRE cutoff for predicting malignant breast lesions[9]. The different machine models used in the included studies were Hitachi (n = 23 US equipment), Toshiba (n = 11), Philips (n = 7), Samsung (n = 6), GE Healthcare (n = 6), Siemens (n = 4), Mindray (n = 3), and Esaote MyLab (n = 2). There was no standard SRE cutoff value for predicting malignant breast lesions between these equipment brands. Therefore, the US model and brand can influence the determination of a specific SRE cutoff value[9].

Malignant breast lesions are generally stiffer than benign ones[1,10]. According to the BI-RADS lexicon, elasticity is categorized as soft, intermediate, or hard[1]. However, the SRE cutoff values that distinguish malignancy from benignity are not standardized because of differences in instrument parameters across manufacturers using several commercially available systems[11]. Furthermore, SRE lacks a standardized grading system to establish a cutoff value for predicting malignancy in breast lesions. This study proposes a new grading classification based on the SRE cutoff value using the LOGIQ E9 GE Healthcare system. It evaluates its diagnostic performance in predicting malignancy in BI-RADS category 4 or 5 breast lesions.

MATERIAL AND METHODS

This retrospective, cross-sectional analytical study was conducted from February 2018 to November 2025 at the IMAX Imaging Center in Tampico, Tamaulipas, Mexico. Women with BI-RADS category 4 or 5 breast lesions detected on imaging were included. Histopathologically malignant lesions without a molecular subtype were excluded. Informed consent was not required for this observational study, which used information collected during routine clinical care. The institutional research ethics and research committees approved the study.

Development and study variables

Women undergoing mammography and/or US and breast lesions classified according to BI-RADS 5th edition[12] were evaluated using conventional, color Doppler US, and SRE value by SE. The molecular subtype and the Ki67 value were recorded in malignant lesions. Histopathologic diagnosis was the gold standard.

Definitions

Suspicious breast lesion: findings categorized as BI-RADS 4 or 5 based on mammography and/or US abnormalities[12].

SE: shows the spatial distribution of tissue elasticity properties in a region of interest (ROI) by estimating the strain before and after tissue distortion caused by external or internal forces[13].

SRE: the elasticity of the subcutaneous fat tissue ROI compared to that of the lesion ROI[1].

Image acquisition and analysis protocol

Conventional, color Doppler, and SE US images of suspicious breast lesions were assessed using a GE LOGIQ E9 (GE Healthcare, Milwaukee, WI, USA) equipped with a high-frequency linear ML6-15 MHz transducer; color Doppler and SE US were performed using longitudinal scans. Lesions were classified according to ACR BI-RADS 5th edition[12]. The SE of the breast lesions was performed after acquiring grayscale US images. The ROI encompassed the lesion and the surrounding fat tissue. A color map and a quality analysis were automatically performed by the software, which calculated the semiquantitative SRE of the breast lesion. Only images with optimal compression, as displayed by the quality index, were included. Images were selected and stored in a Picture Archiving and Communication System (PACS) (SYNAPSE, Fujifilm Medical Systems, Morrisville, NC, USA). Image evaluation was performed by a radiologist (DPM) with 35 years of experience.

The SRE cutoff value in the LOGIQ E9 GE is reported as 0.0-6.0, indicating the color distribution index within a circle (ROI) and comparing a lesion to the adjacent fatty tissue[13].

The new three-grade semiquantitative cutoff values based on SRE were defined arbitrarily by the author (DPM): grade 1 (0-1.9, soft pattern), grade 2 (2.0-3.9, intermediate pattern), and grade 3 (4.0-6.0, hard pattern).

Histopathologic diagnosis

Pathology reports were reviewed, including histopathologic diagnoses of benign and malignant lesions. Histologic type and grading of malignant breast lesions were recorded. Tumor histological types were defined according to the World Health Organization classification of breast tumors (5th edition)[14]. Histopathologic grading was performed using the modified Bloom-Richardson grading system[15]. Histopathologic assessment was performed by a pathologist (KGA) with 13 years of experience.

Table 1. Three-grade classification[a] by SRE and histopathologic diagnosis of breast lesions

Description	n	SRE Grade 1 (soft pattern)	SRE Grade 2 (intermediate pattern)	SRE Grade 3 (hard pattern)
Benign breast diagnosis, n (%)				
Fibroadenoma	37	13 (35.2)	17 (45.9)	7 (18.9)
Ductal hyperplasia without atypia	3	1 (33.3)	1 (33.3)	1 (33.3)
Adenosis	9	7 (77.8)	1 (11.1)	1 (11.1)
Fibrosis	9	5 (55.6)	2 (22.2)	2 (22.2)
Chronic mastitis	11	3 (27.3)	2 (18.1)	6 (54.6)
Fibroadenomatous changes	1	0	1 (100)	0
Columnar cell changes	1	1 (100)	0	0
Ductal hyperplasia with atypia	1	0	0	1 (100)
Intraductal papilloma	1	1 (100)	0	0
Total, n (%)	73	31 (42.5)	24 (32.9)	18 (24.6)
Malignant breast diagnosis, n (%)				
Invasive ductal carcinoma	71	4 (5.6)	14 (19.7)	53 (74.7)
Invasive lobular carcinoma	14	0	2 (14.3)	12 (85.7)
Cribriform carcinoma	2	1 (50.0)	1 (50.0)	0
Papillary carcinoma	2	0	1 (50.0)	1 (50.0)
Mucinous carcinoma	3	0	0	3 (100)
Ductal carcinoma in situ	7	2 (28.6)	4 (57.1)	1 (14.3)
Tubular carcinoma	1	0	0	1 (100)
Total, n (%)	100	7 (7.0)	22 (22.0)	71 (71.0)

[a]Grade 1 with an SRE cutoff of 0 to 1.9; grade 2 with an SRE of 2.0 to 3.9; and grade 3 with an SRE of 4.0 to 6.
SRE: strain ratio elastography.

Immunohistochemical molecular subtypes

Molecular subtypes were determined according to the 2013 St. Gallen International Expert Consensus[16]: estrogen receptor (ER) expression, progesterone receptor (PR) expression, human epidermal growth factor receptor 2 (HER2) expression, and the cell proliferation index (Ki67). Malignant tumors were classified into five molecular subtypes: luminal A (HER2+ and/or PR+, HER2– and Ki67 < 14%; luminal B/HER2– (ER+ and/or PR+, HER2–, Ki67 ≥ 14%)); luminal B/HER2+ (ER+ and/or PR+, HER2+, any Ki67); HER2+ (ER–, PR–, HER2+); and triple negative breast cancer (ER–, PR–, HER2–).

Statistical analysis

Measures of central tendency (median) and dispersion (interquartile range, IQR) were calculated for quantitative variables. Benign and malignant breast lesions were compared with the Mann–Whitney U test. Qualitative variables were summarized as absolute frequencies and percentages. Categorical variable associations were evaluated with the chi-square test. Fisher's exact test was used when the expected cell counts were less than five. Receiver operating characteristic (ROC) curve analysis was used to compare the diagnostic performance of SRE cutoff values ≥ 2 and ≥ 4 for predicting malignant breast lesions. Sensitivity, specificity, positive likelihood ratio, negative likelihood ratio, positive predictive value (PPV), negative predictive value (NPV), and accuracy with 95% confidence intervals (CI) were calculated for each SRE cutoff value. A p value less than 0.05 was statistically significant. Statistical analyses were performed using RStudio (vs. 2025.09.1+401) (RStudio, Vienna, Austria) and SPSS vs. 2025 (IBM Corp., Armonk, NY, USA).

RESULTS

Three-grade classification by SRE and histopathologic diagnosis of breast lesions

Of 173 women with breast lesions, 73 (42.0%) had benign lesions and 100 (58.0%) malignant lesions (Table 1). The grade 1, soft pattern of SRE was more

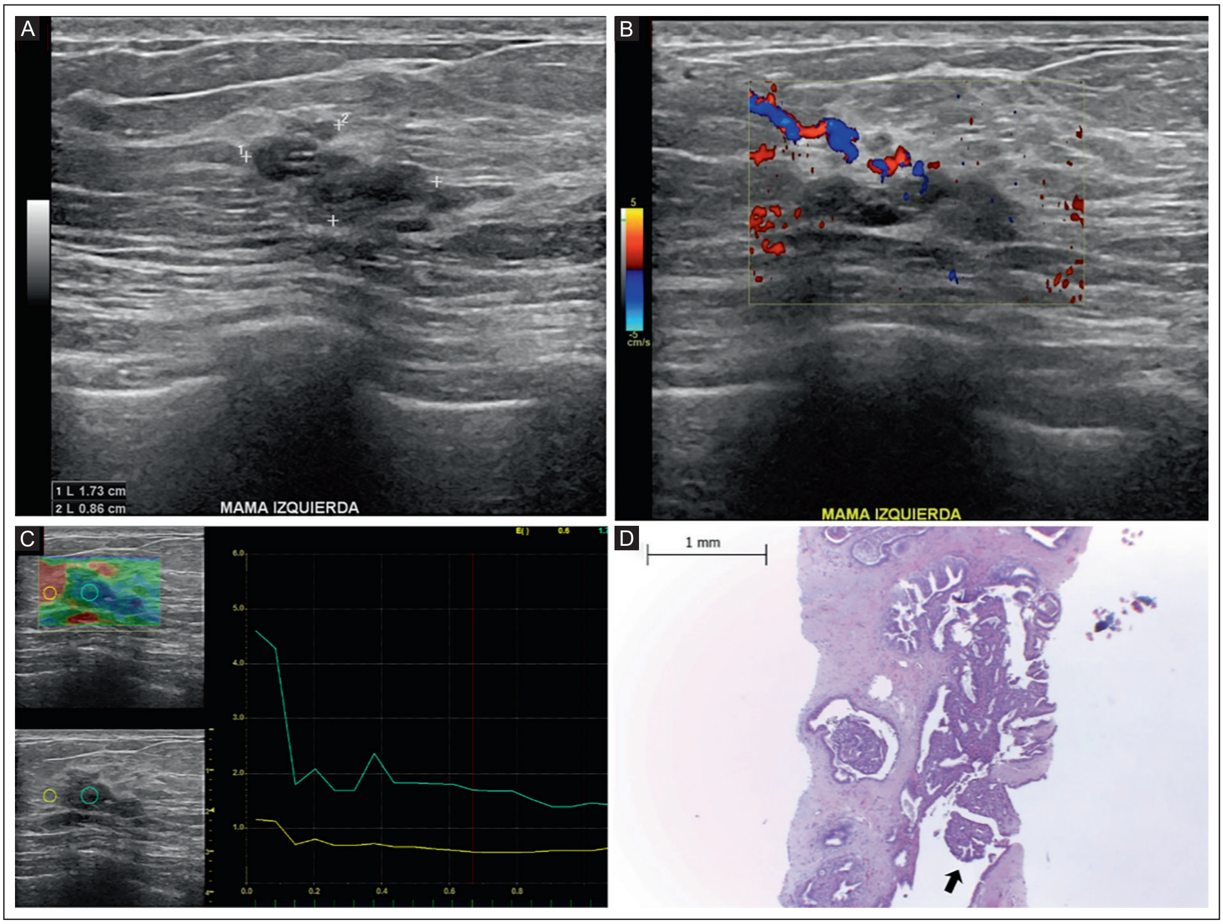

Figure 1. A 62-year-old woman with a palpable lump in the left breast. **A:** grayscale US shows a hypoechoic, focal, parallel, non-mass lesion located in the upper-inner quadrant of the left breast and measuring 1.7 × 0.9 cm with posterior shadowing and architectural distortion. **B:** color Doppler US shows peripheral vascularity. BI-RADS 4A. **C:** SE image shows the ROI at the center of the lesion (green circle and line) and the reference ROI in the adjacent fat tissue (yellow circle and line). The SRE cutoff value was 1.7 (grade 1, soft pattern). **D:** histological section (H&E, 20×) shows a papillary proliferation occupying the duct lumen. It consists of arborescent extensions emerging from a central fibrovascular stalk, lined by epithelium without atypia (black arrow). The diagnosis was intraductal papilloma of the breast.

US: ultrasound; BI-RADS: Breast Imaging Reporting and Data System; SE: strain elastography; ROI: region of interest; H&E: hematoxylin and eosin.

common in benign breast lesions (n = 31, 42.5%), followed by grade 2, intermediate pattern (n = 24, 32.9%), and grade 3, hard pattern (n = 18, 24.6%). In contrast, in malignant lesions, the most common SRE was grade 3, hard pattern (n = 71, 71.0%), followed by grade 2, intermediate pattern (n = 22, 22.0%), and grade 1, soft pattern (n = 7, 7.0%).

Figure 1 shows grayscale US, color Doppler, and SE images of a non-mass lesion, BI-RADS 4A. The SRE cutoff value was 1.7, soft pattern, and the histopathologic diagnosis was intraductal papilloma. Figure 2 shows grayscale US, color Doppler, and SE images of a mass, BI-RADS 4B. The SRE cutoff value was 3.9, intermediate pattern. The histopathologic diagnosis was fibroadenoma. Figure 3 shows grayscale US, color Doppler, and SE images of a mass, BI-RADS 4C. The SRE cutoff value was 5.0, hard pattern. The histopathologic diagnosis was fibroadenoma.

Comparison of a three-grade classification by SRE for the differentiation of benign and malignant breast lesions

The median SRE cutoff value in benign lesions was 2.4 (IQR 1.5-3.9), whereas in malignant lesions, it was 5.2 (IQR 3.7-5.9), with a significant difference ($p < 0.001$).

The diagnosis of benign breast lesions was significantly more common in grade 1, soft pattern (n = 31, 42.0%) compared to malignant breast lesions (n = 7, 7.0%) ($p < 0.001$) (Table 2). In contrast, the hard SRE pattern was significantly more common in malignant lesions (n = 71, 71.0%) compared to benign lesions

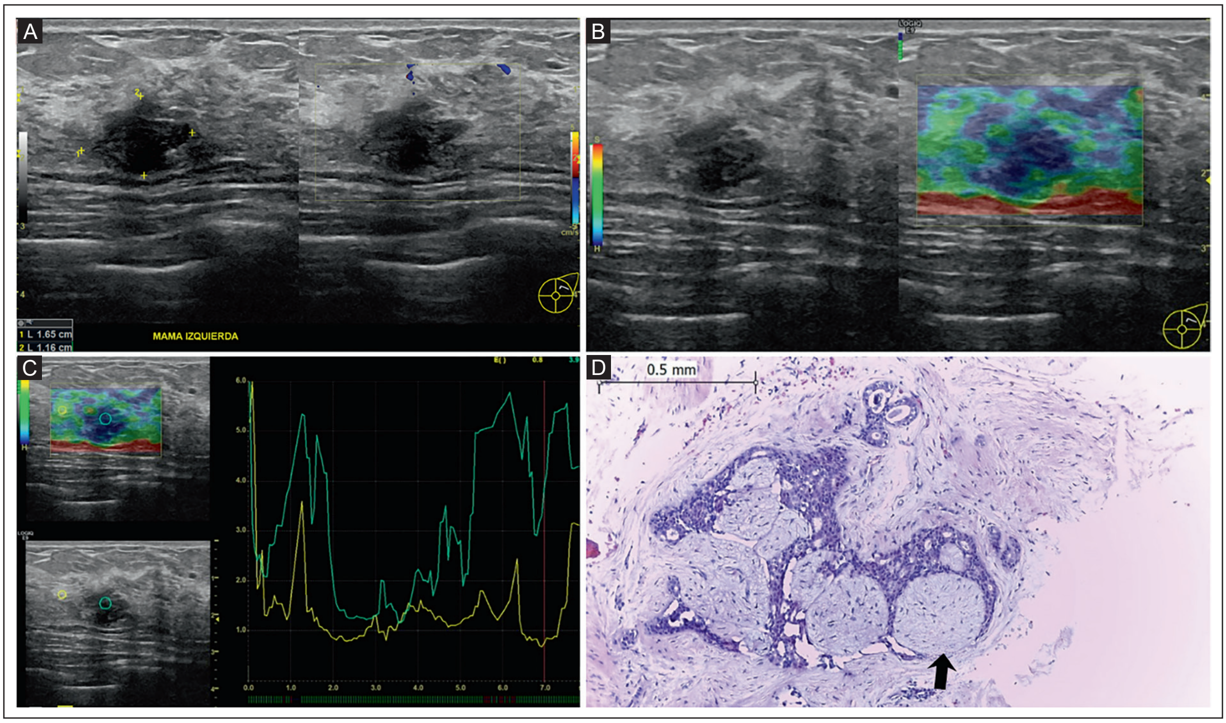

Figure 2. A 29-year-old woman with a palpable lump in the left breast. **A:** grayscale US shows an oval, hypoechoic, parallel mass with a microlobulated margin and posterior shadowing. Color Doppler US shows no vascularity. The mass is located in the upper outer quadrant of the left breast and measures 1.6 × 1.1 cm; BI-RADS 4B. **B-C:** SE image shows the ROI at the center of the lesion (green circle and line). The reference ROI is in the adjacent fat tissue (yellow circle and line). The SRE cutoff value was 3.9 (grade 2, intermediate pattern). **D:** histological section (H&E, 20×) shows a fibroepithelial lesion with spindle cells and collagen deposits displacing the epithelial component composed of columnar to cuboidal cells without cytological atypia (black arrow). The diagnosis was fibroadenoma of the breast.

US: ultrasound; BI-RADS: Breast Imaging Reporting and Data System; SE: strain elastography; ROI: region of interest; H&E: hematoxylin and eosin.

(n = 18, 25.0%) ($p < 0.001$). There was no significant difference between benign (n = 24, 33.0%) and malignant lesions (n = 22, 22.0%) ($p = 0.110$) in those with an intermediate pattern.

Diagnostic performance of SRE for predicting malignant breast lesions

The ROC curve for cutoff value ≥ 2, corresponding to grade 2 (intermediate pattern) by SRE for predicting malignant breast lesions showed a sensitivity of 93.0% (95% CI, 86.1-97.14), a specificity of 42.4% (95% CI, 30.9-54.5), and an accuracy of 71.6% (95% CI, 64.3-78.2) (Figure 4A, Table 3). There were 93 true positives, 42 false positives, 7 false negatives, and 31 true negatives.

The ROC curve for a hardness cutoff value ≥ 4, corresponding to grade 3 (hard pattern) by SRE for predicting malignant breast lesions showed a sensitivity of 71.0% (95% CI, 61.0-79.6), a specificity of 75.3% (95% CI, 63.8-84.6), and an accuracy of 72.8% (95% CI, 65.5-79.3) (Figure 4B, Table 4). The AUC was 0.80 (95% CI, 0.74-0.86). There were 71 true positives, 18 false positives, 29 false negatives, and 55 true negatives.

Three-grade classification by SRE in relation to the tumor grade of malignant breast lesions

Among malignant breast lesions (n = 100), hardness according to SRE was compared with histologic tumoral grade (Table 5). The hard pattern, SRE grade 3, was the most common in all tumoral grades. The most common cases were tumoral grade 2 (67/100, 67%).

Three-grade classification by SRE in relation to molecular subtypes of malignant breast lesions

The SRE hardness grade was also evaluated in relation to molecular subtype (Table 6). The grade 3 hard pattern was more common in all molecular subtypes, with no significant difference compared to the grade 1 soft pattern and the grade 2 intermediate pattern.

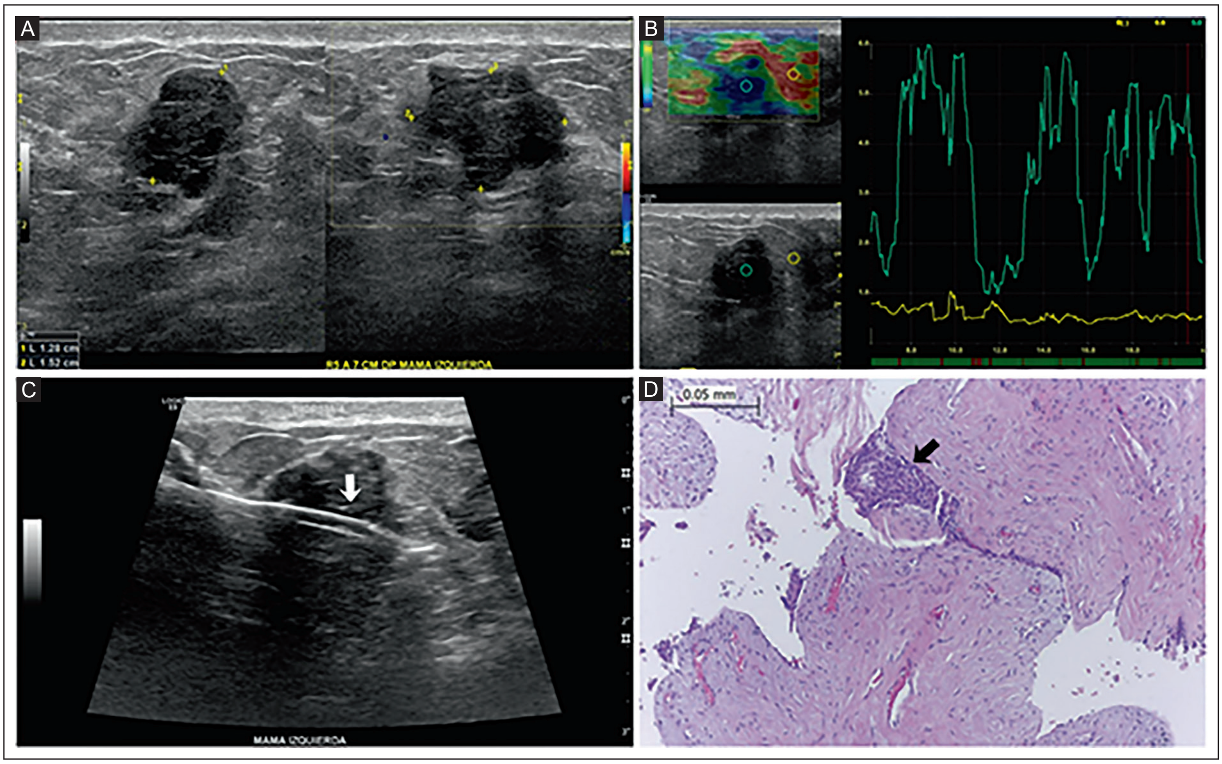

Figure 3. A 45-year-old woman with a palpable lump in the left breast. **A:** grayscale US shows an oval, hypoechoic, parallel mass with an angular margin and posterior shadowing. Color Doppler US shows no vascularity. The mass is located in the lower outer quadrant of the left breast and measures 1.2 × 1.5 cm; BI-RADS 4C. **B:** SE image shows an ROI at the center of the lesion (green circle and line). A reference ROI is in the adjacent fat tissue (yellow circle and line). The SRE cutoff value was 5.0 (grade 3, hard pattern). **C:** US-guided needle biopsy (white arrow). **D:** histological section (H&E, 20×) shows a benign fibroepithelial lesion with dense fibrous stroma, vascular congestion, and ductal hyperplasia without atypia (black arrow). The diagnosis was fibroadenoma of the breast.

US: ultrasound; BI-RADS: Breast Imaging Reporting and Data System; SE: strain elastography; ROI: region of interest; H&E: hematoxylin and eosin.

Table 2. Comparison of a three-grade classification[a] by SRE for the differentiation of benign and malignant breast lesions

Description	Benign breast diagnosis (n = 73)	Malignant breast diagnosis (n = 100)	p
Grade 1: soft pattern, n (%)	31 (42.0)	7 (7.0)	< 0.001
Grade 2: intermediate pattern, n (%)	24 (33.0)	22 (22.0)	0.110
Grade 3: hard pattern, n (%)	18 (25.0)	71 (71.0)	< 0.001

[a]Grade 1 with an SRE cutoff of 0 to 1.9; grade 2 with an SRE of 2.0 to 3.9; and grade 3 with an SRE of 4.0 to 6.
SRE: strain ratio elastography.

Figure 5 shows grayscale US, color Doppler, and SE images of a mass, BI-RADS 4C. The SRE cutoff value was 5.9, hard pattern. The histopathologic diagnosis was invasive ductal carcinoma, tumor grade 1, and molecular subtype luminal B. Figure 6 shows grayscale US, color Doppler, and SE images of a mass, BI-RADS 4B. The SRE cutoff value was 5.3, hard pattern. The histopathologic diagnosis was invasive ductal carcinoma, tumor grade 2, and molecular subtype HER2. Figure 7 shows grayscale US, color Doppler, and SE images of a mass, BI-RADS 4C. The SRE cutoff value was 5.7, hard pattern. The histopathologic diagnosis was invasive ductal carcinoma with a cribriform pattern, tumor grade 3, and molecular subtype luminal A.

DISCUSSION

We propose a three-grade classification of SRE cutoff values using the LOGIQ E9 GE system for predicting malignant breast lesions. The diagnostic performance of an SRE cutoff ≥ 4 (grade 3, hard pattern) was good for predicting malignant breast lesions BI-RADS

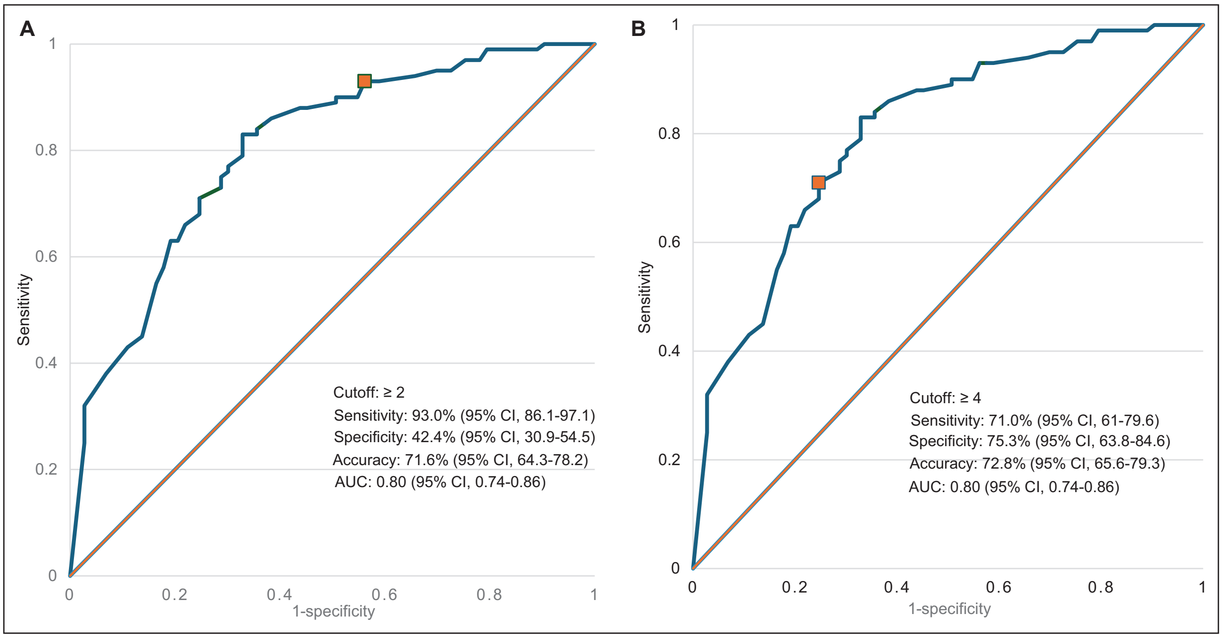

Figure 4. ROC curves of strain ratio elastography for predicting malignant breast lesions. **A:** ROC curve for the strain ratio elastography cutoff value ≥ 2, intermediate pattern, with a sensitivity of 93.0%, a specificity of 42.4%, and an accuracy of 71.6%. **B:** ROC curve for the strain ratio elastography cutoff value ≥ 4 with a sensitivity of 71.0%, a specificity of 75.3%, and an accuracy of 72.8%. The diagonal line represents the expected diagnostic performance by chance.

ROC: receiver operating characteristic; AUC: area under the curve; SE: strain elastography.

Table 3. Diagnostic performance of an SRE cutoff ≥ 2 (intermediate pattern) for predicting malignant breast lesions

Description	Parameter
Sensitivity, n (%) (95% CI)	93.0 (86.1-97.14)
Specificity, n (%) (95% CI)	42.4 (30.9-54.5)
Positive LR (min-max)	1.62 (1.32-1.98)
Negative LR (min-max)	0.16 (0.08-0.35)
PPV, n (%) (95% CI)	68.8 (64.3-73.0)
NPV, n (%) (95% CI)	81.5 (67.3-90.4)
Accuracy, n (%) (95% CI)	71.6 (64.3-78.2)

SRE: strain ratio elastography; LR: likelihood ratio; PPV: positive predictive value; NPV: negative predictive value; CI: confidence interval.

Table 4. Diagnostic performance of an SRE cutoff ≥ 4 (hard pattern) for predicting malignant breast lesions

Description	Parameter
Sensitivity, n (%) (95% CI)	71.0 (61.0-79.6)
Specificity, n (%) (95% CI)	75.3 (63.8-84.6)
Positive LR (min-max)	2.88 (1.89-4.38)
Negative LR (min-max)	0.38 (0.28-0.54)
PPV, n (%) (95% CI)	78.7 (72.1-85.7)
NPV, n (%) (95% CI)	65.4 (57.6-72.5)
Accuracy, n (%) (95% CI)	72.8 (65.5-79.3)

SRE: strain ratio elastography; LR: likelihood ratio; PPV: positive predictive value; NPV: negative predictive value; CI: confidence interval.

categories 4 or 5. These results applied only to the LOGIQ E9 GE system. The three-grade classification based on the SRE cutoff value may be useful for improving characterization of breast lesions as a complement to morphological BI-RADS assessment.

Elasticity has been categorized as soft, intermediate, or hard using a five-point scale for the color map and E/B index[1]. In contrast, SRE cutoff values that distinguish malignancy from benignity are not standardized[1]. Furthermore, each equipment brand defines its own reference values for reporting SRE. Radiologists should review the elastography recommendations of their US unit vendor[2-9]. In our study, using the LOGIQ E9 GE, we proposed a new grading classification based on SRE cutoff values: grade 1, soft pattern (0-1.9); grade 2, intermediate pattern (2.0-3.9); and grade 3, hard pattern (4.0-6.0). We found that grade 3 with an SRE cutoff ≥ 4 had good diagnostic performance, with a sensitivity of 71.0%, a specificity of 75.3%, and an accuracy of 72.8% for predicting malignant breast lesions.

Table 5. Three-grade classification by SRE in relation to the tumor grade of malignant breast lesions

Description	Total (n = 100)	SRE Grade 1 (soft pattern) (n = 7)	SRE Grade 2 (intermediate pattern) (n = 22)	SRE Grade 3 (hard pattern) (n = 71)	p
Tumor grade, n (%)					
Grade 1	20	3 (15.0)	8 (40.0)	9 (45.0)	0.015
Grade 2	67	2 (3.0)	11 (16.4)	54 (80.6)	0.006
Grade 3	13	2 (15.4)	3 (23.1)	8 (61.5)	0.428

[a] Grade 1 with an SRE cutoff of 0 to 1.9; grade 2 with an SRE of 2.0 to 3.9; and grade 3 with an SRE of 4.0 to 6. SRE: strain ratio elastography.

Table 6. Three-grade classification by SRE in relation to molecular subtypes of malignant breast lesions

Description	Total (n = 100)	SRE Grade 1 (soft pattern) (n = 7)	SRE Grade 2 (intermediate pattern) (n = 22)	SRE Grade 3 (hard pattern) (n = 71)	p
Molecular subtype, n (%)					
Luminal A	37	1 (2.7)	9 (24.3)	27 (73.0)	0.422
Luminal B	28	1 (3.5)	5 (17.9)	22 (78.6)	0.530
Her2	11	1 (9.0)	3 (27.3)	7 (63.7)	0.849
Her2-enriched	10	1 (10.0)	3 (30.0)	6 (60.0)	0.721
Triple negative	14	3 (21.4)	2 (14.3)	9 (64.3)	0.068

[a] Grade 1 with an SRE cutoff of 0 to 1.9; grade 2 with an SRE of 2.0 to 3.9; and grade 3 with an SRE of 4.0 to 6. Her2: human epidermal growth factor receptor 2. SRE: strain ratio elastography.

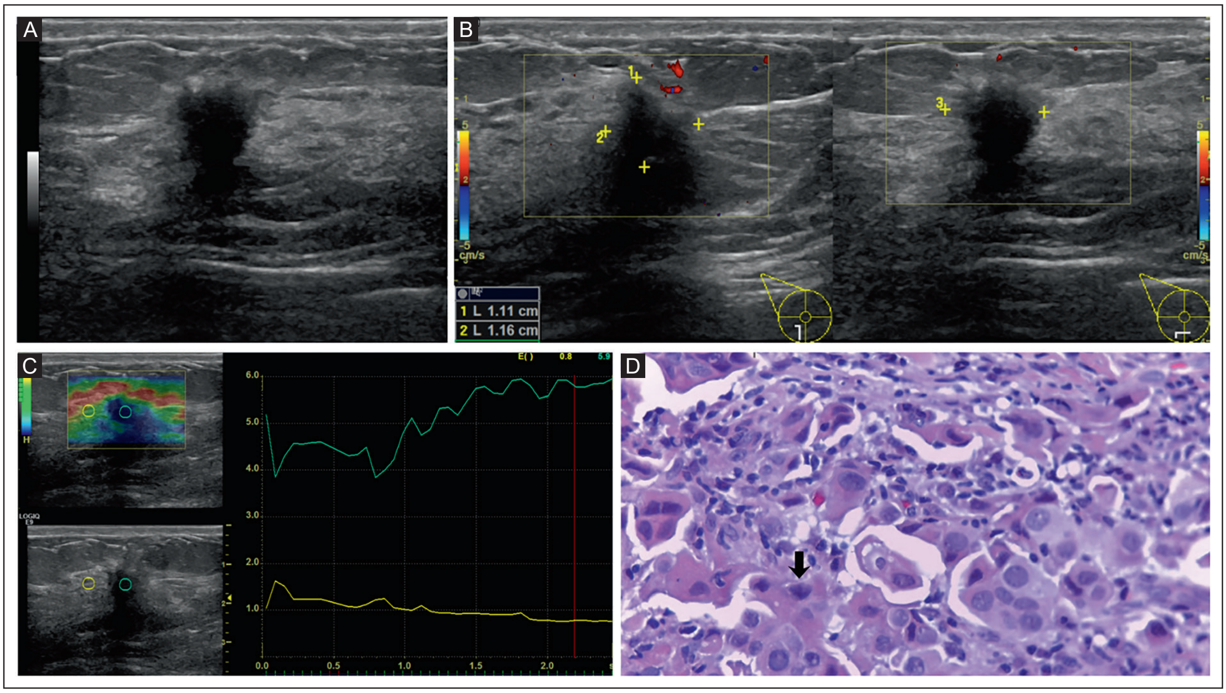

Figure 5. A 54-year-old woman with a palpable lump in the right breast. **A:** grayscale US shows an irregular, non-parallel, hypoechoic mass with an angular margin and posterior shadowing. **B:** color Doppler US shows no internal vascularity. The mass is located in the lower-outer quadrant of the right breast and measures 1.1 × 1.1 cm; BI-RADS 4C. **C:** SE image shows an ROI in the center of the lesion (green circle and line) and a reference ROI in the adjacent fat tissue (yellow circle and line). The SRE cutoff value was 5.9 (grade 3, hard pattern). **D:** histological section (H&E, 40×) shows nests of cells with abundant cytoplasm and nuclei with irregular chromatin, pleomorphism, and hyperchromatic nuclei (black arrow). The diagnosis was invasive ductal carcinoma, tumor grade 1, and molecular subtype luminal B.

US: ultrasound; BI-RADS: Breast Imaging Reporting and Data System; SE: strain elastography; ROI: region of interest; H&E: hematoxylin and eosin.

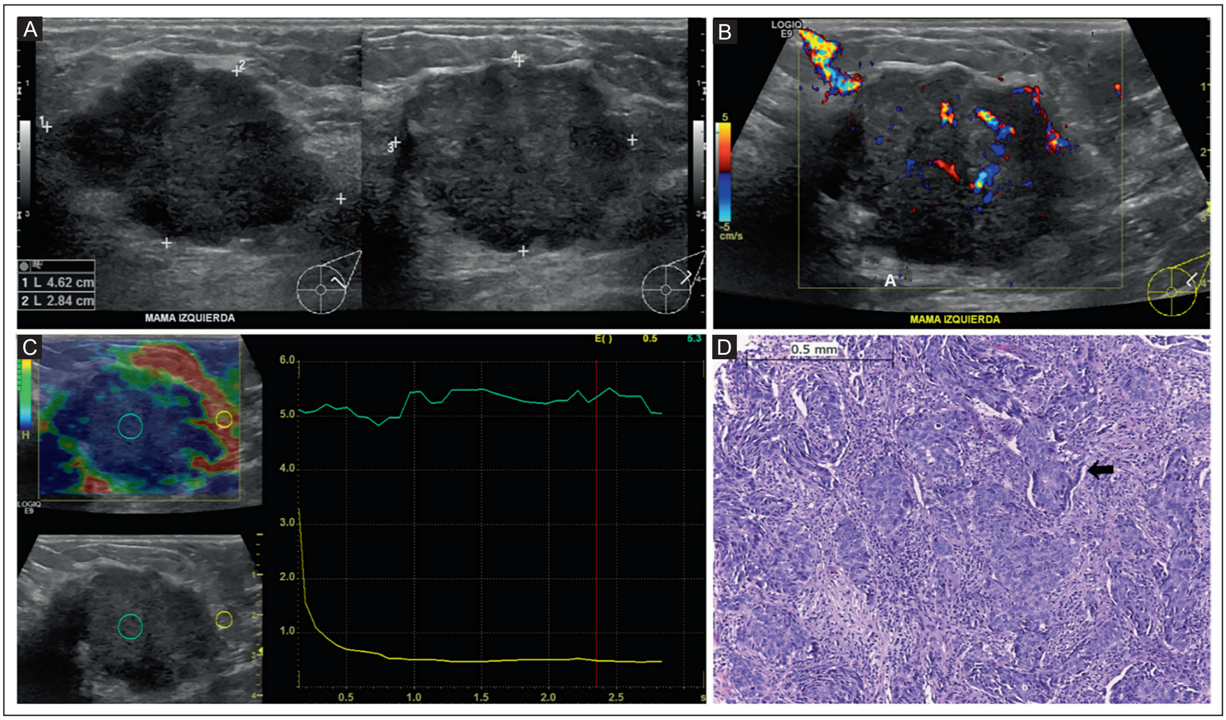

Figure 6. A 39-year-old woman with a palpable lump in the left breast. **A:** grayscale US shows an oval, parallel-oriented, hypoechoic mass with a microlobulated margin and posterior enhancement, located in the upper-outer quadrant of the left breast and measuring 4.6 × 2.8 cm. **B:** color Doppler US shows internal vascularity. BI-RADS 4B. **C:** SE shows an ROI at the center of the lesion (green circle and line) with the reference ROI in adjacent fat tissue (yellow circle and line). The SRE cutoff value was 5.3 (grade 3, hard pattern). **D:** histological section (H&E, 20×) shows solid nests of pleomorphic and atypical cells, inducing extensive peripheral desmoplastic reaction in the stroma (black arrow). The diagnosis was invasive ductal carcinoma, tumor grade 2, and molecular subtype HER2.

US: ultrasound; BI-RADS: Breast Imaging Reporting and Data System; SE: strain elastography; ROI: region of interest; H&E: hematoxylin and eosin.

In contrast, an SRE cutoff ≥ 2 at grade 2 (intermediate pattern) yielded a sensitivity of 93%, a specificity of 42.4%, and an accuracy of 71.6% for predicting malignancy. The SRE cutoff ≥ 4 showed higher specificity and fewer false positives ($n = 29$) than the cutoff ≥ 2 ($n = 42$). Liu et al.[2] evaluated 431 BI-RADS 4 breast lesions in 417 women. All patients were examined with US, SE, and histopathology using the LOGIQ E9 GE system. There were 276 malignant and 155 benign lesions. An SRE cutoff of 4.15 yielded a sensitivity of 92.2%, a specificity of 72.5%, and an accuracy of 86.1%. Mutala et al.[4] studied 112 patients using US and SE with a LOGIQ E9 GE system and histopathologic examination, BI-RADS 4 and 5 categories. Eighty-four lesions were benign, and 28 were malignant. An SRE cutoff of 4.2 yielded a sensitivity of 93% and a specificity of 96%. Our study results are comparable to those of the Mutala and Liu reports, both of which used LOGIQ E9 GE equipment and recommended an SRE cutoff ≥ 4.

Soft breast lesions assessed by SE tend to be benign, with exceptions such as mucinous carcinoma, ductal carcinoma *in situ*, and necrotic tumors[1]. The SRE cutoff for benign lesions has been little studied. Kokubu et al.[3], using the LOGIQ E9 GE system, evaluated 170 patients with intraductal breast lesions and reported a mean SRE cutoff of 2.63 ± 1.22 for benign lesions and 4.46 ± 1.08 for malignant lesions ($p < 0.001$). In our study of 173 women, 73 with benign and 100 with malignant breast lesions, the median SRE cutoff was 2.4 (IQR 1.5-3.9) for benign lesions and 5.2 (IQR 3.7-5.9) for malignant lesions ($p < 0.001$). This finding enables significant differentiation between benign and malignant lesions. Benign lesions were commonly classified as SRE grade 1, soft pattern ($n = 31$, 42.0%) and SRE grade 2, intermediate pattern ($n = 24$, 33.0%). In contrast, malignant lesions were commonly SRE grade 3, hard pattern ($n = 71$, 71.0%). Our results for benign lesions are comparable to other reports, indicating that benign breast lesions are softer than malignant ones.

The strengths of this study include the use of histopathologic confirmation as the gold standard for breast lesion diagnoses. Only SE images with optimal compression, as determined by the quality index, were included. SE examinations were performed by a

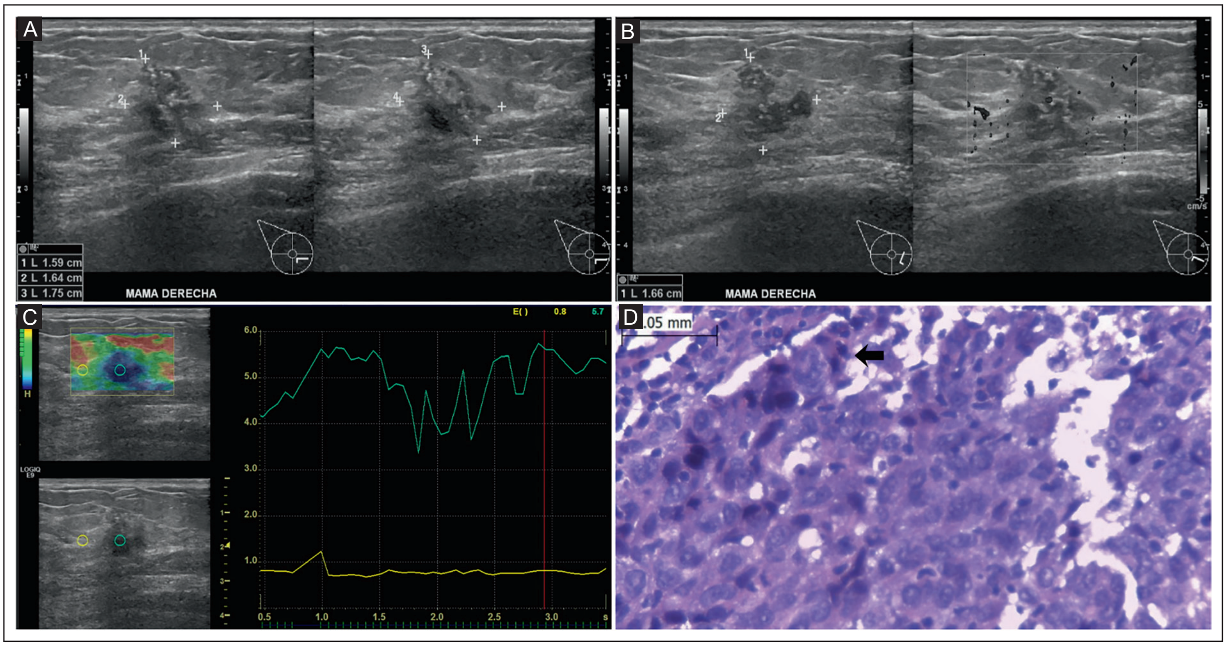

Figure 7. A 59-year-old asymptomatic woman, mammography screening (not shown) with focal asymmetry of the right breast. **A:** a grayscale US shows an irregular, parallel, hypoechoic mass, with an angular margin, posterior shadowing, and calcifications, located in the lower inner quadrant of the right breast and measuring 1.5 × 1.6 cm, BI-RADS 4C. **B:** color Doppler US shows internal vascularity. **C:** SE shows the ROI at the center of the lesion (green circle and line), with the reference ROI in adjacent fat tissue (yellow circle and line). The SRE cutoff value was 5.7 (grade 3, hard pattern). **D:** histological section (H&E, 40×) shows marked atypia, nuclear pleomorphism, and atypical mitoses (black arrow). The diagnosis was invasive ductal carcinoma with a cribriform pattern, tumor grade 3, and molecular subtype luminal A.

US: ultrasound; BI-RADS: Breast Imaging Reporting and Data System; SE: strain elastography; ROI: region of interest; H&E: hematoxylin and eosin.

radiologist specializing in breast imaging. Our study has several limitations, including its retrospective, single-center design. Only patients with suspicious BI-RADS categories 4 and 5 were included. The placement of the ROI and the maintenance of steady compression are operator dependent, and image quality significantly impacts the accuracy of interpretation[1]. The cutoff value of SRE for predicting malignant breast lesions was selected arbitrarily and guided the SRE three-grade classification. In addition, intra- and interobserver agreement were not assessed, which limits the evaluation of the reproducibility of SRE measurements. Our study assessed only the LOGIQ E9 GE system; therefore, our results are not generalizable to other US systems from other manufacturers due to vendor-dependent differences in SRE implementation and semiquantitative scales.

CONCLUSION

This study presented a three-grade classification based on SRE cutoff values using the LOGIQ E9 GE. The SRE grade 3, hard pattern with a cutoff value ≥ 4 had good diagnostic performance for predicting malignant breast lesions. Future studies should validate our results using larger sample sizes in multicenter settings. As elastography techniques continue to evolve, radiologists and US vendors should agree upon a universally standard SRE cutoff value to promote consistency in predicting benign and malignant breast lesions.

Acknowledgments

The authors thank Professor Ana M. Contreras-Navarro for her guidance in preparing and writing this scientific paper.

Funding

The authors declare that they have not received funding.

Conflicts of interest

The authors declare no conflicts of interest.

Ethical considerations

Protection of human subjects and animals. The authors declare that the procedures followed were in accordance with the ethical standards of the responsible committee on human experimentation and with the World Medical Association and the Declaration of Helsinki (1964). The procedures were authorized by the Institutional Ethics Committee.

Confidentiality, informed consent, and ethical approval. The authors have followed their institution's confidentiality protocols, informed consent was not required, and secured approval from the Ethics Committee. SAGER guidelines have been followed as applicable to the nature of the study.

Declaration on the use of artificial intelligence. The authors declare that no generative artificial intelligence was used in the writing or creation of the content of this manuscript.

REFERENCES

1. Leung JWT, Baker JA, Hooley R, Loving VA, Raelyea JA. Ultrasound. In: ACR BI-RADS v2025 Manual. Reston, VA. USA. American College of Radiology; 2025.
2. Liu XJ, Zhu Y, Liu PF, Xu YL. Elastography for breast cancer diagnosis: a useful tool for small BI-RADS 4 lesions. Asian Pac J Cancer Prev. 2014;15(24):10739-10743. doi: 10.7314/apjcp.2014.15.24.10739.
3. Kokubu Y, Yamada K, Tanabe M, Izumori A, Kato C, Horii R, et al. Evaluating the usefulness of breast strain elastography for intraductal lesions. J Med Ultrason. 2021;48(1):63-70. doi: 10.1007/s10396-020-01070-2.
4. Mutala TM, Ndaiga P, Aywak A. Comparison of qualitative and semiquantitative strain elastography in breast lesions for diagnostic accuracy. Cancer Imaging. 2016;16(1):12. doi: 10.1186/s40644-016-0070-8.
5. Zhi H, Xiao XY, Yang HY, Ou B, Wen YL, Luo BM. Ultrasonic elastography in breast cancer diagnosis: strain ratio vs 5-point scale. Acad Radiol. 2010;17(10):1227-1233. doi: 10.1016/j.acra.2010.05.004.
6. Cruz-Ramos JA, Trapero-Corona MI, Valencia-Hernández IA, Gómez-Vargas LA, Toranzo-Delgado MT, Cano-Magaña KR, et al. Strain elastography fat-to-lesion index is associated with mammography BI-RADS grading, biopsy, and molecular phenotype in breast cancer. Biosensors (Basel). 2024;14(2):94. doi: 10.3390/bios14020094.
7. Itoh A, Ueno E, Tohno E, Kamma H, Takahashi H, Shiina T, et al. Breast disease: clinical application of US elastography for diagnosis. Radiology. 2006;239(2):341-350. doi: 10.1148/radiol.2391041676.
8. Kanagaraju V, Dhivya B, Devanand B, Maheswaran V. Utility of ultrasound strain elastography to differentiate benign from malignant lesions of the breast. J Med Ultrasound. 2020;29(2):89-93. doi: 10.4103/JMU.JMU_32_20.
9. Mutala TM, Mwango GN, Aywak A, Cioni D, Neri E. Determining the elastography strain ratio cut off value for differentiating benign from malignant breast lesions: systematic review and meta-analysis. Cancer Imaging. 2022;22(1):12. doi: 10.1186/s40644-022-00447-5.
10. Tay IWM, Sim LS, Moey THL, Tan KPP, Lai LMS, Leong LCH. Shear wave versus strain elastography of breast lesions-The value of incorporating boundary tissue assessment. Clin Imaging. 2022;82:228-233. doi: 10.1016/j.clinimag.2021.11.030.
11. Gu Y, Tian J, Ran H, Ren W, Chang C, Yuan J, et al. Ultrasound strain elastography to improve diagnostic performance of breast lesions by reclassifying BI-RADS 3 and 4a lesions: a multicentre diagnostic study. Br J Radiol. 2025;98(1165):89-99. doi: 10.1093/bjr/tqae197.
12. Mendelson EB, Bühm-Vélez M, Berg WA, Whitman GJ, Feldman MI, Madjar H, et al. ACR BI-RADS ultrasound. In: ACR BI-RADS Atlas: Breast imaging reporting and data system. Reston, VA. USA. American College of Radiology; 2013.
13. General Electric Healthcare. LOGIQ E9 basic user manual. Milwaukee (WI): General Electric Co.; 2014. 1598p. Direction 5496408-100. English Rev. 1, version R5.
14. Yang WT, Bu H. Updates in the 5(th) edition of WHO classification of tumours of the breast. Zhonghua Bing Li Xue Za Zhi. 2020;49(5):400-405. Chinese. doi: 10.3760/cma.j.cn112151-20200303-00163.
15. Elston CW, Ellis IO. Pathological prognostic factors in breast cancer. I. The value of histological grade in breast cancer: experience from a large study with long-term follow-up. Histopathology. 1991;19(5):403-410. doi: 10.1111/j.1365-2559.1991.tb00229.x.
16. Untch M, Gerber B, Harbeck N, Jackisch C, Marschner N, Möbus V, et al. 13th st. Gallen international breast cancer conference 2013: primary therapy of early breast cancer evidence, controversies, consensus - opinion of a German team of experts (Zurich 2013). Breast Care (Basel). 2013;8(3):221-229. doi: 10.1159/000351692.

JMeXFRI

Journal of the Mexican Federation of Radiology and Imaging

FULL RESEARCH ARTICLE

Fractional anisotropy quantification by diffusion tensor MRI of cranial nerves VII and VIII with neurovascular contact in patients with and without neurocompressive syndrome

M. Pilar Cortes-Avalos, C. Arturo Dominguez-Frausto and Juan A. Benitez-Lopez*

Magnetic Resonance Imaging Unit, Institute of Neurobiology, Universidad Nacional Autonoma de Mexico, Juriquilla, Queretaro, Mexico

ABSTRACT

Introduction: *Fractional anisotropy (FA) quantification using diffusion tensor imaging (DTI) provides information beyond anatomy. It allows differentiation between incidental asymptomatic neurovascular contact (NVC) and clinical neurocompressive syndrome. This study evaluated the FA of cranial nerves VII and VIII with NVC at the cerebellopontine angle in patients with and without neurocompressive syndrome.* **Material and Methods***: This cross-sectional study evaluated participants with and without neurocompressive syndromes, including hemifacial spasm, tinnitus, or vertigo. Conventional 3.0T magnetic resonance imaging (MRI) with T2-weighted CUBE and 3D- time-of -flight (TOF) sequences was performed. FA quantification using DTI MRI, as well as Chavda type and Gorrie grading were used to assess NVC.* **Results.** *We evaluated 132 ears in 66 adults; 99 (75.0%) had some type of NVC. Among these, 66 ears were asymptomatic with a high mean FA (0.294 ± 0.068). Thirty-three ears with neurocompressive syndrome had a low mean FA (0.218 ± 0.053) ($p < 0.001$). In ears with NVC, the mean FA was 0.207± 0.032 in hemifacial spasm (n = 6, 6.1%), 0.227 in tinnitus (n = 21, 21.2%), and 0.206 in vertigo (n = 14, 14.2%). In contrast, the mean FA was 0.273 in ears without hemifacial spasm (n = 93, 93.9%), 0.280 in those without tinnitus (n = 78, 78.8%), and 0.279 in those without vertigo (n = 85, 85.8%). FA differences were significant between ears with and without neurocompressive syndrome.* **Conclusion.** *DTI MRI demonstrated significantly lower FA of cranial nerves VII and VIII with NVC at the cerebellopontine angle in ears with neurocompressive syndrome compared to asymptomatic ears with NVC.*

Keywords: *Diffusion tensor. Fractional anisotropy. Neurovascular contact. Neurocompression syndrome. Facial nerve. Vestibulocochlear nerve.*

INTRODUCTION

The anatomical proximity of nerves and vessels in the cerebellopontine angle allows neurovascular contact (NVC) involving cranial nerves VII (facial) and VIII (vestibulocochlear), and cerebellar artery branches. NVC may be an incidental finding or associated with neurocompressive syndromes such as hemifacial spasm, vestibular neuralgia, or vascular hearing loss and vertigo[1,2]. Conventional magnetic resonance imaging (MRI) can identify the anatomical relationship between nerves and vessels, but it is limited in assessing neural microstructural damage. In this context, diffusion tensor imaging (DTI), particularly fractional anisotropy (FA), is an emerging quantitative tool that detects subtle changes in nerve fiber integrity[3].

FA quantification by DTI has been linked to white matter fiber demyelination[4]. NVC occurs most frequently at the root entry/exit zone, where the transition between central and peripheral myelin makes the nerve more

***Corresponding author:**
C. Arturo Dominguez-Frausto
E-mail: dominguez@inb.unam.mx

Received for publication: 18-10-2025
Accepted for publication: 17-12-2025
DOI: 10.24875/JMEXFRI.M26000124

Available online: 16-04-2026
J Mex Fed Radiol Imaging. 2026;5(1):36-45
www.JMeXFRI.com

vulnerable to pulsatile vascular compression. Not all cases of NVCs are clinically symptomatic. Therefore, a distinction is made between NVC with neurocompressive syndrome (vascular contact associated with neurological symptoms and, potentially, microstructural alterations of the nerve) and NVC without neurocompressive syndrome, which is an anatomical finding without a clinical correlation.

The role of DTI in NVC has been studied in trigeminal neuralgia; however, there are few reports on clinical symptoms involving cranial nerves VII and VIII at the cerebellopontine angle and the presence of neurocompressive syndromes such as hemifacial spasm, tinnitus, or vertigo[5,6]. This study used DTI to evaluate FA of cranial nerves VII and VIII in patients with NVC at the cerebellopontine angle, with and without neurocompressive syndrome.

MATERIAL AND METHODS

A cross-sectional study was conducted from July to October 2024 at the Magnetic Resonance Imaging Unit of the Institute of Neurobiology, Universidad Nacional Autonoma de Mexico, Juriquilla, Queretaro, Mexico. Participants of both sexes, over 18 years of age, referred with neurocompressive syndrome or other diagnoses without neurocompressive syndrome were included. Patients with an MRI showing a space-occupying lesion in the cerebellopontine angle or with a poor-quality MRI were excluded. Written informed consent was obtained. This study was approved by the Institutional Ethics Committee and Research Committee.

Development and study of variables

The age and sex of each participant were recorded in the institutional database. MRI T2-weighted CUBE and 3D-time-of-flight (TOF) sequences were used to assess the type and grade of NVC. FA was quantified using DTI in the axial plane.

Definitions

NVC: a vascular loop that contacts a cranial nerve, with no cerebrospinal fluid interface between them[7].

Neurocompressive syndrome: signs and symptoms such as hemifacial spasm, tinnitus and vertigo caused by irritation of cranial nerves VII or VIII due to direct mechanical contact with a vascular loop.

Vertigo: sensation of rotational movement, a vestibular dysfunction symptom.

Tinnitus: the perception of sound generated by body functions[8].

Hemifacial spasm: irregular, involuntary muscle contractions of the face[5].

FA: a scalar parameter that varies between 0 and 1; 0 refers to isotropy, and 1 refers to anisotropy. An FA close to 1 indicates highly directional diffusion, typical of intact and well-myelinated nerve fibers. An FA close to 0 indicates isotropic diffusion, associated with a loss of microstructural organization, demyelination, edema, or axonal degeneration.

Chavda classification of NVC

The Chavda classification was used to evaluate NVC. It refers to the depth of extension of the vascular loop in the cerebellopontine angle and internal auditory canal[9]. The NVC type was defined in the MRI T2-weighted CUBE and 3D-TOF sequences[9].

Chavda type I: an anterior inferior cerebellar artery loop within the cerebellopontine angle but outside the internal auditory canal.

Chavda type II: an anterior inferior cerebellar artery loop extending into the internal auditory canal, but less than 50% of the length of the internal auditory canal.

Chavda type III: an anterior inferior cerebellar artery loop with a greater than 50% extension into the internal auditory canal.

Gorrie grading of NVC

The Gorrie classification was used to define the grade of contact between the artery and nerve[10]. The NVC grades were determined using MRI T2-weighted CUBE and 3D-TOF anatomical sequences.

Gorrie grade A: an anterior inferior cerebellar artery loop without contact with the adjacent VII/VIII nerve complex.

Gorrie grade B: an anterior inferior cerebellar artery loop that runs adjacent to the VII/VIII nerve complex.

Gorrie grade C: an anterior inferior cerebellar artery loop that courses between the VII/VIII nerve complex.

Gorrie grade D: an anterior inferior cerebellar artery loop that physically displaces the VIII cranial nerve.

MRI acquisition and analysis protocol

A Discovery MR 750 3.0T scanner (2009, GE Healthcare, Milwaukee, WI, USA) with a 32-channel head coil was used. Conventional MRI T2 CUBE and 3D-TOF sequences were acquired in the axial plane.

DTI was performed with a b-value of 1000 and 27 directions, a field of view (FOV) of 24 × 24 mm, a matrix size of 120 × 120 mm × 1 number of signal averages (NSA), a slice thickness of 1 mm × 1 mm with no gaps, a time echo (TE) of 600 ms, and a time repetition (TR) of 68.5 ms.

The FA map was generated using GE post-processing and SIGNA_LX1.MR30.1_R01_2322.c software merged with the anatomical sequences. A region of interest (ROI) was manually defined at the NVC site and another of the same size at the same level in the contralateral ear. The assessment of NVC and FA was performed by a high-specialty resident in MRI (PCA) with 3 years of experience, supervised by a neuroradiologist (ADF) with 15 years of experience.

Statistical analysis

Numerical variables were described using measures of central tendency and dispersion, and categorical variables were described using absolute numbers and percentages. The mean and standard deviation (SD) of FA were reported. The association between unrelated categorical variables was assessed using the chi-square test. The difference between numerical variables divided into categorical groups was assessed using an independent-samples *t*-test. A p value less than 0.05 was considered significant. SPSS software v.25 (IBM Corp., Armonk, NY, USA) was used.

RESULTS

A total of 132 ears in 66 adults were evaluated with conventional MRI and DTI. Of the 66 patients, 41 (62.0%) were women and 25 (38.0%) were men. The mean age was 55.5 ± 17.9 with a range of 18 to 91 years.

FA quantification of cranial nerves VII and VIII with NVC comparing ears with and without neurocompressive syndrome

Of the 132 ears, 99 (75.0%) had some type of NVC at the cerebellopontine angle. Among these, 66 were asymptomatic with a high mean FA (0.294 ± 0.068) compared to a low mean FA (0.218 ± 0.053) (p < 0.001) in 33 ears with neurocompressive syndrome (Table 1). The mean FA was 0.207± 0.032 in hemifacial spasm (n = 6, 6.1%), 0.227 in tinnitus (n = 21, 21.2%), and 0.206 in vertigo (n = 14, 14.2%) in contacted ears (Table 2). In contrast, in ears without hemifacial spasm (n = 93, 93.9%), the mean FA was 0.273; without tinnitus, 0.280 (n = 78, 78.8%), and 0.279 without vertigo (n = 85, 85.8%). FA differences between ears with and without neurocompressive syndrome were significant. FA values were significantly lower in neurocompressive syndrome.

Table 1. FA quantification by DTI MRI of cranial nerves VII and VIII with NVC at the cerebellopontine angle with and without neurocompressive syndrome

Description		FA		
	(n = 99)	Mean	SD	p
With neurocompressive syndrome	33	0.218	0.053	< 0.001
Without neurocompressive syndrome	66	0.294	0.068	

FA: fractional anisotropy; DTI: diffusion tensor imaging; MRI: magnetic resonance imaging; NVC: neurovascular contact; SD: standard deviation.

Table 2. FA quantification by DTI MRI of cranial nerves VII and VIII with NVC at the cerebellopontine angle with neurocompressive syndrome

Description[a]		FA		
	n	Mean	SD	p
Hemifacial spasm				
Yes	6	0.207	0.032	0.002
No	93	0.273	0.073	
Tinnitus				
Yes	21	0.227	0.029	0.001
No	78	0.280	0.077	
Vertigo				
Yes	14	0.206	0.072	0.001
No	85	0.279	0.068	

[a] Eight ears had two or more symptoms.

FA: fractional anisotropy; DTI: diffusion tensor imaging; MRI: magnetic resonance imaging; NVC: neurovascular contact; SD: standard deviation.

Chavda classification of NVC and FA quantified by DTI MRI in cranial nerves VII and VIII, comparing ears with and without neurocompressive syndrome

Among 99 ears with some type of NVC at the cerebellopontine angle, 73 (73.7%) were Chavda type I, 23 (23.3%) type II, and 3 (3.0%) type III (Table 3). The mean FA of Chavda type I was 0.205 in ears with hemifacial spasm and 0.270 in those without it (p = 0.074). Tinnitus was present in 17 ears with a mean FA of 0.221. In contrast, in patients without tinnitus, the mean FA was 0.279 (p = 0.001).

Table 3. Chavda types of NVC and FA quantified by DTI MRI in cranial nerves VII and VIII comparing ears with and without neurocompressive syndrome

Description		Chavda type I FA				Chavda type II FA				Chavda type III FA		
	(n = 73)	Mean	SD	p	(n = 23)	Mean	SD	p	(n = 3)	Mean	SD	p
With neurocompressive syndrome	28	0.213	0.054	0.001	4	0.250	0.038	0.290	1	0.214	0.034	0.179
Without neurocompressive syndrome	45	0.298	0.073		19	0.283	0.058		2	0.304	0.021	
Neurocompressive syndrome[a]												
Hemifacial spasm												
Yes	5	0.205	0.035	0.074	0	-	-	-	1	0.214	0.034	0.179
No	68	0.270	0.078		23	0.278	0.055		2	0.304	0.021	
Tinnitus												
Yes	17	0.221	0.025	0.001	4	0.250	0.038	0.290	0	-	-	-
No	56	0.279	0.083		19	0.283	0.058		3	0.274	0.254	
Vertigo												
Yes	14	0.205	0.072	0.001	0	-	-	-	0	-	-	-
No	59	0.280	0.073		23	0.278	0.055		3	0.274	0.054	

[a]Eight ears had two or more symptoms.

FA: fractional anisotropy; DTI: diffusion tensor imaging; MRI: magnetic resonance imaging; NVC: neurovascular contact; SD: standard deviation.

Vertigo was present in 14 ears with a mean FA of 0.205, while in those without vertigo, the mean FA was 0.280 (p = 0.001).

In Chavda type II, tinnitus was present in four ears with a mean FA of 0.250, compared to 0.283 in those without tinnitus (p = 0.290). In Chavda type III, hemifacial spasm was present with an FA of 0.214, compared to a mean FA of 0.304 in those without hemifacial spasm (n = 2). There were no Chavda type II in ears with vertigo or hemifacial spasm or Chavda type III in those with tinnitus or vertigo.

Figure 1 shows MRI T2-weighted CUBE with examples of Chavda types of NVC based on vascular loop extension into the internal auditory canal. Figure 2 shows an MRI of a 61-year-old man with tinnitus and Chavda type II. DTI T2 CUBE fusion shows a decreased FA of 0.251 in the ROI at the level of an NVC. The contralateral ear shows an FA of 0.419.

Gorrie grades of NVC and FA quantified by DTI MRI in cranial nerves VII and VIII, comparing ears with and without neurocompressive syndrome

Among 99 ears with some grade of NVC at the cerebellopontine angle, three (3.0%) were Gorrie A, 79 (79.8%) Gorrie B, and 17 (17.2%) Gorrie C (Table 4). Gorrie grade B was the most common (n = 79, 79.8%). Of these, 53 (67.1%) were asymptomatic with a mean FA of 0.296, while 26 (32.9%) ears with neurocompressive syndrome exhibited a significantly lower mean FA of 0.211 (p = 0.001). In Gorrie grade B, the mean FA was 0.208 in those with hemifacial spasm and 0.272 in those without (p = 0.065). Tinnitus was present in 16 ears with a mean FA of 0.227, in contrast to a mean FA of 0.278 in those without tinnitus (p = 0.001). Vertigo was found in 11 with a mean FA of 0.189, while the mean FA was 0.280 in those without vertigo (p = 0.001).

Ears with Gorrie grade A showed an FA of 0.201 in one ear with hemifacial spasm compared to a mean FA of 0.273 in those without hemifacial spasm. Similarly, one ear with tinnitus had an FA of 0.201. Those without tinnitus had a mean FA of 0.273. Vertigo was found in one ear with an FA of 0.222, compared to a mean FA of 0.262 in those without vertigo.

Among those with Gorrie grade C, tinnitus was present in four ears with a mean FA of 0.232, compared to a mean FA of 0.291 in those without tinnitus. Vertigo was found in two ears with a mean FA of 0.288, while those without vertigo had a mean of 0.275. However, differences in mean FA values between NVC Gorrie grades A and B with and without neurocompressive syndrome were not significant. There was no patient with Gorrie D.

Figure 3 shows an MRI T2- weighted CUBE with the Gorrie grading of NVC between the vascular loop and the VIII nerve. Figure 4 shows an MRI of a 51-year-old

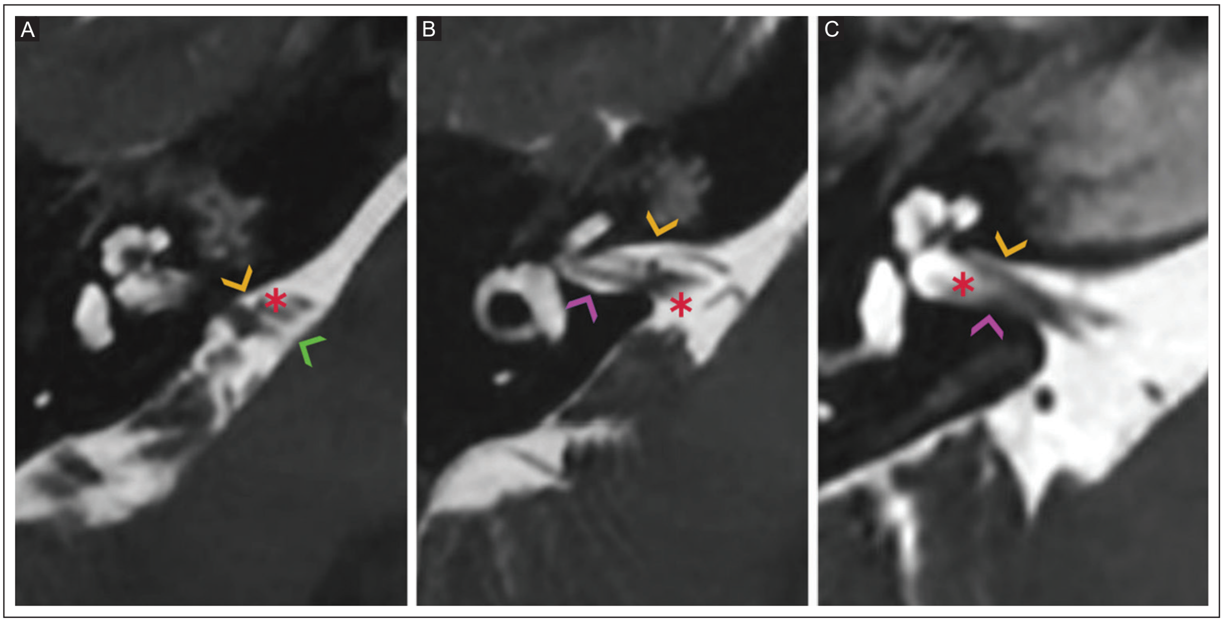

Figure 1. A 3.0T MRI T2- weighted CUBE shows Chavda types of NVC based on the depth of vascular loop extension into the internal auditory canal. **A:** a 66-year-old man with tinnitus and vertigo. NVC Chavda type I (yellow arrowhead) shows an anteroinferior cerebellar artery loop (asterisk) in the cerebellopontine angle (green arrowhead). **B:** a 61-year-old woman with hemifacial spasm. NVC Chavda type II (yellow arrowhead) shows an anteroinferior cerebellar artery loop (asterisk) extending into the internal auditory canal (purple arrowhead), but less than 50% of its length. **C:** a 54-year-old man with hemifacial spasm. The yellow arrowhead shows NVC Chavda type III with an anteroinferior cerebellar artery loop (asterisk) extending more than 50% into the internal auditory canal (purple arrowhead).

T: Tesla; MRI: magnetic resonance imaging; NVC: neurovascular contact.

man with tinnitus and vertigo, Chavda type I, Gorrie grade C. DTI T2-weighted CUBE fusion shows decreased FA (0.217) in the ROI at the level of the NVC. The contralateral ear shows an FA of 0.233.

DISCUSSION

Our study found significantly lower FA values using DTI in cranial nerves VII and VIII with NVC at the cerebellopontine angle in ears with neurocompressive syndrome than in asymptomatic ears with NVC. FA provides additional information for assessing NVC in patients with neurocompressive syndrome. Incorporating DTI in the evaluation of the cerebellopontine angle offers further insight, which can improve the clinical-radiological classification and reinforce the need to complement an anatomical evaluation with functional quantitative techniques.

Previous DTI reports on cranial nerves have demonstrated decreased FA in patients with neurocompressive syndrome or cranial neuralgias, particularly at the root entry/exit zone[3,5,11]. Several reports have shown a relationship between direct contact of a vascular loop with a nerve and the presence of vertigo, tinnitus, and hemifacial spasm[8,12,13]. The use of DTI to measure FA has recently increased because it reflects demyelination of white matter fibers. Our study, using DTI MRI, showed a significant difference between ears with NVC and neurocompressive syndrome, with a mean FA of 0.218, and asymptomatic NVC ears with a mean of 0.294 ($p < 0.001$). Ears with NVC presenting neurocompressive syndrome with hemifacial spasm, tinnitus or vertigo had a significantly lower FA than asymptomatic NVC ears. These findings show an FA behavior consistent with that reported by other authors[5,6]. Kierig et al.[6] conducted a comparative study at the Interdisciplinary German Center for Vertigo and Balance Disorders that included 36 adults, 18 with vestibular paroxysm (52.6 ± 18.1 years) and 18 asymptomatic (50.3 ± 16.5 years). In the study of the VIII cranial nerve entry/exit zone, a 3.0T MRI (Magnetom Skyra, Siemens Healthcare, Erlangen, Germany) was used to evaluate vestibular NVC. By combining DTI sequences for vestibular nerve angulation with delayed post-gadolinium acquisition and processing via DSI Studio software (http://dsi-studio.labsolver.org/), a significant difference in FA was observed. The mean FA was lower (0.150) in nerves affected by vestibular paroxysm compared to those without

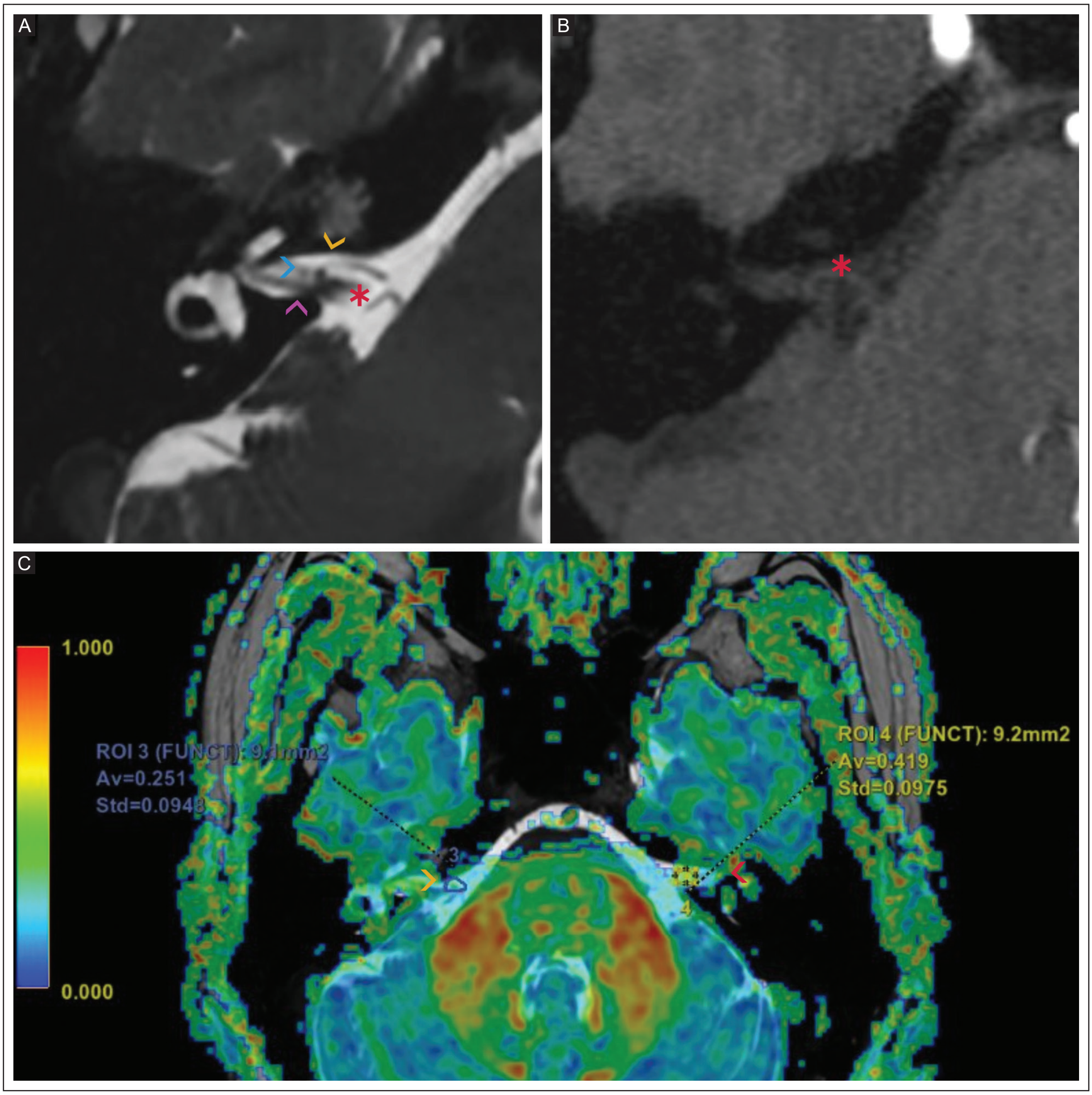

Figure 2. A 3.0T MRI of a 61-year-old man with tinnitus. **A:** the T2-weighted CUBE shows a right NVC Chavda type II (yellow arrowhead) with an anteroinferior cerebellar artery loop (asterisk) extending less than 50% into the internal auditory canal (purple arrowhead), adjacent to the nerve complex VII/VIII (blue arrowhead). **B:** a 3D-TOF shows an anteroinferior cerebellar artery loop (asterisk) in the internal auditory canal. **C:** a DTI T2 CUBE showing fusion with decreased FA of 0.251 in the ROI at the level of the NVC (yellow arrowhead). The contralateral ear shows FA of 0.419 (red arrowhead).

DTI: diffusion tensor imaging; 3D-TOF: three-dimensional time of flight; T: Tesla; MRI: magnetic resonance imaging; NVC: neurovascular contact; FA: fractional anisotropy: ROI: region of interest.

vestibular paroxysm (0.170; $p < 0.05$). Jin et al.[5] at the Department of Neurosurgery of the First Affiliated Hospital of China Medical University performed a prospective study of 40 patients with primary hemifacial spasm. These patients underwent DTI with a 3.0T MRI scanner and DSI Studio software before microvascular decompression. They were followed up at 6 months and one year after surgery with DTI. The mean FA (0.430) of the affected side was significantly lower than the healthy side (FA 0.460) ($p < 0.05$). There is no standard value to define FA reduction in NVC. The trend toward decreased FA in the studies by Jin et al.[5] and Kierig et al.[6] is similar to our study; however, the FA values are not directly comparable because our measurements were performed manually by placing the ROI at the level of the NVC, including all fibers of the voxel.

Table 4. Gorrie grades of NVC and FA quantified by DTI MRI in cranial nerves VII and VIII comparing ears with and without neurocompressive syndrome

Description		Gorrie grade A FA				Gorrie grade B FA				Gorrie grade C FA		
	(n = 3)	Mean	SD	p	(n = 79)	Mean	SD	p	(n = 17)	Mean	SD	p
With neurocompressive syndrome	2	0.211	0.14	0.102	26	0.211	0.49	0.001	5	0.259	0.066	0.490
Without neurocompressive syndrome	1	0.324	-		53	0.296	0.069		12	0.284	0.067	
Neurocompressive syndrome[a]												
Hemifacial spasm												
Yes	1	0.201	-	0.565	5	0.208	0.035	0.065	0	-	-	-
No	2	0.273	0.072		74	0.272	0.075		17	0.277	0.066	
Tinnitus												
Yes	1	0.201	-	0.565	16	0.227	0.029	0.001	4	0.232	0.032	0.126
No	2	0.273	0.072		63	0.278	0.079		13	0.291	0.068	
Vertigo												
Yes	1	0.222	-	0.769	11	0.189	0.062	0.001	2	0.288	0.111	0.818
No	2	0.262	0.086		68	0.280	0.068		15	0.275	0.064	

[a] Eight ears had two or more symptoms.

FA: fractional anisotropy; DTI: diffusion tensor imaging; MRI: magnetic resonance imaging; NVC: neurovascular contact; SD: standard deviation.

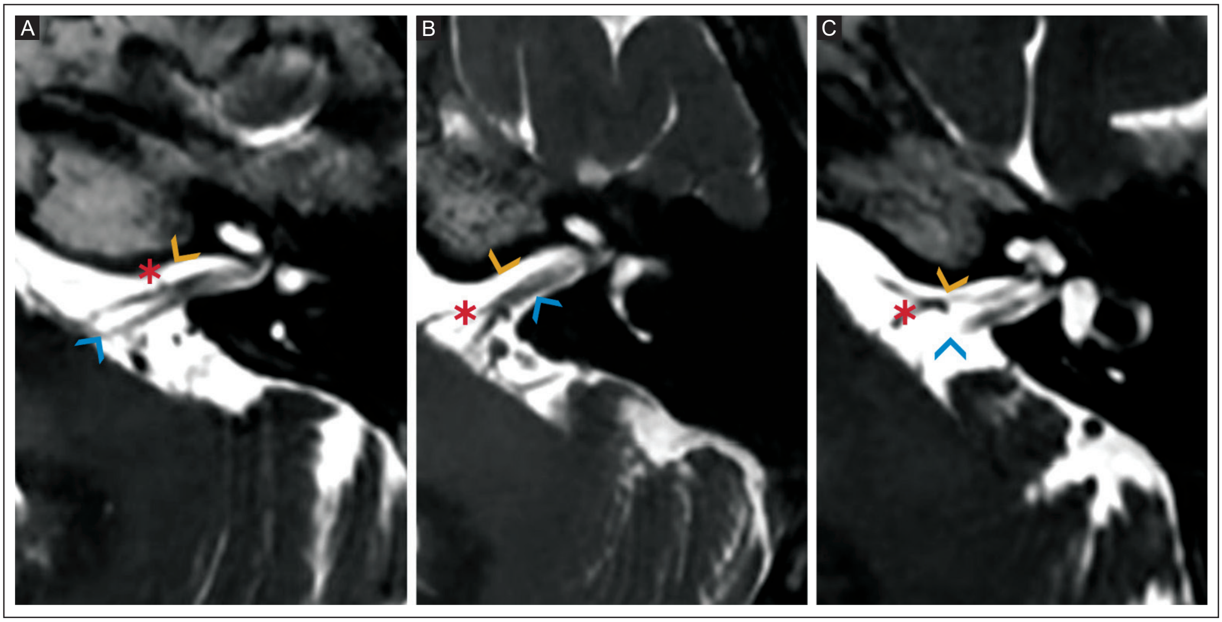

Figure 3. 3.0T MRI T2- weighted CUBE shows the Gorrie grade of contact between the vascular loop and the VIII nerve. **A:** a 72-year-old asymptomatic woman with NVC Gorrie grade A (yellow arrowhead) shows an anteroinferior cerebellar artery loop (asterisk) without contact with the adjacent VII/VIII nerve complex (blue arrowhead). **B:** a 61-year-old woman with hemifacial spasm, shows NVC Gorrie grade B (yellow arrowhead) with an anteroinferior cerebellar artery loop (asterisk) running adjacent to the VII/VIII nerve complex (blue arrowhead). **C:** a 58-year-old man with vertigo, shows NVC Gorrie grade C (yellow arrowhead) with an anteroinferior cerebellar artery loop (asterisk) coursing between the VII/VIII nerve complex (blue arrowhead).

T: Tesla; MRI: magnetic resonance imaging; VII: facial nerve; VIII: vestibulocochlear nerve; NVC: neurovascular contact.

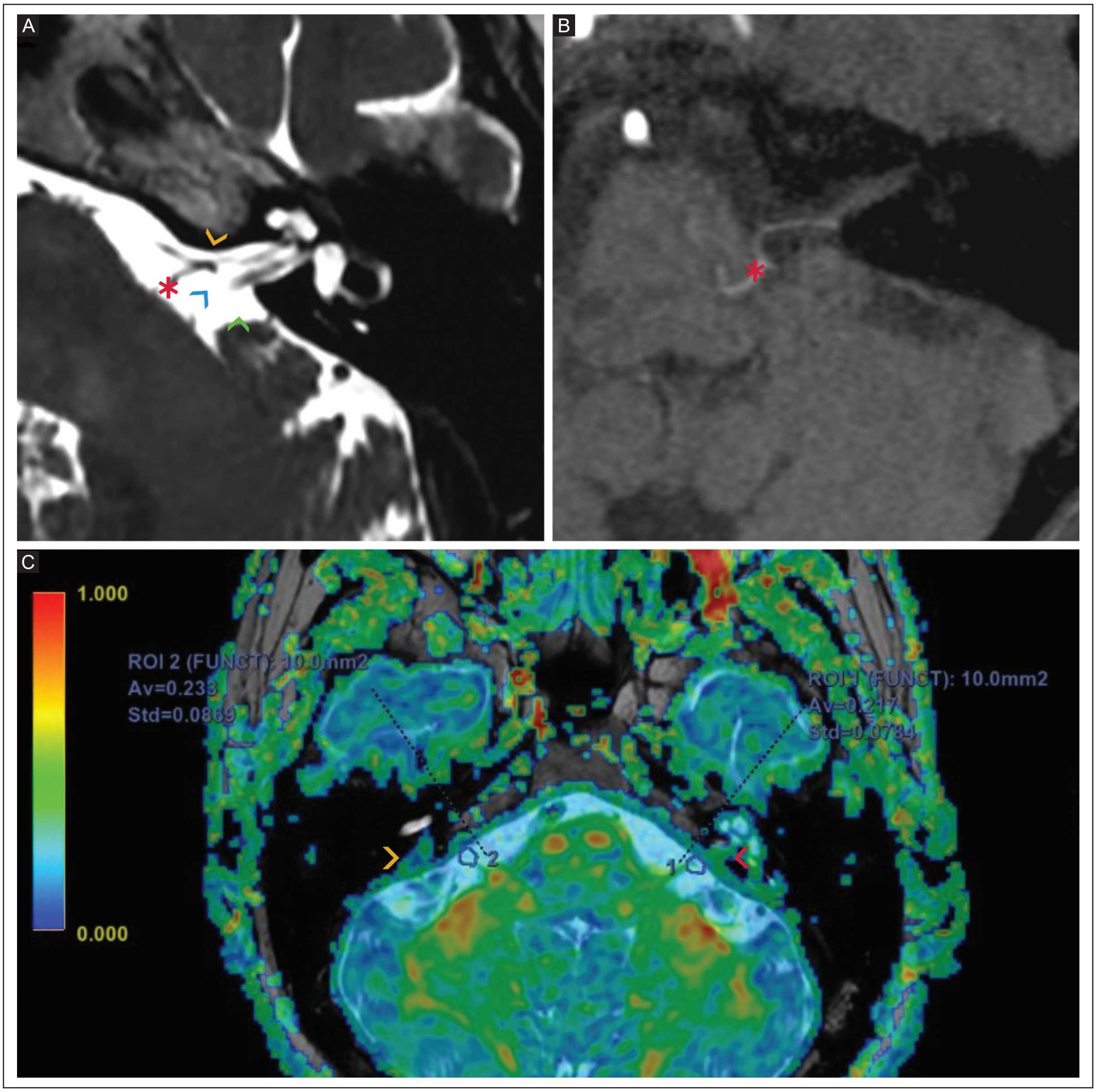

Figure 4. A 3.0T MRI of a 58-year-old man with tinnitus and vertigo. **A:** T2-weighted CUBE shows NVC Chavda type I and Gorrie grade C (yellow arrowhead) on the left side in the cerebellopontine angle (green arrowhead). **B:** the 3D-TOF demonstrates the vascular loop (asterisk) in the cerebellopontine angle. **C:** a DTI T2-weighted CUBE fusion shows decreased FA of 0.217 in the ROI at the level of the NVC (red arrowhead). The contralateral ear shows FA of 0.233 (yellow arrowhead).

DTI: diffusion tensor imaging; 3D-TOF: three-dimensional time of flight; T: Tesla; MRI: magnetic resonance imaging; NVC: neurovascular contact; FA: fractional anisotropy; ROI: region of interest.

They used DSI Studio software, which eliminates voxels containing crossing fibers, resulting in a lower anisotropy fraction than when performed manually. DTI allows the identification of microstructural alterations in cranial nerves VII and VIII associated with neurocompressive syndrome. FA is a useful quantitative parameter for differentiating incidental NVC from clinically symptomatic NVC, providing additional diagnostic value in the radiological evaluation of the cerebellopontine angle.

Neurocompressive syndromes caused by NVCs are usually due to arteries that directly contact the cisternal portion at the entry/exit points of cranial nerves[14]. Chavda type I, located in the cerebellopontine angle cistern, is the most common type of NVC[3,15]. McDermott et al.[9] conducted a prospective study in the UK of 332 adults with unilateral tinnitus or asymmetrical hearing loss. 3D constructive interference in steady-state MRI was performed. They found that Chavda type I was the most common contact, but the presence of tinnitus did not differ across neurovascular contact types. In contrast, Chavda type II of NVC showed a significant difference in the presence of hearing loss between the 126 affected and 76 non-affected sides ($p = 0.016$). Our study showed that Chavda type I was the most common NVC, with a significant difference in the presence of tinnitus or vertigo in affected ears compared to asymptomatic ears with Chavda type I NVC. Chavda type II was less common and showed no significant difference in the presence of tinnitus compared to asymptomatic ears. Our findings showed a higher frequency of Chavda type I and a trend toward an association with neurocompressive syndrome.

The Gorrie classification provides a common language describing the presence of a vascular loop and its specific location, correlating with the patient's symptoms[10,15]. In our study, Gorrie grade B was the most common NVC. Tinnitus and vertigo showed significant differences with lower FA than in asymptomatic ears. Bae et al.[16] conducted a retrospective study in South Korea on 25 patients diagnosed with typewriter tinnitus. Patients were classified into three groups: group 1 (symptomatic side), group 2 (asymptomatic side), and group 3 (patients with dizziness). They underwent MRI with conventional sequences at the level of the internal auditory canal and the cerebellopontine angle. The type of NVC was classified into three categories: type I, no neurovascular contact, similar to Gorrie grade A; type II, neurovascular contact present at the cochleovestibular nerve complex but without angulation or indentation of the nerve, similar to Gorrie grade B; and type III, neurovascular compression causing cochleovestibular nerve angulation or indentation similar to Gorrie grade D. NVC type III was significantly higher on the symptomatic sides of patients with typewriter tinnitus than in the other groups. The findings suggested that greater contact between the vascular loop and the cranial nerve is associated with neurocompressive syndrome.

This study has several strengths. DTI was performed by a radiology technician, with MRI parameters meticulously modified by a medical physicist with 15 years of experience in MRI based on the physical and anatomical characteristics of cranial nerves VII and VIII in the cerebellopontine angle. The scanner included the requirement for post-processing and software for FA measurement. This study also has limitations that need to be considered. The small sample size and the use of only a 3.0T MRI scanner limit data reproducibility. The sample size and cross-sectional design also limit causal inference regarding the association between decreased FA and neurocompressive syndrome. Evaluating cranial nerves using DTI is technically challenging due to their small size, proximity to cerebrospinal fluid, and susceptibility to motion and distortion artifacts. Additionally, the lack of standardized protocols for DTI acquisition and analysis in cranial nerves hinders direct comparisons between studies.

CONCLUSION

DTI MRI showed significantly lower FA in cranial nerves VII and VIII with NVC in the cerebellopontine angle in ears with neurocompressive syndrome compared with asymptomatic ears with NVC. While asymptomatic NVC does not alter FA values, neurocompressive syndrome is consistently associated with a significant decrease in FA. These findings reinforce DTI as a diagnostic complement and a potential biomarker in NVC assessment. From a neuroradiology perspective, our results support the use of DTI as a complement to high-resolution anatomical sequences, providing quantitative information on nerve integrity. Further studies with larger populations are needed to confirm the consistency of significant differences in ears with NVC with or without neurocompressive syndromes of cranial nerves VII and VIII in the cerebellopontine angle.

Acknowledgments

The authors thank the technician Jorge O. Bravo-Gamboa for acquiring the images for this study. The authors thank Professor Ana M. Contreras-Navarro for her guidance in preparing and writing this scientific paper. This original research in the Radiology Specialty field was an awarded thesis at the *Tercera Convocatoria Nacional 2024-2025 "Las Mejores Tesis para Publicar en el JMeXFRI"*.

Funding

The authors declare that they have not received funding.

Conflicts of interest

The authors declare no conflicts of interest.

Ethical considerations

Protection of human subjects and animals. The authors declare that the procedures followed were in accordance with the ethical standards of the responsible committee on human experimentation and with the World Medical Association and the Declaration of Helsinki (1964). The procedures were authorized by the Institutional Ethics Committee.

Confidentiality, informed consent, and ethical approval. The authors have followed their institution's confidentiality protocols, obtained informed consent from all patients, and secured approval from the Ethics Committee. SAGER guidelines have been followed as applicable to the nature of the study.

Declaration on the use of artificial intelligence. The authors declare that no generative artificial intelligence was used in the writing or creation of the content of this manuscript.

REFERENCES

1. Guclu B, Sindou M, Meyronet D, Streichenberger N, Simon E, Mertens P. Cranial nerve vascular compression syndromes of the trigeminal, facial and vago-glossopharyngeal nerves: comparative anatomical study of the central myelin portion and transitional zone; correlations with incidences of corresponding hyperactive dysfunctional syndromes. Acta Neurochir (Wien). 2011;153(12):2365-2375. doi: 10.1007/s00701-011-1168-1.
2. Szmyd B, Sołek J, Błaszczyk M, Jankowski J, Liberski PP, Jaskólski D, et. al. The underlying pathogenesis of neurovascular compression syndromes: a systematic review. Front Mol Neurosci. 2022;15:923089. doi:10.3389/fnmol.2022.923089.
3. Zhang G, Li H, Zhao Z, Zhang M, Zou J. Location of the AICA influences the severity but not occurrence of ISSNHL: a reappraisal using high-resolution 3T MRI. J Otol. 2023;18(4):193-198. doi: 10.1016/j.joto.2023.07.001.
4. Zhang J, Yu Q, Gu P, Sun H, Yuan F, Zhang Q. Brain structure alterations in hemifacial spasm: a diffusion tensor imaging study. Clin EEG Neurosci. 2022;53(2):165-172. doi: 10.1177/1550059420979250.
5. Jin Z, Li Z. Clinical application of diffusion tensor imaging in diagnosis and prognosis of hemifacial spasm. World Neurosurg. 2021;145:e14-e20. doi: 10.1016/j.wneu.2020.08.049.
6. Kierig E, Gerb J, Boegle R, Ertl-Wagner B, Dieterich M, Kirsch V. Vestibular paroxysmia entails vestibular nerve function, microstructure and endolymphatic space changes linked to root-entry zone neurovascular compression. J Neurol. 2023;270(1):82-100. doi: 10.1007/s00415-022-11399-y.
7. Liang C, Yang L, Reichardt W, Zhang B, Li R. Different MRI-based methods for the diagnosis of neurovascular compression in trigeminal neuralgia or hemifacial spasm: a network meta-analysis. J Clin Neurosci. 2023;108:19-24. doi:10.1016/j.jocn.2022.12.016.
8. Di Stadio A, Dipietro L, Ralli M, Faralli M, Volpe A, Ricci G et. al. Loop characteristics and audio-vestibular symptoms or hemifacial spasm: is there a correlation? A multiplanar MRI study. Eur Radiol. 2020;30(1): 99-109. doi:10.1007/s00330-019-06309.
9. McDermott A, Dutt S, Irving R, Pahor A, Chavda SV. Anterior inferior cerebellar artery syndrome: fact or fiction. Clin Otolaryngol Allied Sci. 2003;28(2):75-80. doi: 10.1046/j.1365-2273.2003.00662.x.
10. Gorrie A, Warren F, De la Garza A, Shelton CW. Is there a correlation between vascular loops in the cerebellopontine angle and unexplained unilateral hearing loss? Otol Neurotol. 2010;31(1):48-52. doi: 10.1097/MAO.0b013e3181c0e63a.
11. Lutz J, Linn J, Mehrkens JH, Thon N, Stahl R, Seelos K, et al. Trigeminal neuralgia due to neurovascular compression: high-spatial-resolution diffusion-tensor imaging reveals microstructural neural changes. Radiology. 2011;258(2):524-530. doi: 10.1148/radiol.10100477.
12. Kazawa N, Togashi K, Ito J. The anatomical classification of AICA/PICA branching and configurations in the cerebellopontine angle area on 3D-drive thin slice T2WI MRI. Clin Imaging. 2013;37(5):865-870. doi: 10.1016/j.clinimag.2011.11.021
13. Nowé V, De Ridder D, Van de Heyning PH, Wang XL, Gielen J, Van Goethem J, et al. Does the location of a vascular loop in the cerebellopontine angle explain pulsatile and non-pulsatile tinnitus? Eur Radiol. 2004;14(12):2282-2289. doi: 10.1007/s00330-004-2450-x.
14. Leng Y, Lei P, Liu Y, Chen C, Xia K, Liu B. Vascular loops in cerebellopontine angle in patients with unilateral idiopathic sudden sensorineural hearing loss: Evaluations by three radiological grading systems. Laryngoscope Investig Otolaryngol. 2022;7(5):1532-1540. doi:10.1002/lio2.876.
15. Kim SH, Ju YR, Choi JE, Jung JY, Kim SY, Lee MY. Anatomical location of AICA loop in CPA as a prognostic factor for ISSNHL. PeerJ. 2019;7: e6582. doi:10.7717/peerj.6582.
16. Bae Y, Jeon Y, Choi B, Koo J, Song J. The role of MRI in diagnosing neurovascular compression of the cochlear nerve resulting in typewriter tinnitus. AJNR Am J Neuroradiol. 2017;38(6):1212-1217. doi: 10.3174/ajnr.A5156.

Journal of the Mexican Federation
of Radiology and Imaging

PICTORIAL ESSAY

Superficial prepatellar and infrapatellar bursitis: a pictorial essay

Josue Solis-Ugalde[1,2]*, *Bruno Solis-Ugalde*[3] and *Ronald Ocampo-Chacon*[1]

[1]*Department of Medical Imaging, Hospital del Trauma;* [2]*Department of Medical Imaging, MedCare Center. San Jose, Costa Rica;* [3]*Radiology Department, Memorial Sloan Kettering Cancer Center, New York, NY, USA*

ABSTRACT

Because bursae play an essential role in mobility, their pathological entity –bursitis– requires specialized medical care. Superficial prepatellar bursitis and superficial infrapatellar bursitis are common causes of anterior knee inflammation and pain. This pictorial essay provides a detailed description of imaging findings and broadens the spectrum of conditions affecting the superficial prepatellar and superficial infrapatellar bursae. Ultrasound (US) is a first-line diagnostic tool because of its high sensitivity, wide availability, low cost, and ability to guide interventional diagnostic and therapeutic procedures. Magnetic resonance imaging (MRI) complements US in complex cases, allowing detailed evaluation of bursal contents and adjacent structures and excluding intra-articular abnormalities. Traumatic superficial prepatellar and infrapatellar bursitis are classified as aseptic, septic, or hemorrhagic; each has specific clinical and imaging characteristics. The differential diagnosis of superficial prepatellar and superficial infrapatellar bursitis of the knee includes soft tissue collections, hematomas, scar-related lesions, patellar tendon pathology, bone lesions, and, less frequently, tumors. Superficial prepatellar and superficial infrapatellar bursitis can develop as postoperative complications of anterior knee procedures, especially those involving the patella or the patellar tendon. The cause and severity determine treatment. Most cases respond well to conservative management, including PRICE therapy (protection, rest, ice, compression, and elevation) and non-steroidal anti-inflammatory drugs. Accurate imaging assessment of superficial prepatellar and superficial infrapatellar bursitis is essential to ensure appropriate management.

Keywords: *Superficial prepatellar bursitis. Superficial infrapatellar bursitis. Knee bursae. Ultrasound. Magnetic resonance imaging. Computed tomography.*

INTRODUCTION

Technological advances have enabled a qualitative leap in the study of organs and anatomical structures, including their function, pathological changes, and mechanisms of injury. The topic in this pictorial essay – the study of bursae – is essential for recognizing the diagnostic accuracy and detailed information provided by high-resolution ultrasound (US) and magnetic resonance imaging (MRI), thereby facilitating appropriate medical and surgical treatment decisions.

In ancient times, bursae were not studied as independent structures but were considered elements associated with joints and body movement. Hippocrates (2nd century BC) and Galen (2nd century AD) described them without assigning a specific name. It is also known that, even in antiquity, thermal baths were recommended for the treatment of inflammation and movement limitations[1]. The term *bursa* began to be used during the Middle Ages. It derives from Latin and means “bag” or “pouch,” referring to containers used to store coins or wine. The term was adopted in both anatomical and

***Corresponding author:**
Josue Solis-Ugalde
E-mail: jsolisu@gmail.com

Received for publication: 04-10-2025
Accepted for publication: 26-12-2025
DOI: 10.24875/JMEXFRI.M26000122

Available online: 16-04-2026
J Mex Fed Radiol Imaging. 2026;5(1):46-60
www.JMeXFRI.com

stock exchange terminology. The formal and systematic study of bursae in medicine is relatively recent[2].

Bursae are fluid-filled structures located between the skin and a tendon, or between a tendon and a bone[3]. Most bursae form during embryonic development; however, some are not present at birth and develop gradually with age as mechanical friction increases. The human body contains approximately 140 bursae[4]. Their main function is to minimize friction between adjacent moving structures[3]. They are classified according to their location as subcutaneous, subfascial, subtendinous, and submucosal[3]. Bursae can be divided into two types: anatomical and adventitial. Anatomical bursae are true synovial-lined fluid-filled sacs located near joints.

In contrast, adventitial bursae lack a synovial lining and may be located farther from the joint; therefore, they are also considered accidental bursae[3]. A limited number of reports describe the superficial prepatellar and superficial infrapatellar bursae. Most articles focus on anatomical aspects or are case reports of severe bursitis treated with minimally invasive techniques or surgery. This pictorial essay broadens the spectrum of conditions affecting the superficial prepatellar and infrapatellar bursae of the anterior knee and provides a detailed description of their imaging findings.

ANATOMY OF THE SUPERFICIAL PREPATELLAR BURSA

This superficial prepatellar bursa is located anterior to the patella, between the patella, the quadriceps tendon, and the overlying subcutaneous tissue. It is a small superficial structure centered over the patella, although it may project beyond the lateral border by a few millimeters[5]. It is oriented in the coronal plane in all cases.

Anatomically, the anterior bursae of the knee, particularly the superficial prepatellar bursa, have a complex trilaminar organization, which explains their diverse pathological patterns. The trilaminar configuration of the superficial prepatellar bursa consists of fibrous soft-tissue over the patella[6]. These structures, from superficial to deep, include (Figure 1):

- *A superficial compartment*, known as the subcutaneous prepatellar bursal space, is located between the subcutaneous tissue and the transverse superficial fascia (fascia lata).
- *An intermediate compartment, or subfascial prepatellar bursal space*, is situated between the transverse superficial fascia and the intermediate oblique fascia, which is formed by fascial extensions of the vastus lateralis and vastus medialis muscles.
- *The deepest compartment, or subaponeurotic prepatellar bursal space*, is located between the intermediate oblique fascia and the deep longitudinal fibers of the rectus femoris tendon, which inserts directly on the patella[6].

This trilaminar arrangement was found in 93% of cases in cadaveric study by Dye et al.[6] and in 78% in a study by Aguiar et al.[5], who also reported a bilaminar pattern in 22%**.** There are no reports of a unilaminar or unicameral pattern, as previously suggested in older anatomy textbooks[5]. The superficial prepatellar bursa normally does not communicate with the knee joint, except in cases of patellar tendon rupture (Figure 2).

ANATOMY OF THE SUPERFICIAL INFRAPATELLAR BURSA

The superficial infrapatellar bursa, located adjacent to the distal insertion of the patellar tendon, is one of the bursae surrounding the knee[7]. It has clinical and imaging characteristics similar to those of the superficial prepatellar bursa.

This bursa has both superficial and deep components[7]. The superficial component lies over the patellar tendon and is most often involved in bursitis. In some pathological situations, the superficial prepatellar and superficial infrapatellar bursae may communicate with each other[7].

IMAGING DIAGNOSIS OF BURSITIS

X-ray

The role of X-ray in evaluating superficial bursae of the knee is limited. Plain radiography is primarily used to assess adjacent bone structures and, on anteroposterior and lateral projections, to evaluate soft tissues indirectly. The lateral X-ray projection is the most useful view for evaluating anterior knee soft tissues. Its main usefulness is in identifying associated fractures and detecting soft-tissue swelling or subcutaneous emphysema anterior to the patella. These findings may be relevant in the acute setting, particularly in the context of trauma or infection[8].

Plain radiographs may show dystrophic or heterotopic calcifications, which are common in chronic or complicated bursitis or in some differential diagnoses involving the anterior aspect of the knee. X-ray also serves a complementary role in postoperative patients, allowing evaluation of surgical hardware position and identification of potential complications related to previous interventions[9] (Figures 3 A and B).

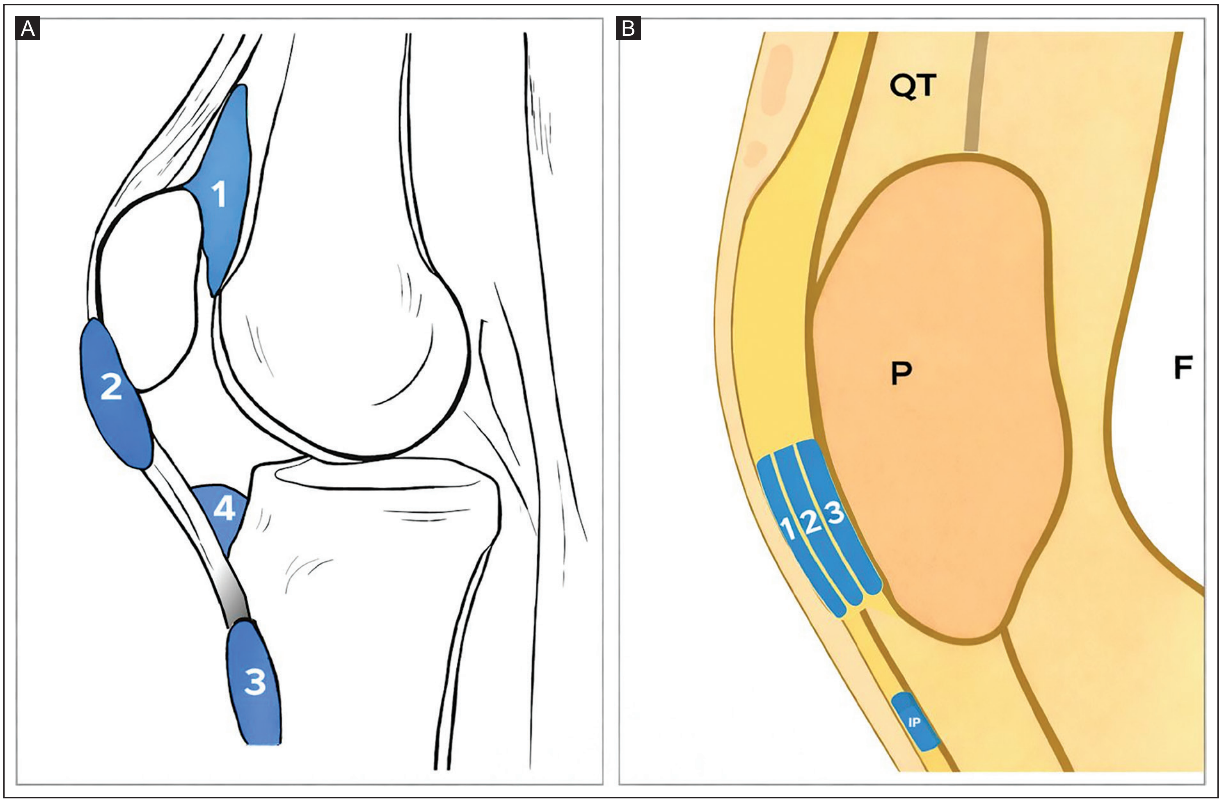

Figure 1. A: bursae of the anterior compartment of the knee highlighted in blue: (1) suprapatellar, (2) superficial prepatellar, (3) superficial infrapatellar, and (4) deep infrapatellar. **B:** illustration shows compartmentalization of the superficial prepatellar bursa highlighted in blue: (1) superficial compartment, or prepatellar subcutaneous bursal space, between subcutaneous tissue and transverse superficial fascia; (2) intermediate compartment, or prepatellar subfascial bursal space, between transverse superficial fascia and intermediate oblique fascia; (3) deepest compartment, or prepatellar subaponeurotic bursal space, between intermediate oblique fascia and deep longitudinal fibers of the rectus femoris tendon, which inserts directly into the patella. This illustration serves as an anatomical reference for the pictorial essay. *Modified from Aguiar et al.*[5]

F: femur; QT: quadriceps tendon; PT: patellar tendon; IP: infrapatellar bursa; P: patella.

Ultrasound

US is the imaging modality of choice to assess superficial prepatellar and superficial infrapatellar bursae[10]. It is operator-dependent and, in some cases, considered limited for this reason. The location of the superficial prepatellar bursae allows adequate evaluation, even by personnel with limited US experience, making it a useful, versatile, cost-effective procedure[11]. US enables assessment of the subcutaneous tissue and multiple knee structures. Current high-resolution equipment allows the detection of small amounts of fluid.

US allows evaluation of intrinsic bursal characteristics, such as synovial thickening, septations, or internal heterogeneity, findings commonly associated with hemorrhagic, subacute, or chronic processes[10,12]. US diagnosis of bursitis of the superficial bursae of the anterior aspect of the knee may be based solely on identification of a hypoechoic fluid collection, always in the context of the patient's clinical presentation[12] (Figures 3C and D). Dynamic maneuvers can be performed to assess the functional involvement of the joint. Real-time interaction with the patient during the US examination allows questioning and provides valuable information about the mechanism of injury or the patient´s current clinical status.

A wide range of differential diagnoses can be identified by correlating ultrasound findings with the patient's clinical presentation. US is the modality of choice for interventional procedures, such as fluid aspiration for diagnosis, therapeutic injections, and placement of percutaneous catheters[10,13].

Comparative studies show the high specificity of US versus MRI for superficial bursitis with good sensitivity in expert hands, although some deep bursae or small collections may go undetected[14,15].

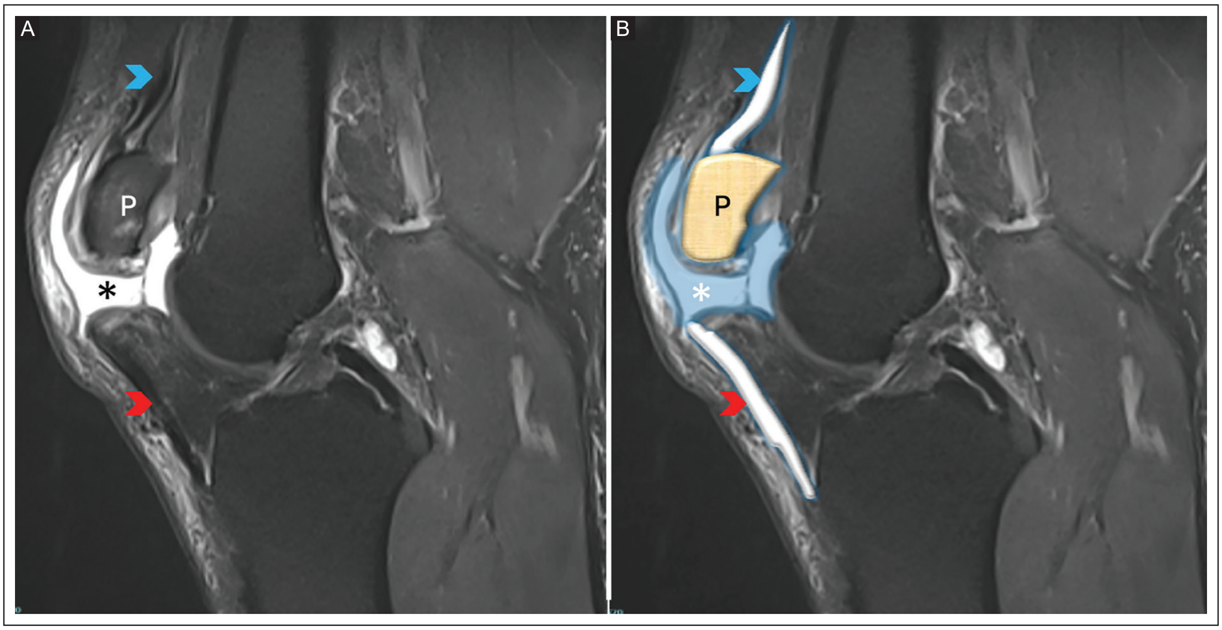

Figure 2. A-B: sagittal proton density-weighted knee MRI with fat suppression in a 42-year-old man shows complete patellar tendon rupture, characterized by fiber discontinuity and marked hyperintense fluid signal at the tear site (red arrowheads). There is abnormal hyperintense fluid communication between the knee joint and the superficial prepatellar bursa (asterisks), highlighted in blue. The patella is shown in brown. The quadriceps tendon is intact (blue arrowheads).

MRI: magnetic resonance imaging; P: patella.

Computed tomography

Computed tomography (CT) plays a secondary role in evaluating the superficial bursae of the anterior knee. Nevertheless, it is a useful modality with high resolution for assessing bone structures, particularly for detecting associated fractures[16]. Its soft-tissue characterization capability is limited, with performance similar to conventional X-ray; however, it allows identification of findings such as emphysema, calcifications, and edema[16] (Figure 3E and F). Dual-energy computed tomography (DECT) is a new tool for soft-tissue evaluation. It offers emerging opportunities in a field where the utility of CT has traditionally been limited[16]. However, its scope has not been clearly defined in superficial prepatellar and infrapatellar bursitis.

In postoperative patients, CT allows adequate evaluation of surgical hardware and identification of potential complications[16]. However, exposure to ionizing radiation limits its routine use; it should be reserved for selected cases.

Magnetic resonance imaging

MRI offers greater anatomical and tissue resolution and superior characterization of the bursal wall, soft-tissue edema, deep-plane extension, and bone complications (such as osteomyelitis). MRI is more sensitive for detecting secondary findings, such as bone contusions, signal changes in adjacent tendons, and complex intrabursal masses. MRI is useful when clinical findings or US suggest complications or when detailed preoperative mapping is required[7,17].

MRI provides advantages, including the evaluation of associated findings and assessment of the internal structures of the knee, as well as the added benefit of avoiding ionizing radiation[8,18]. MRI exhibits high tissue differentiation, making it the ideal complementary modality to US, particularly in complex cases[14,18] (Figure 4).

MRI identifies bursal fluid content and soft-tissue edema, making it useful for differentiating simple bursitis from hemorrhagic, infectious, or chronic processes[8]. It also enables evaluation of synovial thickening, internal septations, debris, and fluid-fluid levels, a characteristic finding related to blood products of different ages and sedimentation effects that can help support the diagnosis to distinguish it from other soft-tissue collections or neoplastic processes[19,20] (Figure 5). The use of contrast media allows improved assessment of the bursal wall and tissue behavior in equivocal cases[18].

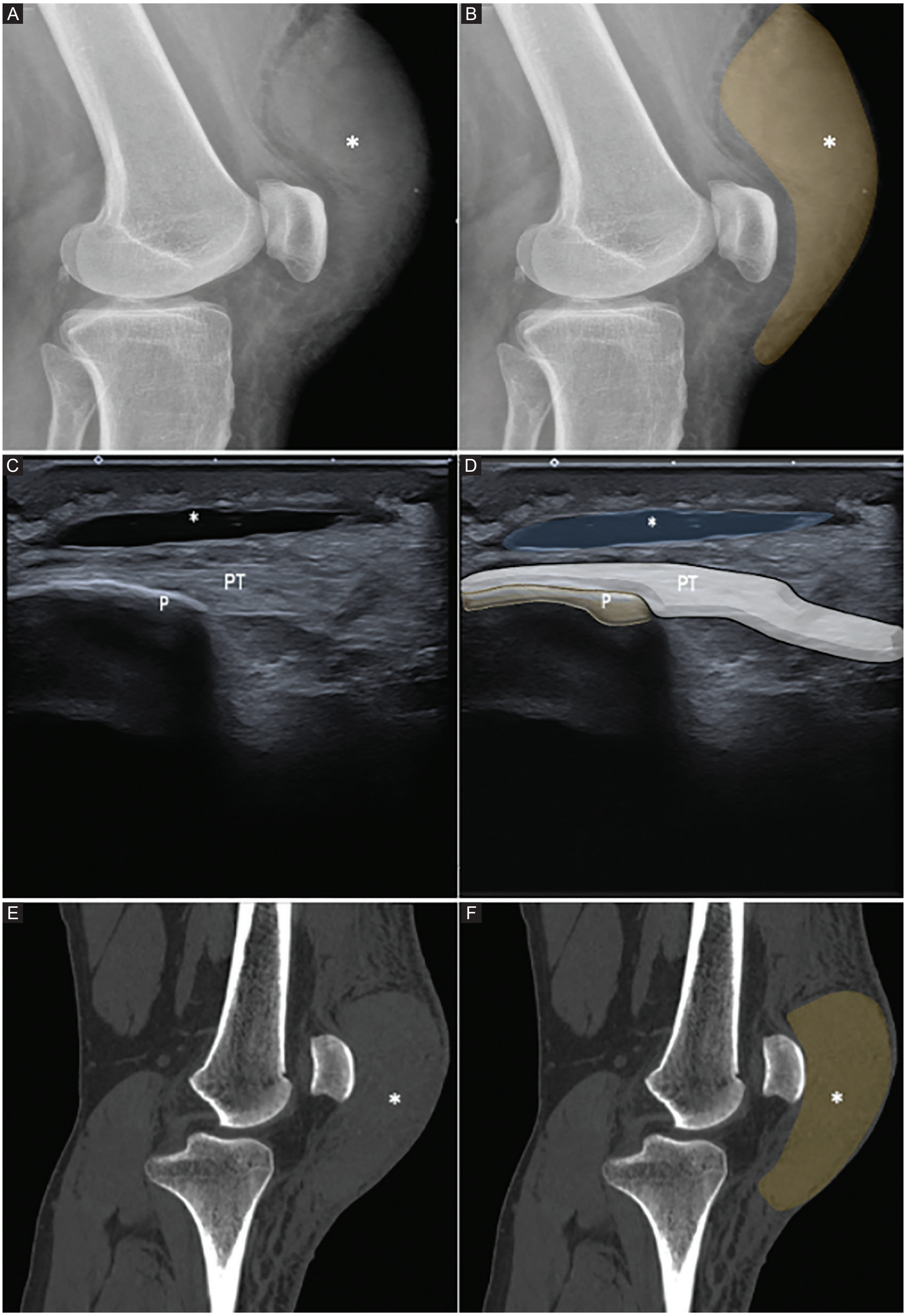

Figure 3. A-B: lateral knee X-rays in a 59-year-old woman show prominent soft-tissue swelling anterior to the patella (asterisks), highlighted in brown, consistent with prepatellar soft-tissue edema. **C-D:** sagittal US views show prepatellar bursitis, characterized by a well-defined anechoic collection of the prepatellar bursa (asterisks), superficial to the patella, with a thin wall and absence of vascularization, highlighted in blue, suggestive of aseptic (post-traumatic) bursitis. **E-F:** sagittal CT views show soft-tissue edema anterior to the patella (asterisks), highlighted in brown, with no associated bone abnormalities.

US: ultrasound; CT: computed tomography; P: patella; PT: patellar tendon.

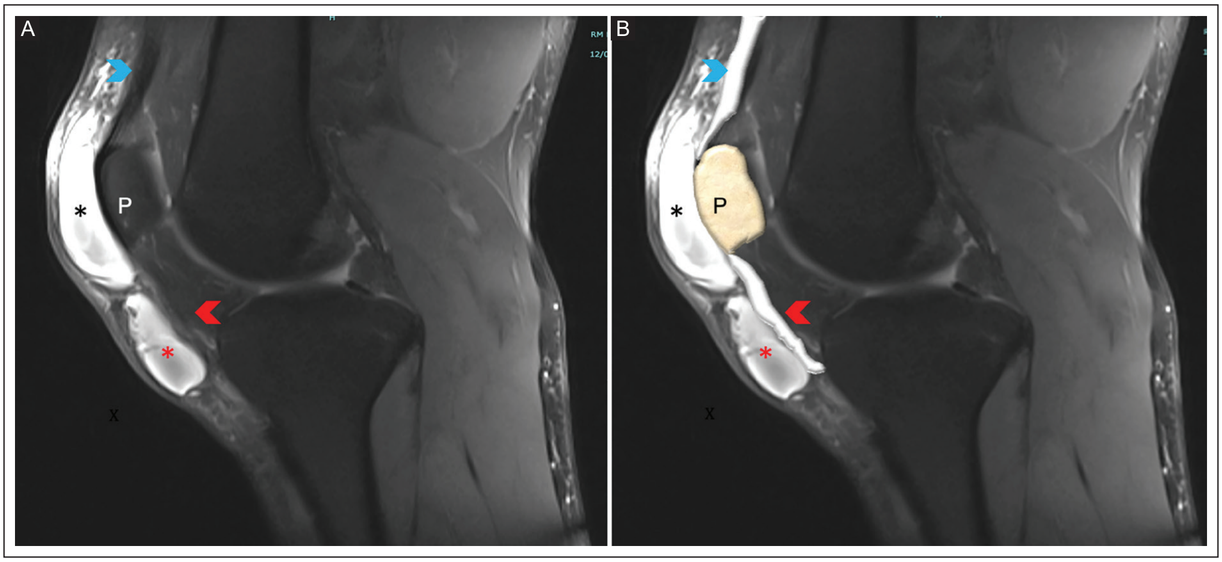

Figure 4. A-B: sagittal proton density-weighted knee MRI with fat suppression in a 29-year-old woman shows a well-defined hyperintense fluid collection involving the superficial prepatellar (black asterisks), and superficial infrapatellar (red asterisks) bursae without imaging evidence of communication between them. The patellar tendon has preserved contour and homogeneous low signal intensity (red arrowheads). The quadriceps tendon is intact, with normal signal intensity (blue arrowheads).

MRI: magnetic resonance imaging; P: patella.

MRI is particularly valuable for assessing involvement of adjacent structures, such as the patellar tendon, Hoffa's fat pad, subcutaneous tissue, and the patella, allowing exclusion of associated pathologies, such as soft-tissue tumors, fibrocicatricial changes, or intra-articular lesions[8].

Despite its advantages, MRI is not usually a first-line procedure due to its higher cost and limited availability compared to US. Therefore, MRI is reserved for cases with suspected complications, lack of treatment response, deep extension, or to refine complex differential diagnoses[7,14].

Recommendations for imaging report of bursitis

- Specify the affected anatomical bursa (superficial prepatellar or superficial infrapatellar) and note any compartmentalization if present[7].
- Describe the contents (anechoic, hyperechoic, heterogeneous), wall thickness, post-contrast enhancement (if MRI), peribursal edema, and adjacent bone findings[17,21].
- Identify findings suggesting infection (circumferential mural enhancement, gas, marked inflammatory edema) and recommend image-guided aspiration when appropriate[15,21].
- Suggest additional imaging modalities (e.g., MRI if US indicates deep extension or bone involvement) and recommend a clinical-microbiological correlation[7,14].
- Emphasize findings that (a) differentiate bursitis from other cystic or soft tissue lesions, (b) recognize signs suggestive of infection or complication, and (c) optimize the imaging algorithm and communication with the clinical or surgical team[7,14,17,21].

CLINICAL PATHOLOGIES

The diagnosis of superficial prepatellar and superficial infrapatellar pathology is primarily clinical, but multimodal imaging (US and MRI) provides critical information on location, extent, and complications such as abscesses, extension into adjacent tissues, or osteomyelitis. They also help guide procedures such as needle aspiration or surgery[7,14,17,22].

The superficial prepatellar bursa is particularly susceptible to compression and repetitive microtrauma, which are common in professions that require kneeling. Superficial prepatellar bursitis can be acute or chronic with synovial thickening and septations.

Aseptic bursitis

Traumatic superficial prepatellar bursitis can be aseptic or septic. Aseptic superficial bursitis occurs after minor, repetitive trauma in people whose occupations

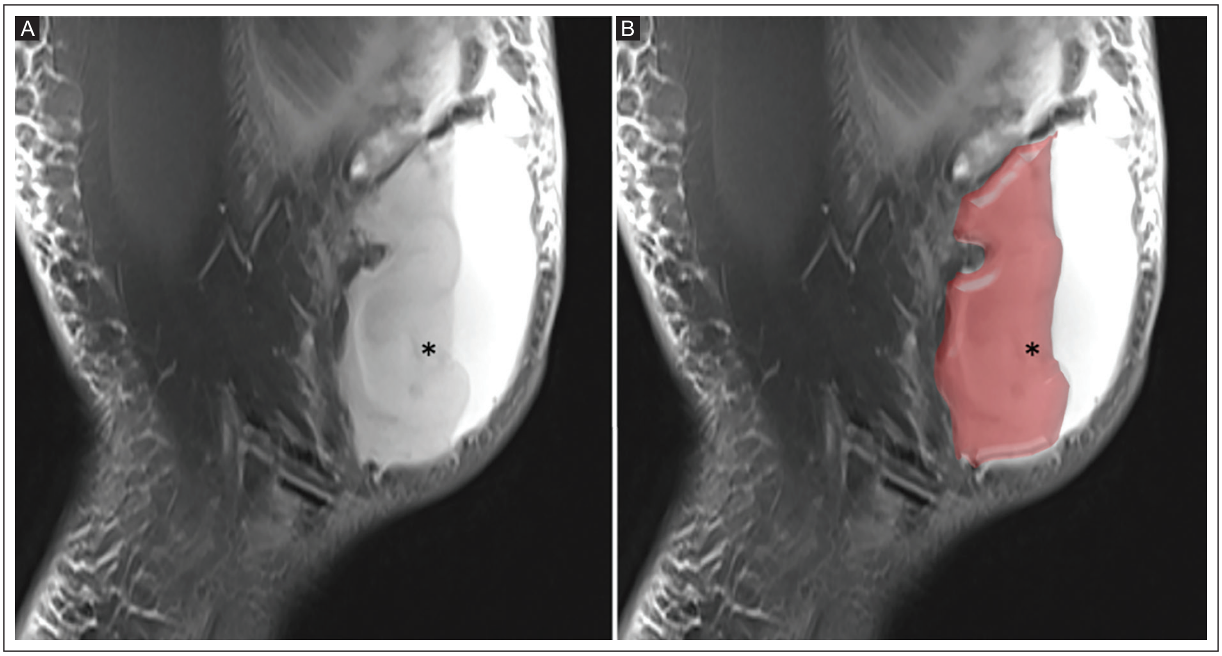

Figure 5. A-B: sagittal proton density-weighted knee MRI with fat suppression in a 22-year-old man demonstrates a markedly distended superficial prepatellar bursa containing a heterogeneous fluid collection with fluid-fluid levels, showing dependent hypointense sedimented components and nondependent hyperintense fluid signal superiorly (asterisks), consistent with hemorrhagic bursitis. The bursal extent is highlighted in red.

MRI: magnetic resonance imaging.

require prolonged kneeling, such as carpet installers and cleaning staff[4]. Superficial prepatellar bursitis, which involves excessive accumulation of fluid in both superficial anterior knee bursae, is commonly known as "maid's knee" when it affects the superficial prepatellar bursa (Figure 6) and "cleric's knee" when the superficial infrapatellar bursa is involved (Figure 7). The appearance of superficial prepatellar and infrapatellar aseptic bursitis is consistent with fluid on US and MRI[4].

US is a helpful screening method, with a sensitivity of 87% for detecting fluid in the anterior knee bursae compared with MRI as the gold standard[4]. With modern high-resolution US, even small amounts of anechoic fluid can be detected. This finding must always be interpreted in the clinical context. Other causes of aseptic prepatellar bursitis include systemic diseases such as gout, rheumatoid arthritis, collagen vascular disorders, and inflammatory arthropathy[23].

Septic bursitis

Superficial prepatellar and superficial infrapatellar septic bursitis account for approximately one-third of all bursitis cases and represent between 0.01% and 0.1% of hospital admissions[24]. The infection is believed to occur through direct inoculation rather than hematogenous spread, likely because of the limited blood supply to the bursa[24] (Figure 8).

Diagnosis is primarily clinical. US can help identify hypoechoic fluid accompanied by synovial thickening and hypertrophy[24]. In some cases, thin septations and increased vascularity on power Doppler US may be observed, which provide useful diagnostic and therapeutic guidance[24]. Associated soft tissue edema is almost always present. There is a lack of consensus on standardized ultrasound or Doppler parameters that best predict infection[10].

The presence of circumferential bursal mural thickening and enhancement on MRI, peripheral enhancement after contrast administration, marked peribursal edema, a heterogeneous collection with debris, and gas in soft tissues increases the likelihood of septic or abscessed bursitis and should prompt urgent aspiration and antibiotic management. However, overlaps are frequent: chronic bursitis with hemorrhage or tophi (gout) can show heterogeneous content and enhancement; therefore, clinical correlation and microbiological/crystal aspiration analysis remain the gold standard for distinguishing etiologies[15].

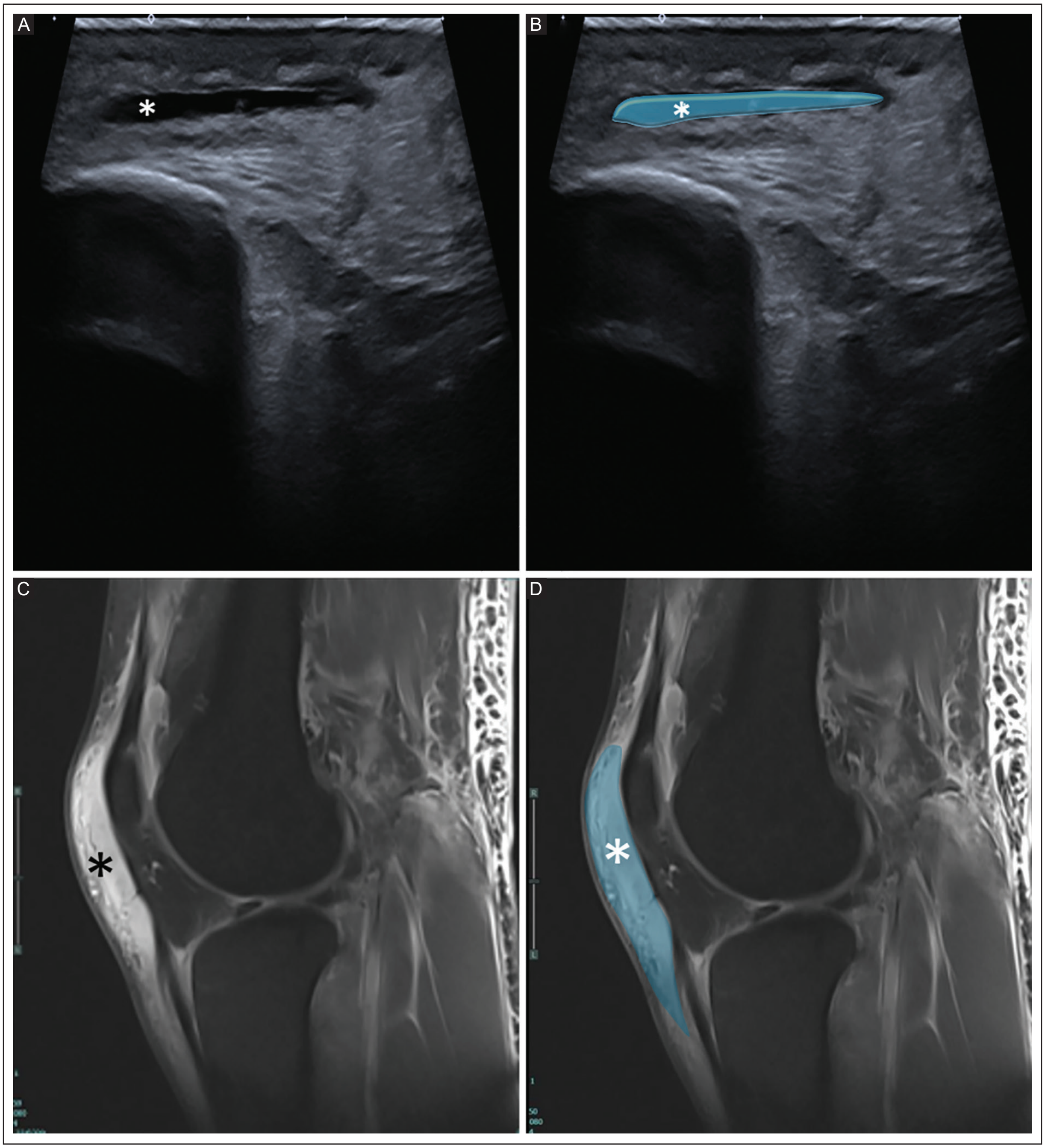

Figure 6. A-B: sagittal knee US in a 30-year-old man shows superficial prepatellar bursitis, characterized by well-defined anechoic fluid collection in the prepatellar bursa (asterisks), highlighted in blue. **C-D:** sagittal proton density-weighted knee MRI with fat suppression shows a marked hyperintense fluid signal distending the superficial prepatellar bursa (asterisks), highlighted in blue, consistent with superficial prepatellar bursitis ("housemaid's knee").

US: ultrasound; MRI: magnetic resonance imaging.

Hemorrhagic bursitis

Hemorrhagic bursitis is commonly post-traumatic, although it can also occur as a postsurgical complication[19,20]. Hemorrhagic bursitis has been extensively described in the literature, largely due to the significant size these lesions can reach. Progressive enlargement can result in visible cosmetic deformity, leading to limited joint mobility and impaired quality of life[19].

Its appearance on US is variable and typically characterized by predominantly heterogeneous and poorly defined echogenicity, usually without central vascularity

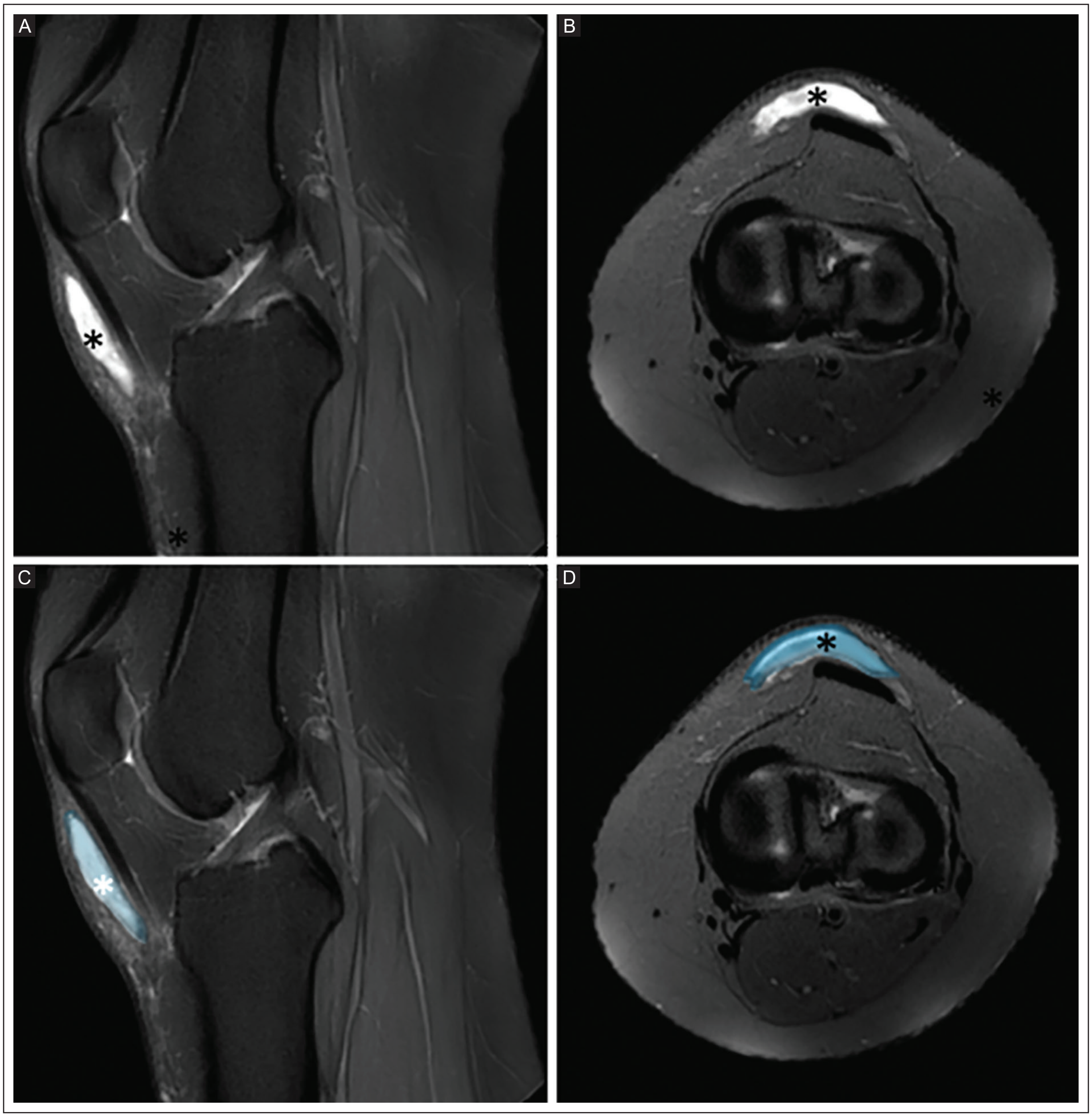

Figure 7. A, B, C, D: sagittal and axial proton density-weighted knee MRI with fat suppression in a 35-year-old man shows superficial infrapatellar bursitis, characterized by fluid collection in the superficial infrapatellar bursa (asterisks). The bursa is highlighted in blue. This condition is commonly referred to as "clergyman's knee."

MRI: magnetic resonance imaging.

on color Doppler imaging. In some cases, hemorrhagic bursitis may show a more complex ultrasonographic appearance, including internal septations, debris, or calcifications, particularly in chronic or organized stages[19] (Figure 9). Unlike hematomas in other anatomical regions, hemorrhagic bursae tend to become predominantly organized over time, often developing a fibrous capsule and internal complexity. Several cases requiring surgical management have been reported due to their large size, persistent symptoms, or functional compromise (Figure 10).

Postsurgical and/or iatrogenic bursitis

Patellar surgeries can affect the superficial prepatellar bursa more than the infrapatellar bursa[25]; therefore, cases of bursitis associated with these procedures may be encountered (Figure 11). However, surgeries

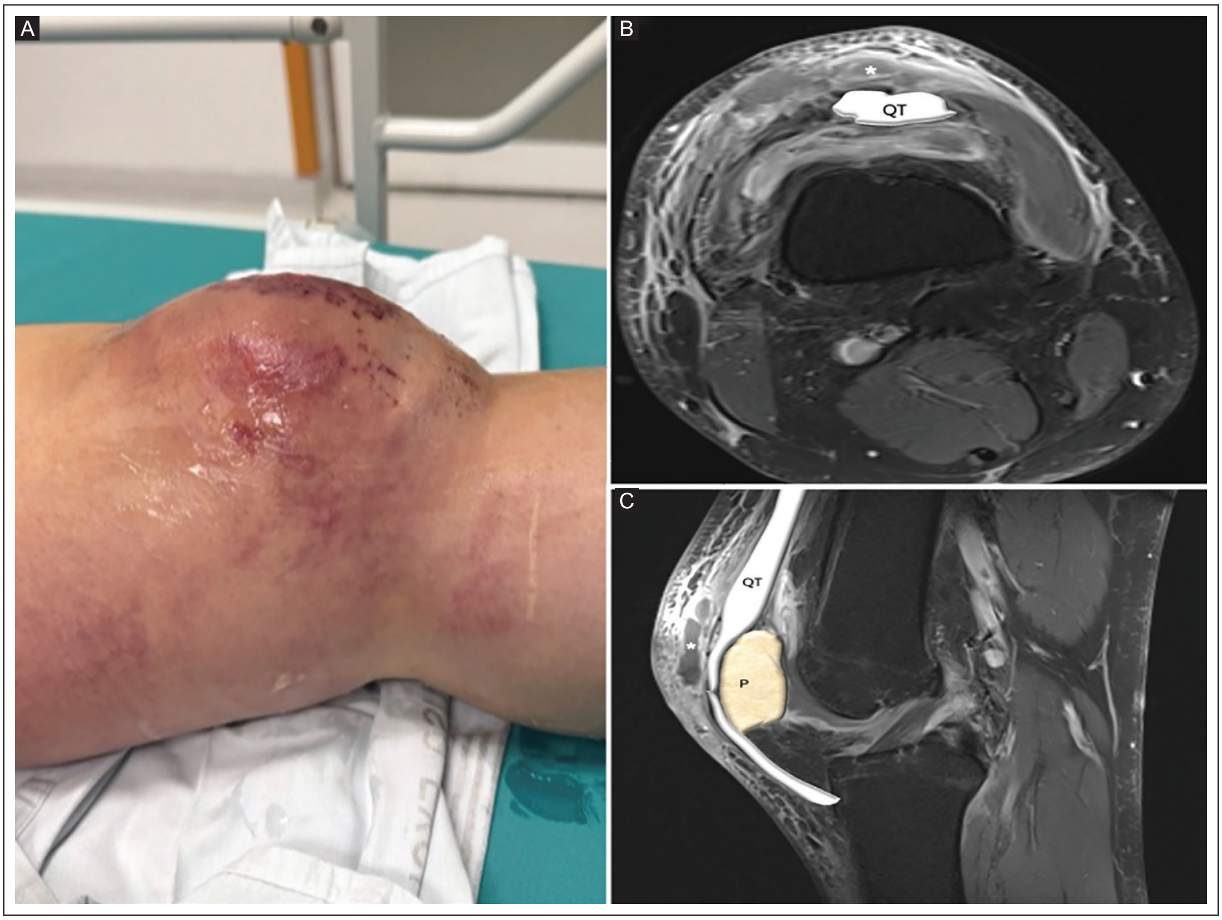

Figure 8. A: clinical photograph of the left knee in a 53-year-old man shows marked edema, erythema, and superficial skin abrasions over the anterior aspect of the knee, suggestive of septic prepatellar bursitis, commonly caused by direct inoculation through skin disruption. **B:** axial T1-weighted fat-suppressed post-contrast knee MRI shows a hypointense fluid collection in the superficial prepatellar bursa (asterisk) with peripheral bursal wall enhancement and a hyperintense anterior subcutaneous edema. **C:** axial T1-weighted fat-suppressed post-contrast knee MRI shows a hypointense fluid collection in the superficial prepatellar bursa (asterisk) with peripheral bursal wall enhancement and hyperintense anterior subcutaneous edema.

MRI: magnetic resonance imaging; P: patella; QT: quadriceps tendon.

involving the patellar tendon may affect the superficial infrapatellar bursa, making bursitis a potential complication of this type of intervention[25].

DIFFERENTIAL DIAGNOSES

Various soft-tissue conditions of the anterior knee are included in the differential diagnoses. Among these, extensive soft tissue hematomas and Morel-Lavallée hematomas are important considerations, as they can mimic intrabursal collections. Therefore, the clinical history (such as trauma or metabolic disease) and characterization by MRI or fluid analysis are essential[17,21]. These lesions are often associated with previous trauma and tend to occur in regions adjacent to the superficial bursae of the anterior knee (Figures 12 A and B). They result from shearing forces that separate the subcutaneous tissue from the underlying fascia. Due to their characteristic anatomical location, extent, and distribution, differentiation from superficial prepatellar bursitis on US and MRI is usually straightforward.

Injuries to adjacent supporting structures should also be considered, including post-traumatic scarring and thickening of the prepatellar ligament. These changes are commonly observed after direct trauma and are typically characterized by predominant posterior fibrotic thickening. Both US and MRI are valuable in this setting, with MRI providing crucial information for accurate anatomical assessment and differential diagnosis (Figures 12 C-F). High-energy motorcycle injuries are a frequent cause of these types of injuries.

Soft-tissue masses such as lipomas can mimic bursal pathology. Lipomas generally grow slowly with minimal clinical symptoms. On US, they appear as solid lesions

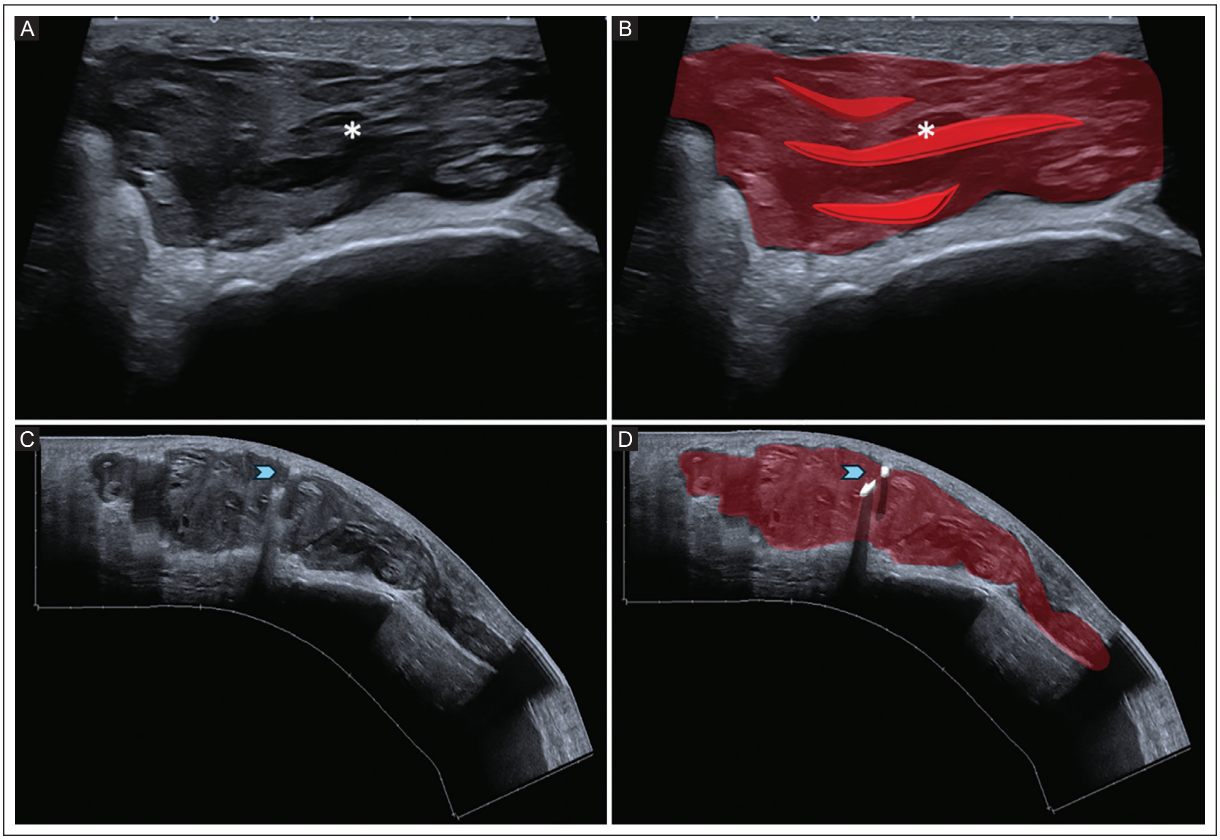

Figure 9. A-B: axial US views of the anterior knee in a 21-year-old woman show hemorrhagic bursitis with an organized hematoma within the bursa (asterisks), highlighted in red. The lesion shows heterogeneous content and echogenic fragments consistent with debris or hemorrhage, one of the most common ultrasonographic features of acute hemorrhagic bursitis. **C-D:** sagittal US images of the anterior knee in a 43-year-old woman show hemorrhagic bursitis with an organized hematoma highlighted in red, containing internal calcifications highlighted in white (blue arrowheads), findings suggestive of chronicity. In the absence of previous trauma, gout should be considered in the differential diagnosis.
US: ultrasound.

with absent or minimal Doppler vascularity. At the same time, MRI shows distinctive signal intensity characteristics, including high signal intensity on T1-weighted images and signal suppression on fat-suppressed sequences. Importantly, these lesions are located outside the normal bursal topography, facilitating differentiation from true bursitis. Osgood-Schlatter disease should also be included in the differential diagnosis, particularly in cases of superficial infrapatellar bursitis, especially in younger patients.

Postsurgical complications and less common entities within the differential diagnosis, including tendon-related abnormalities and soft-tissue tumors, should not be overlooked. Other less frequent differential diagnoses include tuberculosis, crystal deposition diseases such as gout and calcium pyrophosphate deposition disease (pseudogout), and systemic conditions including rheumatoid arthritis, systemic lupus erythematosus, and uremia[4,23].

A high index of suspicion should be maintained for osteomyelitis or intraosseous conditions in pediatric or immunocompromised patients that initially present with prepatellar swelling. MRI should be considered to evaluate bone involvement[4].

TREATMENT OF BURSITIS

Imaging identifies the affected bursa and helps determine the treatment plan. The treatment of aseptic superficial prepatellar and superficial infrapatellar bursitis is determined first by the underlying cause and, secondly, the pathological changes within the bursa[23]. Management of acute bursitis includes PRICE therapy (protection, rest, ice, compression, and elevation) and non-steroidal anti-inflammatory drugs, which generally provide an adequate response[4]. Patients with septic superficial prepatellar bursitis are managed successfully with non-surgical treatment, including rest, compression, immobilization, aspiration, and antibiotics[23].

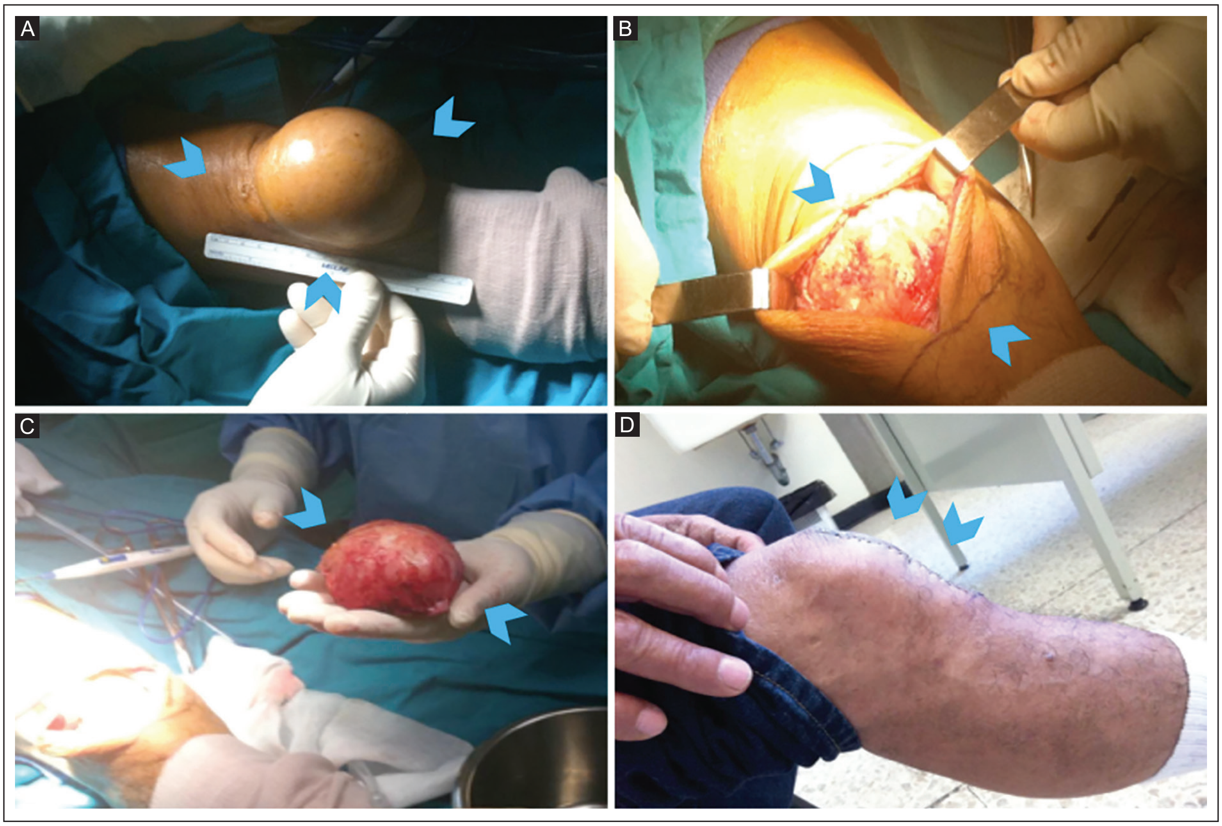

Figure 10. Clinical and intraoperative photographs of a 59-year-old man diagnosed with hemorrhagic superficial prepatellar bursitis. **A:** marked anterior knee swelling (blue arrowheads). **B:** intraoperative exposure of a hemorrhagic prepatellar bursal lesion (blue arrowheads). **C:** surgical specimen showing a large, organized hemorrhagic bursa (blue arrowheads). Post-traumatic hemorrhagic bursae are typically among the largest. **D:** postoperative clinical appearance showing resolution of anterior knee swelling after surgical excision (blue arrowheads).

Surgery is not required in most cases; however, when necessary – particularly in recurrent or treatment-refractory cases – available medical procedures include aspiration and intrabursal injection of an appropriate agent, such as corticosteroids, platelet-rich plasma, autologous blood, sclerosing solutions, and short-term placement of a drainage catheter as a therapeutic option. Excision of a chronically inflamed and thickened bursa is uncommon for superficial prepatellar and superficial infrapatellar bursae[23,26].

Collections with signs of suppuration or deep extension require aspiration, culture, and often systemic antibiotics. Persistent or recurrent, and massive or chronic collections with fibrotic tissue may require bursectomy (open or endoscopic). Open bursectomy carries a significant risk of morbidity of the surgical site, including poor wound healing, decreased scar sensation, contracted scarring, atrophic skin changes, accumulation of subcutaneous hematomas, and painful or hypersensitive scarring[23]. This risk is related to the delicate blood supply of the prepatellar skin and the rich network of anastomoses formed by the descending vertical branches of the anterior divisions of the medial and lateral femoral cutaneous nerves, the intermediate cutaneous nerve, and the infrapatellar branch of the saphenous nerve[23]. Recent systematic reviews show that endoscopic bursectomy is non-inferior to open bursectomy for prepatellar resection in terms of recurrence and is associated with a shorter hospital stay, supporting fewer invasive options when intervention is necessary[4,27].

CONCLUSION

A wide range of pathologies can affect the superficial prepatellar and superficial infrapatellar bursae. Advances in contemporary imaging techniques, particularly high-resolution US and MRI, have significantly improved diagnostic accuracy, enabling more precise characterization of these conditions and facilitating optimal therapeutic decisions. The pathology involving these bursae is wide-ranging, and their anatomy is more complex than traditionally appreciated. Trauma predominates, encompassing

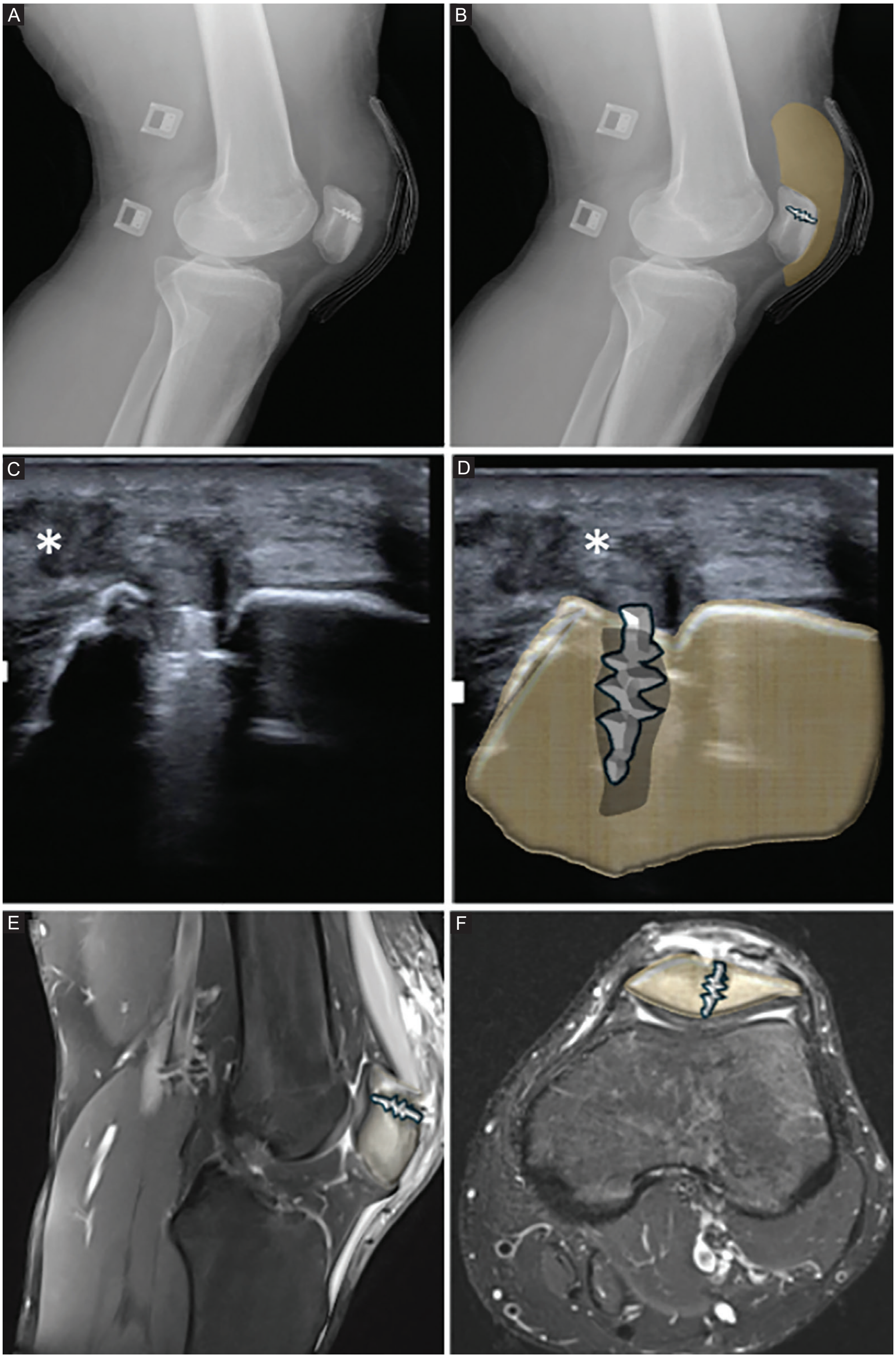

Figure 11. A-B: lateral knee X-rays of a 17-year-old man show the patella with a surgical tendon anchor system and anterior soft-tissue swelling, highlighted in brown. **C-D:** longitudinal US of the anterior knee shows postoperative soft-tissue edema and fluid collection in the prepatellar bursa (asterisks). The patella is highlighted in brown with the surgical tendon anchor system. **E-F:** sagittal and axial proton density-weighted knee MRI with fat suppression shows postoperative anterior soft-tissue edema, characterized by heterogeneous signal in the prepatellar soft tissues with hyperintense fluid distension of the superficial prepatellar bursa. The patella is highlighted in brown. Findings are consistent with postsurgical superficial prepatellar bursitis following a patellar procedure.

US: ultrasound; MRI: magnetic resonance imaging.

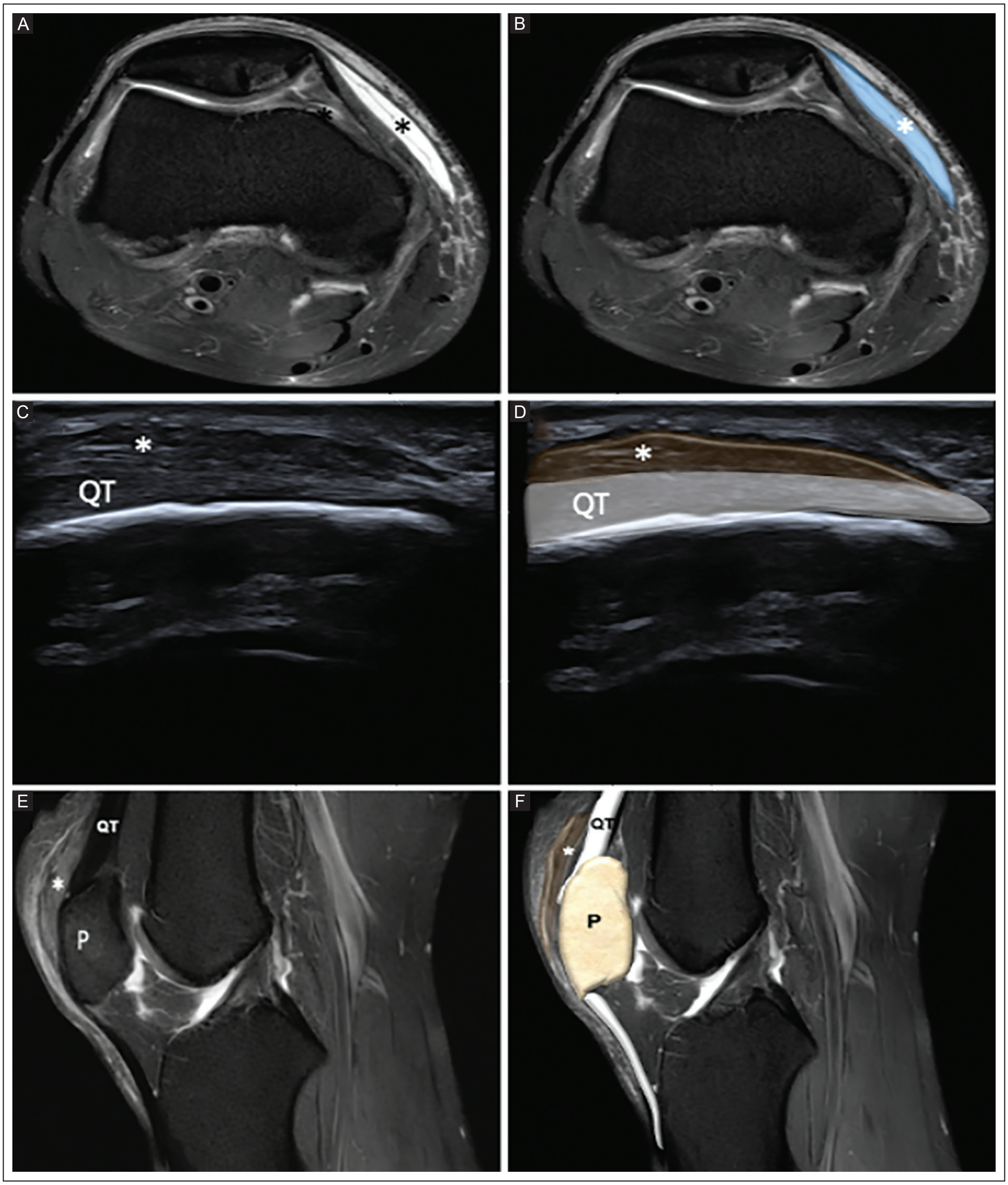

Figure 12. A-B: axial proton density-weighted knee MRI with fat suppression in a 17-year-old man shows post-traumatic hematoma along the medial aspect of the knee, located in soft tissue (asterisks) and highlighted in blue. No prepatellar bursa involvement is observed. **C-D:** longitudinal US view of the anterior knee shows post-traumatic fibrotic thickening of the prepatellar tendon, characterized by focal tendon enlargement with a predominantly hypoechoic echotexture and changes in the normal fibrillar pattern (asterisks). The affected tendon segment is highlighted in dark brown. **E-F:** sagittal proton density-weighted knee MRI views with fat suppression show post-traumatic fibrotic thickening of the prepatellar tendon (asterisks), characterized by tendon enlargement with predominantly low signal intensity and focal areas of intermediate signal, without fiber discontinuity or hyperintense fluid signal suggesting tendon rupture. The affected tendon is highlighted in dark brown.

MRI: magnetic resonance imaging; US: ultrasound; P: patella; QT: quadriceps tendon.

low- and high-energy mechanisms. Accurate imaging diagnosis and appropriate management depend on identifying the underlying cause and understanding the biological behavior of the bursae. US is the primary imaging modality for puncture guidance, while MRI is used for detailed evaluation of complications or complex differential diagnoses.

Acknowledgments

The authors thank Professor Ana M. Contreras-Navarro for her guidance in preparing and writing this scientific paper. The authors thank Dr. Akira Kobayashi-Pinto for the postsurgical photo clinical case.

Funding

The authors declare that they have not received funding.

Conflicts of interest

The authors declare no conflicts of interest.

Ethical considerations

Protection of human subjects and animals. The authors declare that the procedures followed were in accordance with the ethical standards of the responsible committee on human experimentation and with the World Medical Association and the Declaration of Helsinki (1964) and amendments.

Confidentiality, informed consent, and ethical approval. The authors have obtained approval from the Ethics Committee for the analysis of routinely collected and anonymized clinical data; therefore, individual informed consent was not required. Relevant ethical recommendations have been followed.

Declaration on the use of artificial intelligence. The authors declare that no generative artificial intelligence was used in the writing or creation of the content of this manuscript.

REFERENCES

1. Gianfaldoni S, Tchernev G, Wollina U, Roccia MG, Fioranelli M, Gianfaldoni R, et al. History of the baths and thermal medicine. Open Access Maced J Med Sci. 2017; 23;5(4):566-568. doi: 10.3889/oamjms.2017.126.
2. Dyche B. Anatomy word of the month: bursa. Iowa IA. USA: Des Moines University, Medicine and Health Sciences; 2011 Jan 1 (cited November 5, 2025). Available from: https://www.dmu.edu/blog/2011/01/anatomy-word-of-the-month-bursa.
3. Singh A, Devgan A, Kaur S, Singh P. Knee cap bursitis/housemaid's knee role of magnetic resonance imaging: a case report. Indian J Case Reports. 2021;7(3):102-104. doi:10.32677/IJCR.2021.v07.i03.009.
4. Baumbach SF, Lobo CM, Badyine I, Mutschler W, Kanz KG. Prepatellar and olecranon bursitis: literature review and development of a treatment algorithm. Arch Orthop Trauma Surg. 2014;134(3):359-370. doi: 10.1007/s00402-013-1882-7.
5. Aguiar RO, Viegas FC, Fernandez RY, Trudell D, Haghighi P, Resnick D. The prepatellar bursa: cadaveric investigation of regional anatomy with MRI after sonographically guided bursography. AJR Am J Roentgenol. 2007;188(4):W355-W358. doi:10.2214/AJR.06.0960.
6. Dye SF, Campagna-Pinta D, Dye CC, Shiflett S, Eiman T. Soft tissue anatomy anterior to the human patella. J Bone Joint Surg Am. 2003; 85(6):1012-1017. doi:10.2106/00004623-200305000-000.
7. Viegas FC, Aguiar RO, Gasparetto E, Marchiori E, Trudell DJ, Haghighi P, et al. Deep and superficial infrapatellar bursae: cadaveric investigation of regional anatomy using magnetic resonance after ultrasound-guided bursography. Skeletal Radiol. 2007;36(1):41-46. doi: 10.1007/s00256-006-0142-0.
8. Steinbach LS, Stevens KJ. Imaging of cysts and bursae about the knee. Radiol Clin North Am. 2013;51(3):433-454. doi: 10.1016/j.rcl.2012.10.005.
9. Hwang ZA, Suh KJ, Chen D, Chan WP, Wu JS. Imaging features of soft-tissue calcifications and related diseases: a systematic approach. Korean J Radiol. 2018;19(6):1147-1160. doi: 10.3348/kjr.2018.19.6.114.
10. Hasan M, Berkovich Y, Khatib M, Steinfeld Y, Sleiman A, Ben Zvi L, et al. knee bursae: a comprehensive review of clinical evaluation, imaging differentiation, and the expanding role of biologic therapies. Cartilage. 2025:19476035251362434. doi: 10.1177/19476035251362434. Epub ahead of print.
11. Turecki MB, Taljanovic MS, Stubbs AY, Graham AR, Holden DA, Hunter TB, et al. Imaging of musculoskeletal soft tissue infections. Skeletal Radiol. 2010;39(10):957-971. doi: 10.1007/s00256-009-0780-0.
12. Iriarte I, Pedret C, Balius R, Cerezal L. Ultrasound of the musculoskeletal system: anatomical exploration and pathology. 1st ed. Sainz R. Barcelona: Editorial Médica Panamericana; 2021. p. 292-295.
13. Flores DV, Mejía Gómez C, Pathria MN. Layered approach to the anterior knee: normal anatomy and disorders associated with anterior knee pain. Radiographics 2018;38 (7):2069-2101. doi: 10.1148/rg.2018180048.
14. Draghi F, Corti R, Urciuoli L, Alessandrino F, Rotondo A. Knee bursitis: a sonographic evaluation. J Ultrasound. 2015;18(3):251-257. doi:10.1007/s40477-015-0168-z.
15. Herring K, Mathern S, Khodaee M. Septic infrapatellar bursitis in an immunocompromised female. Case Rep Orthop. 2018;2018:9086201. doi: 10.1155/2018/9086201.
16. Fritz B, Fritz J. MR imaging of acute knee injuries: systematic evaluation and reporting. Radiol Clin North Am. 2023;61(2):261-280. doi: 10.1016/j.rcl.2022.10.005.
17. Hirji Z, Hunjun JS, Choudur HN. Imaging of the bursae. J Clin Imaging Sci. 2011;1:22. doi:10.4103/2156-7514.80374.
18. Vicentini JRT, Chang CY. MR imaging of the knee bursae and bursal pathology. Magn Reson Imaging Clin N Am. 2022;30(2):241-260. doi: 10.1016/j.mric.2022.01.004.
19. Abdelghany M, Abdelrazak A, Raafat M, Fattouh E. An unusually massive hemorrhagic superficial infrapatellar bursa excised in a one-stage procedure: case report. J Orthop Case Rep. 2023;13(8):142-146. doi:10.13107/jocr.2023.v13.i08.3850.
20. Naranje S, Mittal R, Kumar A, Nataraj AR. Hemorrhagic prepatellar bursitis: a rare case report and review of the literature. Eur J Orthop Surg Traumatol. 2009;19(4):281-284. doi: 10.1007/s00590-009-0428-8.
21. Telischak NA, Wu JS, Eisenberg RL. Cysts and cystic - appearing lesions of the knee: a pictorial essay. Indian J Radiol Imaging. 2014;24(2): 182-191. doi:10.4103/0971-3026.134413.
22. Rishor-Olney CR, Taqi M, Pozun A. Prepatellar Bursitis. In: StatPearls [Internet]. Treasure Island (FL): StatPearls Publishing; 2024 Jan 4. Available from: NCBI Bookshelf.
23. Luk WCB, Lui TH. Endoscopic resection of prepatellar bursa. Arthrosc Tech. 2020;9(7):e1057-e1060. doi: 10.1016/j.eats.2020.04.003.
24. Lormeau C, Cormier G, Sigaux J, Arvieux C, Semerano L. Management of septic bursitis. Joint Bone Spine. 2019;86(5):583-588. doi:10.1016/j.jbspin.2018.12.004.
25. Lin F, Yao J, Liu Y, Qi B. Prepatellar bursa mucosa: an unreported postoperative complication of patellar fracture. Medicine (Baltimore). 2024;103(45):e40445. doi: 10.1097/MD.0000000000040445.
26. Darrieutort-Laffite C, Coiffier G, Aïm F, Banal F, Bart G, Chazerain P, et al. 2023 French recommendations for diagnosing and managing prepatellar and olecranon septic bursitis. Joint Bone Spine. 2024;91(2):105664. doi:10.1016/j.jbspin.2023.105664.
27. Brown OS, Smith TO, Parsons T, Benjamin M, Hing CB. Management of septic and aseptic prepatellar bursitis: a systematic review. Arch Orthop Trauma Surg. 2022;142(10):2445-2457. doi:10.1007/s00402-021-03853-9.

Journal of the Mexican Federation
of Radiology and Imaging

TECHNICAL NOTE

Standardized structured breast CEM report based on BI-RADS v2025: a technical note

M. Joyce Torres-Navarro[1,2,a], *Carolina Dias-Rivero*[1,2,a], *David F. Perez-Montemayor*[1,2]** *and Karla G. Garcia-Alvarez*[3]

[1]Centro de Imagenologia Integral IMAX; [2]Instituto de Estudios Superiores de Tamaulipas, Universidad Anahuac; [3]Pathogen Pathology Laboratory, Hospital Beneficencia Española de Tampico. Tampico, Tamaulipas, Mexico

[a]These authors contributed equally.

ABSTRACT

The Breast Imaging Reporting and Data System (BI-RADS) lexicon standardizes the interpretation and reporting of breast findings to ensure clear, precise, and consistent communication between radiologists and referring physicians. Until its fifth edition, the BI-RADS system covered only digital mammography (DM), ultrasound (US), and magnetic resonance imaging (MRI). BI-RADS v2025 incorporates a specific lexicon for contrast-enhanced mammography (CEM), a technique that combines mammography with intravenous iodinated contrast media to evaluate lesion vascularity. Greater contrast enhancement improves the detection and characterization of suspicious lesions – especially in dense breasts – offering a faster, more accessible alternative to MRI in certain clinical scenarios. Although BI-RADS provides descriptors, categories, and standardized language for interpreting breast imaging findings, it lacks a structured reporting template for complete report writing. Therefore, the implementation of proprietary or institutional formats is necessary to ensure document uniformity and quality. In radiology, the use of structured templates significantly impacts the quality, efficiency, and safety of reports. They standardize language and report structure, reduce variability among radiologists, and decrease the possibility of omitting relevant findings. By following a predefined format, reports become more comprehensive and consistent, especially in frequent studies or those requiring systematic evaluation of multiple structures. This technical note provides a template for creating a structured and standardized report based on the BI-RADS v2025 lexicon to optimize diagnostic clarity, reproducibility of findings, and appropriate decision-making. It consists of eighteen sections, that includes general information, clinical history, most relevant previous studies, specific descriptors for abnormal findings, and the corresponding category and recommendations.

Keywords: *Mammography. Contrast media. Diagnostic imaging. Computerized medical records systems. Breast Imaging Reporting and Data System.*

INTRODUCTION

In Mexico, breast cancer is the most common malignant neoplasm in women, with an incidence of 30.6 cases per 100,000 women between the ages of 40 and 69[1] and is the leading cause of cancer-related mortality with high incidences in Sonora, Sinaloa, Tamaulipas, Coahuila, Baja California, Nuevo León, and Mexico City[2]. While digital mammography (DM) is the gold standard for screening, factors such as high breast density (C and D categories) can reduce sensitivity as low as 31.3%[3]. The implementation of new imaging

***Corresponding author:**
David F. Perez-Montemayor
E-mail: dfperez@prodigy.net.mx

Received for publication: 05-12-2025
Accepted for publication: 17-01-2026
DOI: 10.24875/JMEXFRI.M26000125

Available online: 16-04-2026
J Mex Fed Radiol Imaging. 2026;5(1):61-74
www.JMeXFRI.com

techniques, such as contrast-enhanced magnetic resonance imaging (CE-MRI) and contrast-enhanced mammography (CEM), helped increase the detection of lesions in women with this dense breasts, with sensitivity and specificity of 97% and 69% for CE-MRI and 95% and 78% for CEM, respectively[4,5]. Although CE-MRI has demonstrated greater sensitivity, factors such as accessibility and cost have led to CEM being increasingly used as an alternative for the detection and locoregional staging of breast cancer in women with dense breasts[3].

Since the Food and Drug Administration (FDA) approval in 2011, the use of CEM has increased, utilizing iodinated contrast media that allow visualize hypervascular areas resulting from tumor angiogenesis. It is based on the acquisition of low-energy (LE), high-energy (HE), and recombined (RC) images[6]. In 2022, the American College of Radiology (ACR) released a supplement to the ACR Breast Imaging Reporting and Data System (BI-RADS) mammography 2013 guidelines, which included the first version of the BI-RADS lexicon for CEM. In 2025, the section was formally established with the release of the first version of the chapter dedicated to CEM[7].

The structured radiology template is a practical tool to organizes information in a standardized, precise, efficient, and clinically relevant way. These features facilitate communication with referring physicians, improving the quality, clarity, and clinical utility of data. It also promotes the incorporation of quantitative measurements, the appropriate use of common terminology, and the reuse of information for research, quality management, and artificial intelligence[8]. This technical note introduces a structured, standardized template for reporting CEM breast findings based on BI-RADS v2025 lexicon.

THE IMPORTANCE OF STRUCTURED REPORTING

Standardized and organized language must be used to report breast findings. In radiology, reports are written as free-text prose or in standardized, structured formats that use templates[9]. Each format has its own characteristics; however, the standardized structured report stands out for its numerous advantages, including clarity, reduced use of acronyms, jargon, and circular reasoning, the ability to express the level of available evidence and the degree of accuracy and consistency of the information provided, and improved communication between radiologists and attending physicians[8].

A cross-sectional study in Mexico, including 71 (44.7%) radiologists and 88 (55.3%) attending physicians from various specialties with active clinical practice, assessed their preference for prose or standardized structured reports and identified the essential qualities of a radiology report. The study concluded that 74.6% of radiologists and 84.1% of attending physicians preferred the standardized structured report over a prose-written report, regardless of age, specialty, or professional experience. The most notable characteristics of this type of report were organization, comprehensibility, conciseness, readability, descriptiveness, and focus on the clinical context[9].

A standardized structured report facilitates interdisciplinary communication by systematically including the clinical indication, relevant findings, study quality, and recommendations for patient management, contributing to efficient and reliable decision-making[9]. Based on BI-RADS v2025, we developed a standardized, structured CEM report template. This report serves as a model that defines the minimum information and characteristics that must be included.

CEM INDICATIONS AND PROTOCOL

CEM is a vascular-based breast imaging method that uses iodinated contrast agents to depict angiogenesis. It may be considered for patients with contraindications to MRI. The main indications for CEM are asymptomatic screening, diagnostic work-up and diagnosis in current breast cancer[7]. The FDA has not approved CEM for screening; therefore, its use is off-label. This can be justified in patients with elevated risk, dense breasts, prior breast cancer with completed treatment, and cases where relevant history includes gene mutations, estimated cancer risk, or prior breast cancer.

For diagnostic work-up, CEM is indicated in patients with imaging findings or, follow-up in BI-RADS category 3, after biopsy, or for breast implant assessment. The clinical and imaging findings in these patients should be reported. If the indication is breast cancer diagnosis, CEM may be used to assess the extent of disease before treatment, and to evaluate response during or after neoadjuvant therapy. Before this examination, it is important to know the location and size of the malignant lesion on a previous imaging examination[7].

To perform CEM, informed consent must first be obtained. Antecubital venous access is established (preferably with a 20-gauge needle), and a non-ionic low-osmolar iodinated contrast agent (300-370 mg/mL) is administered at 1.5 mL/kg and a flow rate of 3 mL/s with a power injector, followed by a 10 mL saline bolus[10,11]. Two minutes after administration, standard bilateral craniocaudal (CC) and mediolateral oblique (MLO) views are obtained using dual-energy imaging, acquiring LE (28-32 keV) and HE (> 33.2 keV) images, which are recombined to suppress normal breast tissue and enhance lesion conspicuity[11,12]. HE imaging reveals contrast agent uptake, but it is non-interpretable. Additional views may be obtained as needed, within a maximum of 10 minutes after completion of the contrast injection and before contrast washout[12]. The injection site must be checked for any signs of contrast extravasation, which occurs in 0.1% to 1.2% of patients[11].

STANDARDIZED STRUCTURED TEMPLATE COMPONENTS FOR BREAST CEM REPORT

The standardized structured template, based on BI-RADS terminology and descriptors established by the ACR BI-RADS system[7] is organized into sections for systematic recording of clinical and radiological information obtained from the patient (Table 1 and Supplementary Table 1). The format begins with general information (date, time, and location of the study), followed by the patient's name, sex, age, weight, and referring physician. The first section includes the full name of the study to be performed. The second section specifies the indication: screening (indicating if the patient has a higher-than-average risk and the reason for the increased risk), diagnosis in patients under follow-up, in those with a finding or history of breast cancer under follow-up, or in those with histopathologic confirmation of breast cancer, to evaluate the extent of the disease or the response to neoadjuvant chemotherapy.

The third section details the patient's medical history, including a personal history with histopathology results, time frame, genetic studies, and/or family history of cancer. The fourth section includes relevant information from previous imaging examinations, specifying the date and type (DM, US, CEM, CE-MRI), and whether images and reports are available. If this is the patient's first CEM examination, it is described as a "baseline exam."

The fifth section describes the technique and protocol: laterality and projections acquired must be indicated, mentioning if projections other than the conventional CC and MLO were obtained, and the name of the contrast medium used, the dose (mmol/kg) and volume (cc). It is essential to include complications and reactions, and to describe in detail the symptoms and medical management during the CEM examination.

The sixth section should indicate the artifacts identified. The BI-RADS manual does not describe each of these in detail. Since they can reduce the quality of the CEM examination and lead to interpretation errors, they must be mentioned. Common artifacts, described by Jochelson et al.[6] and Lorente-Ramos et al.[13], are grouped into three categories:

- *Related to the contrast medium*: splatter of contrast material on the skin, detector, or compression paddles, which can simulate lesions or calcifications. The technician injecting the contrast agent should not be the person who positions the patient and should wear gloves, removing them before positioning the patient. Another preventive measure is to clean the breasts and the detector before image acquisition[6,13]. Another artifact is the transient retention of contrast material in veins, which may persist due to early breast compression; this usually resolves spontaneously. The distribution and morphology of these findings should be considered to determine if they are true[6,13].
- *Related to the technique*: air trapped in skin folds or scars due to improper contact can produce black lines in the image[6,13]; the halo artifact (also known as rim, breast-in-breast, or scattered radiation), when uneven thickness of breast tissue and skin produces different radiation scattering, can result in a double-breast contour; negative enhancement (the eclipse or crescent sign) produced by cysts, calcifications, and hematomas appears darker than the surrounding tissue; misregistration artifact is caused by patient movement with metal or calcium; when the paddles are the incorrect size, the axillary line becomes visible, causing horizontal lines to appear. Other artifacts, such as aborted acquisition, miscalibration, and ghosting, can be resolved through equipment calibration and new image acquisition[6,13].
- *Related to the patient*: movement during the acquisition of LE and HE images results in a mild RC mismatch with fine black-and-white lines or breast margin loss, potentially obscuring findings (ripple artifact)[6,13]. To avoid this, the technician should instruct the patient to hold their breath and maximize compression. Superimposed structures, such as the skin, anatomical features (breast, hair, shoulder, chin, nose, ear, clothing, or antiperspirant, can simulate calcifications. These must be recognized and a new projection acquired with the artifact out of the beam's path. Other artifacts include breast implants and cardiac devices[6,13].

Table 1. Standardized structured breast CEM report template based on BI-RADS v2025[7]

Description	Patient information
Study date, time, and location:	
Patient name:	
Sex (woman/man):	
Age (years):	
Weight (kg):	
Referring physician:	
1. Requested imaging examination.	
2. Indication: screening, diagnostic work-up, or current breast cancer.	
3. Medical history: family and/or personal history of breast cancer, with emphasis on genetic mutations and histopathology report.	
4. Comparison to previous examinations: specify if this is a "baseline exam," including dates and types of previous studies, and whether comparison is based on the report or images.	
5. Examination technique: indicate laterality (right, left, bilateral), views (CC, MLO), name of contrast agent, dosage (mmol/kg), volume (in cc), and presence or absence of complications or contrast reaction.	
6. Artifacts that may affect interpretation: - Contrast agent-related artifacts: contamination and/or transient retention of contrast material in veins. - Patient-related artifacts: ripple, breast implants, cardiac devices, and/or superimposed structures. - Technical artifacts: air trapping, skin-line, axillary line, halo, ghosting, misregistration, miscalibration, and/or aborted acquisition.	
7. General description of breast composition: - Breast density: (A) almost entirely fatty, (B) scattered areas of fibroglandular density, (C) heterogeneously dense, which may obscure small masses, (D) extremely dense, which lowers the sensitivity of mammography. - Background parenchymal enhancement: level (minimal, mild, moderate, or marked) and symmetry (symmetric or asymmetric).	
8. Description of findings on LE images only: based on the BI-RADS lexicon for digital mammography: - Masses: shape (oval, lobulated, round, or irregular), margin (circumscribed, obscured, indistinct, or spiculated), and density (fat-containing, low, equal, or high density). - Calcifications: typically, benign (skin, vascular, coarse, large rod-like, round, rim, layering, suture), suspicious morphology (amorphous, coarse, heterogeneous, fine pleomorphic, fine linear, or fine linear-branching), and distribution (diffuse, regional, grouped, linear, segmental). - Architectural distortion. - Asymmetries: global asymmetry, asymmetry, and/or focal asymmetry - Lymph nodes: intramammary and/or axillary. - Skin lesions. - Dilated ducts: multiple or solitary. - Associated features: skin retraction, nipple retraction, skin thickening, and/or trabecular thickening. - Special cases: gynecomastia, implants, other forms of augmentation, and/or mastectomy.	
9. Description of findings on RC images only: - Mass enhancement: shape (oval, lobulated, round, or irregular), margin (circumscribed or non-circumscribed: indistinct or spiculated), internal enhancement pattern (homogeneous, heterogeneous, or rim). - Non-mass enhancement: distribution (diffuse, regional, focal, linear, or segmental), internal enhancement pattern (homogeneous, heterogeneous, or clumped). - Enhancing asymmetry: internal enhancement pattern (homogeneous or heterogeneous).	

(Continued)

Table 1. Standardized structured breast CEM report template based on BI-RADS v2025[7] *(continuation)*

Description	Patient information
10. Description of findings on LE images with associated enhancement on RC images: - LE findings: as detailed in section 8. - Internal enhancement pattern: as detailed in section 9. - Extent of enhancement: mammographic lesion partially enhances, completely enhances, enhancement extends beyond the mammographic lesion, or no enhancement of the mammographic lesion but enhancement in adjacent tissue.	
11. Lesion conspicuity: describe the degree of BPE as low, moderate, or high.	
12. Associated features: nipple retraction, nipple involvement, skin retraction, skin thickening, skin involvement, and axillary adenopathy.	
13. Location of the suspicious finding: side, clock-face and/or quadrant, and depth (anterior, middle, or posterior third and/or distance from nipple in cm).	
14. Additional imaging: perform a targeted US and describe findings according to the BI-RADS lexicon (preferably report both CEM and US if done on the same day), including elasticity assessment by one of the two methods: - E/B ratio: < 1 = benign, and ≥ 1 = suspicious for malignancy. - 5-point color scale: 1 = soft throughout, 2 = mixed soft and hard, 3 = hard but smaller on elastography than B-mode, 4 = hard and equal in size on elastography and B-mode, 5 = hard and larger on elastography than B-mode.	
15. Conclusion: summarizes the main findings.	
16. BI-RADS: assessment categories and likelihood of cancer based on findings. - Category 0: incomplete: need additional imaging evaluation or need prior mammograms for comparison (N/A). - Category 1: negative (essentially 0% likelihood of malignancy). - Category 2: benign (essentially 0% likelihood of malignancy). - Category 3: probably benign (≥ 0% but ≤ 2% likelihood of malignancy). - Category 4: suspicious (> 2% but < 95% likelihood of malignancy). - Category 5: highly suggestive of malignancy (≥ 95% likelihood of malignancy). - Category 6: known biopsy-proven malignancy (N/A).	
17. Management recommendations: - Category 0: recall for additional imaging or need for comparison of prior examination(s). - Category 1: routine annual mammography. - Category 2: routine annual mammography. - Category 3: short interval (6-month) follow-up or continued surveillance (12-month). - Category 4: tissue diagnosis. - Category 5: tissue diagnosis. - Category 6: clinical follow-up with a surgeon and/or oncologist, and definitive local therapy (usually surgery) when clinically appropriate.	
18. Credentials of the radiologist who interpreted the CEM.	

CEM: contrast-enhanced mammography; BI-RADS: Breast Imaging Reporting and Data System; CC: craniocaudal; MLO: mediolateral oblique; LE: low energy; RC: recombined; BPE: background parenchymal enhancement; E/B: elastography to B mode length; N/A: not available; US: ultrasound.

The seventh section describes breast composition. According to the BI-RADS lexicon, breast density is classified as follows[7]: (A) the breasts are almost entirely fatty, (B) there are scattered areas of fibroglandular density, (C) the breasts are heterogeneously dense, which may obscure small masses, and (D) the breasts

Table 2. Example of a standardized structured CEM report template based on BI-RADS v2025[7] for a benign case (Figure 1)

Description	Patient information
Study date, time, and location:	December 15, 2025. Tampico, Tamaulipas.
Patient's name:	SRSC.
Sex (woman/man):	Woman.
Age (years):	45.
Weight (kg):	80.
Referring physician:	To whom it may concern.
1. Requested imaging examination.	Contrast-enhanced mammography.
2. Indication: screening, diagnostic work-up, or current breast cancer.	Screening.
3. Medical history: family and/or personal history of breast cancer, with emphasis on genetic mutations, and histopathology report.	No relevant family or personal history.
4. Comparison to previous examinations: a "baseline exam" may be specified, including the dates and type of previous studies, and whether it is based on the report or the images.	Comparison is made with reports of previous studies (mammography and ultrasound) from June 2023, which concluded dense breasts (D) and bilateral simple cysts, BI-RADS 2; as well as studies from May 2024 that concluded dense breasts (D), bilateral simple cysts, and multiple bilateral hyperdense masses, BI-RADS 0.
5. Examination technique: indicate the laterality (right, left, bilateral) and views (CC, MLO), name of the contrast agent, dosage (mmol/kg), and volume (cc), and the presence or absence of complications or contrast reaction.	Bilateral CEM with CC and MLO projections. Administration of non-ionic water-soluble contrast agent (omnipaque 300 mg/mL), 1.5 mL/kg, 120 cc. No adverse events after contrast agent administration.
6. Artifacts that may affect interpretation: - Contrast agent-related artifacts: contamination and/or transient retention of contrast material in veins. - Patient-related artifacts: ripple, breast implants, cardiac devices, and/or superimposed structures. - Technical artifacts: air trapping, skin-line, axillary line, halo, ghosting, misregistration, miscalibration, and/or aborted acquisition.	Bilateral halo artifact observed in both CC and MLO views, bilateral air trapping in MLO.
7. General description of breast composition: - Breast density: (A) the breasts are almost entirely fatty, (B) there are scattered areas of fibroglandular density, (C) the breasts are heterogeneously dense, which may obscure small masses, (D) the breasts are extremely dense, which reduces mammography sensitivity. - Background parenchymal enhancement: level (minimal, mild, moderate, or marked), and symmetry (symmetric or asymmetric).	The breast composition is extremely dense (D). Moderate and symmetric background parenchymal enhancement.
8. Description of findings on LE images only: based on the BI-RADS lexicon for digital mammography: - Masses: shape (oval, lobulated, round, or irregular), margin (circumscribed, obscured, indistinct, or spiculated), and density (fat-containing, low density, equal density, high density). - Calcifications: typically, benign (skin, vascular, coarse, large rod-like, round, rim, layering, suture), suspicious morphology (amorphous, coarse, heterogeneous, fine pleomorphic, fine linear, or fine linear-branching), and distribution (diffuse, regional, grouped, linear, segmental). - Architectural distortion. - Asymmetries: global asymmetry, asymmetry, and/or focal asymmetry. - Lymph nodes: intramammary, and/or axillary. - Skin lesions. - Dilated ducts: multiple or solitary. - Associated features: skin retraction, nipple retraction, skin thickening, and/or trabecular thickening. - Special cases: gynecomastia, implants, other forms of augmentation, and/or mastectomy.	See section 9.

(Continued)

Table 2. Example of a standardized structured CEM report template based on BI-RADS v2025[7] for a benign case (Figure 1) *(continuation)*

Description	Patient information
9. Description of findings on RC images only: - Mass enhancement: shape (oval, lobulated, round, or irregular), margin (circumscribed, or non-circumscribed: indistinct, or spiculated), internal enhancement pattern (homogeneous, heterogeneous, or rim). - Non-mass enhancement: distribution (diffuse, regional, focal, linear, or segmental), internal enhancement pattern (homogeneous, heterogeneous, or clumped). - Enhancing asymmetry: internal enhancement pattern (homogeneous or heterogeneous).	An oval, circumscribed, equal density mass is observed, presenting homogeneous internal enhancement.
10. Description of findings on LE images with associated enhancement on RC images: - LE findings: as detailed in section 8. - Internal enhancement pattern: as detailed in section 9. - Extent of enhancement: mammographic lesion partially enhances, mammographic lesion completely enhances, enhancement extends beyond mammographic lesion, or no enhancement of the mammographic lesion but enhancement in adjacent tissue.	See section 9.
11. Lesion conspicuity: describe the degree of BPE as low, moderate, or high.	Moderate lesion conspicuity.
12. Associated features: nipple retraction, nipple involvement, skin retraction, skin thickening, skin involvement, and axillary adenopathy.	None.
13. Location of finding: side, clock-face and/or quadrant, and depth (anterior, middle, or posterior third and/or distance from nipple in cm).	Right breast, lower quadrants interline, middle third, 2 cm from the nipple.
14. Additional imaging: perform a targeted US and describe the findings according to the BI-RADS lexicon (it is preferable to report both the CEM and the ultrasound if performed on the same day), including elasticity assessment by one of the two methods: - E/B ratio: < 1 = benign; and ≥ 1 = suspicious for malignancy. - 5-point color scale: 1 = soft throughout, 2 = mixed soft and hard, 3 = hard but smaller on elastography than B-mode, 4 = hard and equal in size on elastography and B-mode, 5 = hard and larger on elastography than B-mode.	Using GE LOGIQ E9 equipment, an oval, parallel, lobulated, hypoechoic mass without vascularity on color Doppler is observed, measuring 9 × 5 × 6 mm, located at 6 o'clock, 2 cm from the nipple of the right breast. Elastogram shows intermediate stiffness, with a 5-point color scale score of 2 (mixed soft and hard).
15. Conclusion: summarizes the main findings of the examination	Hyperenhancing mass in the right breast.
16. BI-RADS: assessment categories and likelihood of cancer based on findings. - Category 0: incomplete: need additional imaging evaluation or need prior mammograms for comparison (N/A). - Category 1: negative (essentially 0% likelihood of malignancy). - Category 2: benign (essentially 0% likelihood of malignancy). - Category 3: probably benign (≥ 0% but ≤ 2% likelihood of malignancy). - Category 4: suspicious (> 2% but < 95% likelihood of malignancy). - Category 5: highly suggestive of malignancy (≥ 95% likelihood of malignancy). - Category 6: known biopsy-proven malignancy (N/A).	Category BI-RADS 3: probably benign (≥ 0% but ≤ 2% likelihood of malignancy).
17. Management recommendations: - Category 0: recall for additional imaging/ need comparison of prior examination(s). - Category 1: routine annual mammography. - Category 2: routine annual mammography. - Category 3: short interval (6-month) follow-up or continued surveillance (12-month). - Category 4: tissue diagnosis. - Category 5: tissue diagnosis. - Category 6: clinical follow-up with surgeon and/or oncologist, and definitive local therapy (usually surgery) when clinically appropriate.	Short interval (6-month) follow-up is recommended.
18. Credentials of the radiologist who interpreted the CEM	

CEM: contrast-enhanced mammography; BI-RADS: Breast Imaging Reporting and Data System; CC: craniocaudal; MLO: mediolateral oblique; LE: low energy; RC: recombined; BPE: background parenchymal enhancement; E/B: elastography to B-mode length. N/A: not available; US: ultrasound.

are extremely dense, which lowers DM sensitivity. Subsequently, background parenchymal enhancement (BPE) is described according to the level – minimal, mild, moderate, or marked – and whether it is symmetric or asymmetric.

The eighth section describes LE image findings using the BI-RADS lexicon for DM. For masses, describe the shape (oval, lobulated, round, or irregular), margin (circumscribed, obscured, indistinct, or spiculated), and density (fat-containing, low density, equal density, or high density). For calcifications, classify them as typically benign (skin, vascular, coarse, large rod-like, round, rim, layering, or suture) or as having suspicious morphology (amorphous, coarse heterogeneous, fine pleomorphic, or fine linear/fine linear-branching). In both cases, indicate the distribution pattern (diffuse, regional, grouped, linear, or segmental). Also, architectural distortion and asymmetries, such as dilated ducts (multiple or solitary), are described. Special cases, such as gynecomastia, implants, other forms of augmentation, or mastectomy, must be included. The size and location of the finding, specifying laterality, quadrant, and/or clock face, depth, and/or distance from the nipple, should be mentioned.

The ninth section describes only RC image findings. It includes mass (shape, margin, internal enhancement pattern), non-mass enhancement (distribution, internal enhancement pattern), and enhancing asymmetry (internal enhancement pattern). The tenth section describes LE image findings with associated RC image enhancement. It requires a detailed description of morphology (oval, lobulated, round, or irregular), internal enhancement patterns (homogeneous, heterogeneous, or rim), and the extent of enhancement (mammographic lesion partially enhances, mammographic lesion completely enhances, enhancement extends beyond the mammographic lesion or no enhancement of the mammographic lesion but enhancement in adjacent tissue).

The eleventh section provides a subjective description of the degree of enhancement of the lesion compared to normal BPE: low, moderate, or high. If the lesion has enhancement similar to or slightly greater than the BPE, it is classified as low; if the enhancement is much greater than the BPE, it is classified as high; and if the enhancement falls between low and high, it is classified as moderate. The twelfth section describes associated features: retraction, involvement, or thickening of the skin and nipple. Axillary adenopathies are included.

The thirteenth section describes the location of suspicious malignant findings: laterality (right, left, or both) and the clock-face or quadrant. Lesion depth is indicated using thirds (anterior, middle, or posterior) along with the distance from the nipple in centimeters.

Section fourteen describes, if it is possible to perform, a targeted ultrasound (US) for CEM findings using BI-RADS v2025 descriptors for US[7]. Elastography is included in the lexicon because it is available on many US units. The descriptors for elasticity assessment are categorized as soft, intermediate, or hard. Two methods for stiffness assessment are recommended: the elastography-to-B-mode length (E/B) ratio and the 5-point color scale (elasticity score). For the E/B ratio, a value under 1 is associated with benign findings, while a ratio of 1 or higher is suspicious for malignancy. For the 5-point color scale, the assessment is as follows: 1 = soft throughout; 2 = mixed soft and hard; 3 = hard but smaller on elastography than on B-mode; 4 = hard and equal in size on elastography and B-mode; 5 = hard and larger on elastography than on B-mode. A score of 3 or lower on the 5-point color scale is more commonly associated with benign findings, while a score of 4 or 5 is considered suspicious for malignancy. For the strain ratio (lesion-to-fat ratio), a region of interest (ROI) is compared with subcutaneous fat. BI-RADS v2025 does not include formal recommendations for reporting strain elastography, which evaluates tissue stiffness based on how much a lesion can be compressed, or shear wave elastography, which measures the speed at which acoustically generated shear waves travel through tissue. Their cutoff values are not standardized and can vary by vendor or be configured by the user[7].

The fifteenth section is the conclusion, where relevant information from each CEM is summarized and ordered from most to least important. The sixteenth section describes the BI-RADS category based on the most relevant finding, benign or malignant, with assessment categories and likelihood of cancer: Category 0: incomplete; Category 1: negative; Category 2: benign; Category 3: probably benign; Category 4: suspicious; Category 5: highly suggestive of malignancy; and Category 6: known biopsy-proven malignancy[7].

The seventeenth section contains management recommendations based on the assigned BI-RADS category: Category 0: recall for additional imaging or need comparison to prior examinations; Category 1: routine annual mammography; Category 2: routine annual mammography; Category 3: short-interval (6-month) follow-up or continued surveillance (12-month); Category 4: tissue diagnosis; Category 5: tissue diagnosis; Category 6: clinical follow-up with a surgeon and/or oncologist, and

Table 3. Example of a standardized structured CEM report template based on BI-RADS v2025[7] for a malignant case (Figure 2)

Description	Patient information
Study date, time, and location:	December 18, 2025. Tampico, Tamaulipas.
Patient name:	MAPG.
Sex (woman/man):	Woman.
Age (years):	72.
Weight (kg):	65.
Referring physician:	To whom it may concern.
1. Requested imaging examination.	Contrast-enhanced mammography.
2. Indication: screening, diagnostic work-up, or current breast cancer.	Diagnostic.
3. Medical history: family and/or personal history of breast cancer, with emphasis on genetic mutations, and histopathology report.	No relevant family or personal history.
4. Comparison to previous examinations: a "baseline exam" may be specified, including the dates and type of previous studies, and whether it is based on the report or the images.	Based on a report of a previous mammogram performed at another institution in October 2025, a focal asymmetry with thick, heterogeneous, and segmental calcifications was identified in the left breast, categorized as BI-RADS 4B.
5. Examination technique: indicate the laterality (right, left, bilateral) and views (CC, MLO), name of the contrast agent, dose (mmol/kg), volume (cc), and the presence or absence of complications/contrast reaction.	Bilateral CEM with CC and MLO projections. Administration of non-ionic water-soluble contrast agent (Omnipaque 300 mg I/mL), 1.5 ml/kg, 97 cc. No adverse events were reported during or after contrast agent administration.
6. Artifacts that may affect interpretation: - Contrast agent-related artifacts: contamination and/or transient retention of contrast material in veins. - Patient-related artifacts: ripple, breast implants, cardiac devices, and/or superimposed structures. - Technical artifacts: air trapping, skin-line, axillary line, halo, ghosting, misregistration, miscalibration, and/or aborted acquisition.	Air trapping and halo artifact are observed in both breasts, with a misregistration artifact due to calcifications in the left breast seen in CC and MLO views.
7. General description of breast composition: - Breast density: (A) the breasts are almost entirely fatty, (B) there are scattered areas of fibroglandular density, (C) the breasts are heterogeneously dense, which may obscure small masses, (D) the breasts are extremely dense, which reduces mammography sensitivity. - Background parenchymal enhancement: level (minimal, mild, moderate, or marked), and symmetry (symmetric or asymmetric).	The breast composition shows scattered areas of fibroglandular density (B). Minimal and symmetric background parenchymal enhancement.
8. Description of findings on LE images only: based on the BI-RADS lexicon for digital mammography: - Masses: shape (oval, lobulated, round, or irregular), margin (circumscribed, obscured, indistinct, or spiculated), and density (fat-containing, low density, equal density, high density). - Calcifications: typically, benign (skin, vascular, coarse, large rod-like, round, rim, layering, suture), suspicious morphology (amorphous, coarse, heterogeneous, fine pleomorphic, fine linear, or fine linear-branching), and distribution (diffuse, regional, grouped, linear, segmental). - Architectural distortion. - Asymmetries: global asymmetry, asymmetry, and/or focal asymmetry. - Lymph nodes: intramammary and/or axillary. - Skin lesions. - Dilated ducts: multiple or solitary. - Associated features: skin retraction, nipple retraction, skin thickening, and/or trabecular thickening. - Special cases: gynecomastia, implants, other forms of augmentation, and/or mastectomy.	See section 10.

(Continued)

Table 3. Example of a standardized structured CEM report template based on BI-RADS v2025[7] for a malignant case (Figure 2) *(continuation)*

Description	Patient information
9. Description of findings on RC images only: - Mass enhancement: shape (oval, lobulated, round, or irregular), margin (circumscribed, or non-circumscribed: indistinct, or spiculated), internal enhancement pattern (homogeneous, heterogeneous, or rim). - Non-mass enhancement: distribution (diffuse, regional, focal, linear, or segmental), internal enhancement pattern (homogeneous, heterogeneous, or clumped). - Enhancing asymmetry: internal enhancement pattern (homogeneous or heterogeneous).	See section 10.
10. Description of findings on LE images with associated enhancement on RC images: - LE findings: as detailed in section 8. - Internal enhancement pattern: as detailed in section 9. - Extent of enhancement: the mammographic lesion partially enhances, mammographic lesion completely enhances, enhancement extends beyond mammographic lesion, or no enhancement of the mammographic lesion but enhancement in adjacent tissue.	In LE images, asymmetry is observed in the CC projection, associated with round and linear segmental calcifications. In the RC images, at the site of the asymmetry observed in the LE image, a non-mass enhancement is noted, characterized by a segmental distribution and a clumped internal enhancement pattern.
11. Lesion conspicuity: describe the degree of BPE as low, moderate, or high.	Moderate lesion conspicuity.
12. Associated features: nipple retraction, nipple involvement, skin retraction, skin thickening, skin involvement, and axillary adenopathy.	None.
13. Location of finding: side, clock-face and/or quadrant, and depth (anterior, middle, or posterior third and/or distance from nipple in cm).	Left breast, outer upper quadrant, anterior third, 4 cm from the nipple.
14. Additional imaging: perform a targeted US and describe findings according to the BI-RADS lexicon (preferably report both CEM and US if done on the same day), including elasticity assessment by one of the two methods: - E/B ratio: < 1= benign; and ≥ 1 = suspicious for malignancy. - 5-point color scale: 1 = soft throughout, 2 = mixed soft and hard, 3 = hard but smaller on elastography than B-mode, 4 = hard and equal in size on elastography and B-mode, 5 = hard and larger on elastography than B-mode.	Using GE LOGIQ E9 equipment a non-mass lesion with calcifications, posterior shadowing, and internal vascularity on color Doppler is observed, measuring 21 × 21 mm, located in the outer upper quadrant of the left breast. Elastogram shows a hard pattern; the 5-point color scale score is 5 (hard and larger on elastography than B-mode).
15. Conclusion: summarizes the main findings of the examination.	Asymmetry associated with non-mass enhancement with round and linear segmental calcifications in the outer upper quadrant of the left breast.
16. BI-RADS: assessment categories and likelihood of cancer based on findings. - Category 0: incomplete: need additional imaging evaluation or need prior mammograms for comparison (N/A). - Category 1: negative (essentially 0% likelihood of malignancy). - Category 2: benign (essentially 0% likelihood of malignancy). - Category 3: probably benign (≥ 0% but ≤ 2% likelihood of malignancy). - Category 4: suspicious (> 2% but < 95% likelihood of malignancy). - Category 5: highly suggestive of malignancy (≥ 95% likelihood of malignancy). - Category 6: known biopsy-proven malignancy (N/A).	Category BI-RADS 4: suspicious (> 2% but < 95% likelihood of malignancy).
17. Management recommendations: - Category 0: recall for additional imaging/ need comparison of prior examination(s). - Category 1: routine annual mammography. - Category 2: routine annual mammography. - Category 3: short interval (6-month) follow-up or continued surveillance (12-month). - Category 4: tissue diagnosis. - Category 5: tissue diagnosis. - Category 6: clinical follow-up with surgeon and/or oncologist, and definitive local therapy (usually surgery) when clinically appropriate.	Tissue diagnosis is recommended.
18. Credentials of the radiologist who interpreted the CEM.	

CEM: contrast-enhanced mammography; BI-RADS: Breast Imaging Reporting and Data System; CC: craniocaudal; MLO: mediolateral oblique; LE: low energy; RC: recombined; BPE: background parenchymal enhancement; E/B: elastography to B-mode length; N/A: not available; US: ultrasound.

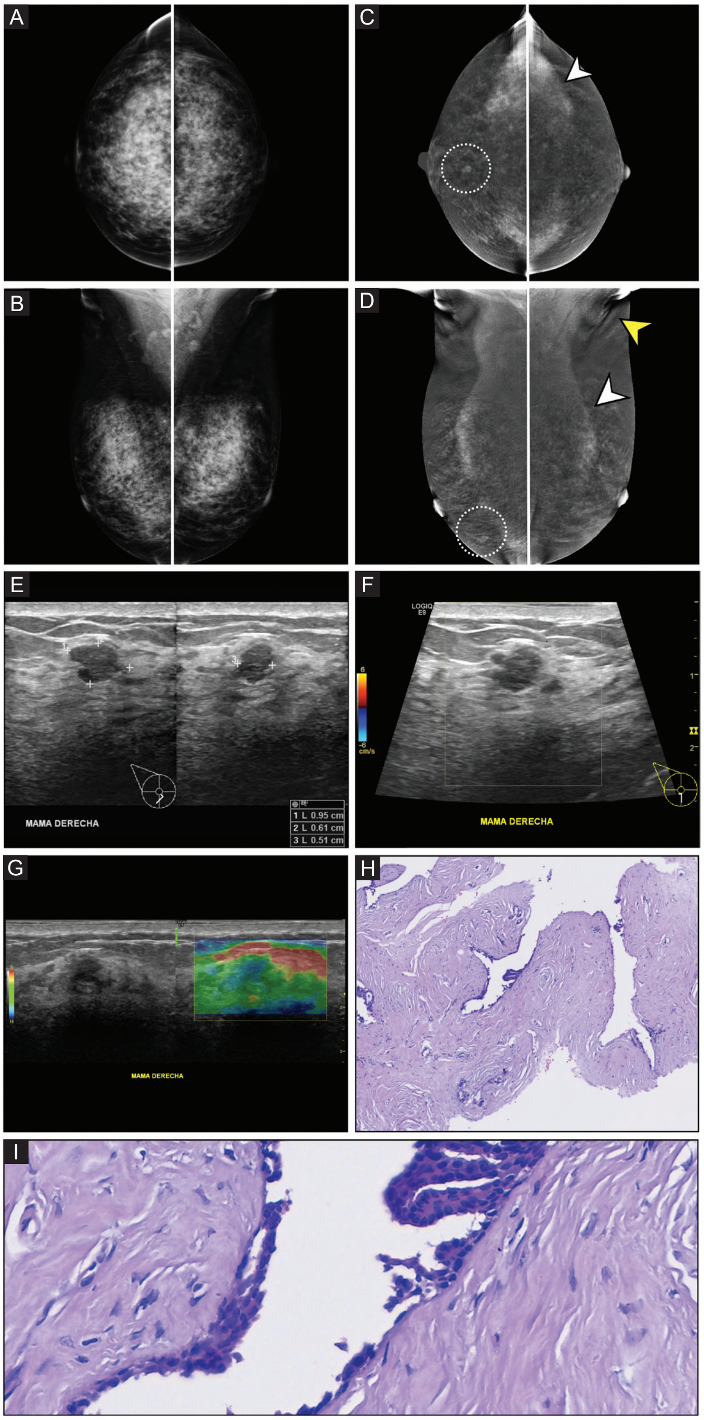

Figure 1. CEM of a 45-year-old asymptomatic woman who underwent screening due to high breast density. A hyperenhancing mass was found in the right breast, resulting in a BI-RADS category 3. **A-B**: CC and MLO LE views show an extremely dense breast (D), with no abnormalities. **C-D**: CC and MLO RC views show bilateral halo artifact (white arrowhead) and air trapping (yellow arrowhead), with moderate and symmetric background parenchymal enhancement. An oval, circumscribed, equal-density mass is observed, presenting homogeneous internal enhancement, and moderate lesion conspicuity, located in the right breast, lower quadrants interline, middle third, 2 cm from the nipple (white dotted circle). **E-F**: grayscale US shows an oval, parallel, lobulated, hypoechoic mass, without vascularity on color Doppler, measuring 9 × 5 × 6 mm, located at 6 o'clock, 2 cm from the nipple of the right breast. **G**: elastogram shows intermediate stiffness, with a 5-point color scale score of 2 (mixed soft and hard). BI-RADS category 3: probably benign. An US-guided biopsy was performed at the request of the attending physician. **H**: histopathologic panoramic view (H&E, 4×) of a fibroepithelial lesion with predominance of the mesenchymal component, consisting of fibroblasts and abundant extracellular matrix. **I**: at higher magnification (H&E, 40×), the epithelial component appears compressed and displaced by the fibrous stroma, lined with columnar cells without evident cytological atypia. The histopathologic diagnosis was fibroadenoma.

CEM: contrast-enhanced mammography; CC: craniocaudal; MLO: mediolateral oblique; LE: low energy; RC: recombined; US: ultrasound; BI-RADS: Breast Imaging Reporting and Data System; H&E: hematoxylin and eosin.

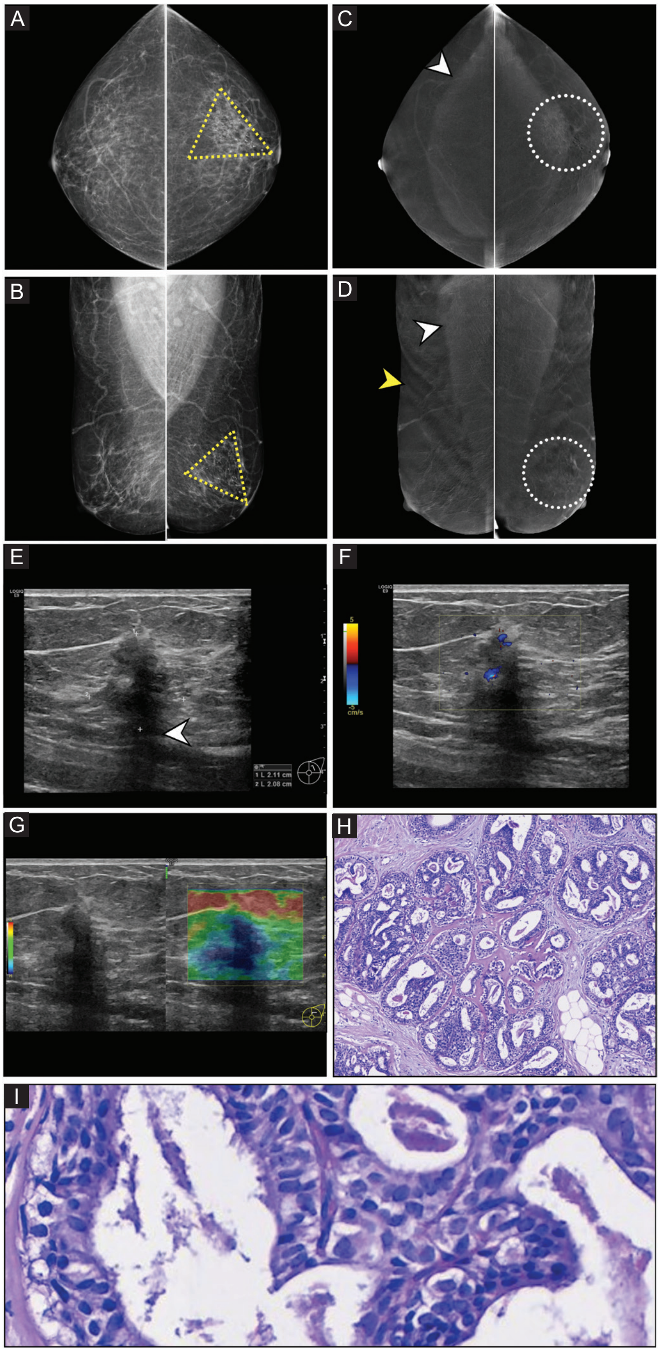

Figure 2. A 72-year-old woman who underwent diagnostic evaluation based on a previous mammography and US with a BI-RADS 4B category. **A-B:** CC and MLO LE views show breast tissue with scattered areas of fibroglandular density (B). Asymmetry is observed in the outer upper quadrants of the left breast, associated with round and linear segmental calcifications (yellow dotted triangle). **C-D:** CC and MLO RC views reveal bilateral air trapping (yellow arrowhead) and halo artifacts (white arrowhead), with minimal and symmetric background parenchymal enhancement. There is non-mass enhancement associated with calcifications (misregistration artifact) in a segmental distribution, and a clumped internal enhancement pattern with moderate lesion conspicuity, located in the left breast, outer upper quadrant, anterior third, 4 cm from the nipple (white dotted circle), corresponding to the asymmetry described in LE. **E:** targeted US using a GE LOGIQ E9 shows a non-mass lesion with calcifications and posterior shadowing (white arrowhead), measuring 21 × 21 mm, located in the outer upper quadrant of the left breast. **F:** color Doppler US shows vascularity within the non-mass lesion. **G:** elastogram shows a hard pattern; the 5-point color scale score is 5 (hard and larger on elastography than B-mode). Assessment category BI-RADS 4: suspicious. US-guided biopsy was performed. **H:** panoramic histopathology view (H&E 4×) shows glandular proliferation with a cribriform and papillary growth pattern, with no evidence of basement membrane rupture. **I:** at higher magnification (H&E 40×), the glands are lined by columnar epithelium with nuclear pleomorphism; elongated and hyperchromatic nuclei are observed, with the basement membrane remains intact. The histopathologic diagnosis was ductal carcinoma in situ.

CEM: contrast-enhanced mammography; CC: craniocaudal; MLO: mediolateral oblique; LE: low energy; RC: recombined; US: ultrasound; BI-RADS: Breast Imaging Reporting and Data System; H&E: hematoxylin and eosin.

definitive local therapy (usually surgery) when clinically appropriate[7]. The eighteenth section, which concludes the report, includes the radiologist's information: name, professional license number, and signature.

Table 2 presents a template example for reporting CEM examination of a benign clinical case involving a 45-year-old asymptomatic woman who underwent screening due to high breast density (D). A hyperenhancing mass was found in the right breast, BI-RADS category 3 (Figure 1). A US-guided biopsy was performed at the physician's request. The histopathologic diagnosis was benign fibroadenoma.

Table 3 presents a template example with the description of the structured and standardized CEM report of a malignant clinical case involving a 72-year-old woman who underwent diagnostic evaluation based on a previous mammography and US with BI-RADS category 4B (Figure 2). Asymmetry associated with non-mass enhancement and round and linear segmental calcifications was found in the left breast. US-guided biopsy was performed. The histopathologic diagnosis was ductal carcinoma in situ.

CONCLUSION

Based on the BI-RADS v2025 update, this technical note presents a structured template for standardized, systematic CEM reporting. The use of templates significantly impacts radiology and other medical specialties by changing how patients' clinical data are documented, communicated, and analyzed. However, excessive and mechanical use of templates should be avoided, as it can limit individual judgment, reduce the medical narrative, or generate repetitive documentation without critical analysis. To prevent this, templates should be flexible, allow supplementary free text, and be based on the specialty's needs. For radiologists, templates have transformed report preparation by organizing findings, reducing omissions, stratifying risk, and improving the quality of conclusions, enabling optimal clinical management for each patient. They also reduce variability among professionals, improve communication with attending physicians, and strengthen the medicolegal framework. Structuring data facilitates clinical research and the development of artificial intelligence. The impact is similar for clinical and surgical specialists, though with its own nuances. Templates ensure that relevant elements are documented. They also serve as checklists that reduce errors and omissions and facilitate follow-up. In the complex hospital environment, standardization facilitates interdisciplinary communication and reduces ambiguity. It increases efficiency by reducing writing time, streamlining workflows, and maintaining quality, even in high-volume patient scenarios.

Acknowledgments

The authors thank Professor Ana M. Contreras-Navarro for her guidance in preparing and writing this scientific paper.

Funding

The authors declare that they have not received funding.

Conflicts of interest

The authors declare no conflicts of interest.

Ethical considerations

Protection of human subjects and animals. The authors declare that the procedures followed were in accordance with the ethical standards of the responsible committee on human experimentation and with the World Medical Association and the Declaration of Helsinki. The procedures were authorized by the Institutional Ethics Committee.

Confidentiality, informed consent, and ethical approval. The authors have obtained approval from the Ethics Committee for the analysis of routinely collected and anonymized clinical data; therefore, individual informed consent was not required. Relevant ethical recommendations have been followed.

Declaration on the use of artificial intelligence. The authors declare that no generative artificial intelligence was used in the writing or creation of the content of this manuscript.

Supplementary data

One supplementary template is available on the Journal of the Mexican Federation of Radiology and Imaging website (DOI: 10.24875/JMEXFRI.M26000125). This template is provided by the corresponding author and published online for the reader's benefit.

REFERENCES

1. Instituto Nacional de Estadística y Geografía (INEGI). Mortalidad por cáncer de mama en mujeres en México 2024. Ciudad de México: INEGI; 2025.

2. Arceo-Martínez MT, López-Meza JE, Ochoa-Zarzosa A, Palomera-Sánchez Z. Estado actual del cáncer de mama en México: principales tipos y factores de riesgo. Gac Mex Oncol. 2021;20(3):101-110. doi: 10.24875/j.gamo.21000134.
3. Brown AL, Vijapura C, Patel M, De La Cruz A, Wahab R. Breast cancer in dense breasts: detection challenges and supplemental screening opportunities. Radiographics. 2023;43(10):e230024. doi: 10.1148/rg.230024.
4. Pötsch N, Vatteroni G, Clauser P, Helbich TH, Baltzer PAT. Contrast-enhanced mammography versus contrast-enhanced breast MRI: a systematic review and meta-analysis. Radiology. 2022;305(1):94-103. doi: 10.1148/radiol.212530.
5. Cozzi A, Magni V, Zanardo M, Schiaffino S, Sardanelli F. Contrast-enhanced mammography: a systematic review and meta-analysis of diagnostic performance. Radiology. 2022;302(3):568-581. doi: 10.1148/radiol.211412.
6. Jochelson MS, Lobbes MBI. Contrast-enhanced mammography: state of the art. Radiology. 2021;299(1):36-48. doi: 10.1148/radiol.2021201948.
7. Newell MS, Destounis SV, Leung JWT, DeMartini WB, Lee CH, Eby PR, et al. ACR BI-RADS® v2025 Manual. Reston, VA. USA: American College of Radiology; 2025.
8. Marti-Bonmati L. The importance of a structured radiological report. J Mex Fed Radiol Imaging. 2023;2(1):1-3. doi: 10.24875/JMEXFRI.M23000036.
9. Garcia-Moreno C, Jimenez-De La O ER, Herrera-Sanchez A. Mexican radiologists' and referring clinicians' preference for a standardized structured radiology report: qualities and content. J Mex Fed Radiol Imaging. 2022;1(1):13-22. doi: 10.24875/JMEXFRI.M21000001.
10. Coffey K, Jochelson MS. Contrast-enhanced mammography in breast cancer screening. Eur J Radiol. 2022;156:110513. doi: 10.1016/j.ejrad.2022.110513.
11. Alsheik N, Gabriel R, Nicholson Brandi T. Contrast Enhanced Mammography Implementation Guide. Hologic® Global Medical Education. 2021 Mar1. www.HologicED.com.
12. Ghaderi KF, Phillips J, Perry H, Lotfi P, Mehta TS. Contrast-enhanced mammography: current applications and future directions. Radiographics. 2019;39(7):1907-1920. doi: 10.1148/rg.2019190079.
13. Lorente-Ramos RM, Azpeitia-Armán J, Oliva-Fonte C, Pérez-Bartolomé A, Azpeitia Hernández J. Contrast-enhanced mammography artifacts and pitfalls: tips and tricks to avoid misinterpretation. Radiographics. 2023;43(10):e230021. doi: 10.1148/rg.230021.

JMeXFRI

Journal of the Mexican Federation
of Radiology and Imaging

CASE REPORT

High-resolution MSK-US findings of a reversed palmaris longus muscle causing a painful mass with neurosensitive symptoms: a case report

Jorge Mora-Constantino[1], Esteban Barbosa-Peña[2], Victor M. Pulido-Cheverria[2]
and Roberto Hernandez-Juarez[3,4]*

[1]Department of Radiology and Imaging, CADEM del Moral, Laboratorios Chopo; [2]Department of Radiology and Imaging, Specialty Hospital Num.1, Centro Medico Nacional del Bajio, Instituto Mexicano del Seguro Social. Leon, Guanajuato; [3]Department of Radiology and Imaging, Hospital Angeles Pedregal; [4]Facultad de Medicina, Division de Posgrados, Universidad Nacional Autonoma de Mexico. Mexico City. Mexico

ABSTRACT

The reversed palmaris longus muscle (RPLM) is an uncommon anatomical variant that can mimic a space-occupying lesion of the forearm. We present the case of a 13-year-old boy, a competitive martial arts, with a painful mass in the right forearm. A high-resolution musculoskeletal ultrasound (MSK-US) exhibited an ovoid muscle structure, isoechoic to adjacent muscles, with a typical fibrillar pattern, anomalously located in the distal third of the right forearm. The RPLM showed an inverted morphology, with a distal muscle belly and a proximal tendon. This anatomical variant is positioned adjacent to the median nerve (MN), resulting in local compression. Real-time dynamic MSK-US demonstrated thinning of the muscle belly during active contraction. Color and power Doppler US showed normal intrinsic vascularity and excluded neoplastic or inflammatory processes. A contralateral examination showed a normal palmaris longus tendon in the left forearm. An anterior right forearm RPLM was diagnosed by MSK-US. Management was conservative, focusing on patient education, physical therapy emphasizing stretching and strengthening, and a temporary reduction in martial arts practice intensity. This case report provides a detailed description of an RPLM diagnosed by MSK-US, highlighting its utility as a dynamic, accessible, and high-resolution tool.

Keywords: *Reversed palmaris longus muscle. Musculoskeletal ultrasound. Median nerve. Anatomical variants. Nerve entrapment syndrome. Case report.*

INTRODUCTION

The palmaris longus muscle (PLM) is a superficial structure in the anterior forearm. Its marked morphological variability makes it a subject of significant clinical interest[1]. Although its biomechanical role as a weak accessory wrist flexor is often considered dispensable, its high variability makes it a fundamental muscle in the differential diagnosis of upper extremity masses[2]. One of the rarest and most pathologically significant variant is the reversed palmaris longus muscle (RPLM), in which its classic structure –a proximal muscle belly and a distal tendon– is inverted, with the fleshy muscle belly in the distal third and the tendon in the upper third of the anterior forearm[3,4]. Clinically, RPLM may be asymptomatic or present as a localized soft mass, with pain, swelling, and neurovascular compression primarily affecting the median nerve (MN)[4,5].

RPLM is usually identified by magnetic resonance imaging (MRI) or intraoperatively during nerve entrapment exploration[6,7]. The features of RPLM using musculoskeletal ultrasound (MSK-US) have been scarcely documented[8,9]. In this case report, we describe a rare, symptomatic case of RPLM diagnosed by high-resolution MSK-US in a pediatric patient.

***Corresponding author:**
Jorge Mora-Constantino
E-mail: moratony57@gmail.com

Received for publication: 11-06-2025
Accepted for publication: 13-01-2026
DOI: 10.24875/JMEXFRI.25000015

Available online: 16-04-2026
J Mex Fed Radiol Imaging. 2026;5(1):75-80
www.JMeXFRI.com

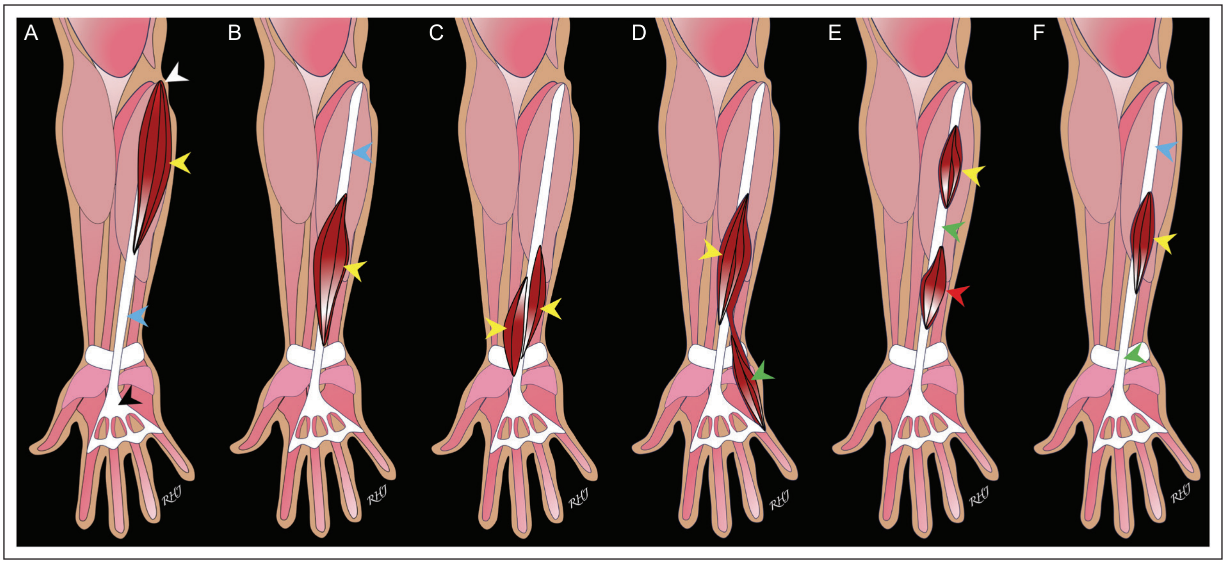

Figure 1. Illustrations of PLM anatomical variants based on muscle belly morphology and tendon arrangement. **A:** normal PLM with the typical appearance of a proximal fusiform muscle belly (yellow arrowhead) originating from the medial epicondyle (white arrowhead) and a palmaris longus tendon (blue arrowhead) inserting on the palmar aponeurosis (black arrowhead). **B:** RPLM with an inverse configuration with a proximal tendinous component (blue arrowhead) and a muscle belly in the distal third of the forearm (yellow arrowhead). **C:** bifid RPLM, reversed variant with a duplication or cleft of the muscle belly in its distal segment (yellow arrowheads). **D:** a RPLM coexisting with the ADMM (yellow arrowhead) associated with an accessory belly or a myofascial slip connecting to the ADMM (green arrowhead). **E:** digastric PLM configuration with two distinct muscle bellies: a proximal belly (yellow arrowhead) and a distal belly (red arrowhead), joined by an intermediate tendon (green arrowhead). **F:** PLM with an intermediate muscle belly with the muscular portion in the middle third of the forearm (yellow arrowhead), bounded by proximal (blue arrowhead) and distal (green arrowhead) tendinous segments.

PLM: palmaris longus muscle; RPLM: reversed palmaris longus muscle; ADMM: abductor digiti minimi muscle.

CLINICAL CASE DESCRIPTION

A 13-year-old boy presented with a painful palpable mass in the right distal forearm. He was a martial arts practitioner with no relevant medical or surgical history. Symptoms began insidiously two months before with intermittent pain during martial arts training, accompanied by mild paresthesia in the MN distribution. Physical examination revealed a soft, mobile, non-tender mass on the volar aspect of the right forearm, approximately 5 cm proximal to the wrist crease. The Tinel and Phalen nerve provocation tests were negative or inconclusive at rest. A broad spectrum of differential diagnoses was considered, including anatomical variants of the PLM, such as the RPLM, bifid RPLM, and RPLM coexisting with the abductor digiti minimi (ADMM) (Figure 1).

Imaging findings

Real-time MSK-US was performed using a LOGIQ S8 system (GE Healthcare, Chicago, IL, USA) with a high-frequency linear transducer (11 MHz), focused on the anterior forearm compartment. The patient was seated, with the right upper limb semi-flexed and fully supinated on a stable surface. Conductive gel was applied to the distal anterior forearm, approximately 4-6 cm proximal to the wrist crease. Transverse and longitudinal planes were systematically scanned (Figure 2). Initial transverse imaging identified the PLM, the flexor carpi radialis muscle (FCRM), the flexor digitorum superficialis muscle (FDSM) tendons, and the MN. A fusiform, hypoechoic, mild fibrillar, muscular structure – with an echotexture similar to adjacent muscles – was noted along the course of the MN, resulting in nerve compression.

Longitudinal imaging confirmed a distal muscle belly and a proximal tendon – typical of the reversed variant. Color and power Doppler US showed normal vascularization, with no signs of inflammation or pathological neovascularization (Figure 3). Contralateral examination showed a normal palmaris longus tendon in the left forearm (Figure 4). The muscle was adjacent to the MN without dynamic entrapment. A RPLM in the anterior right forearm was diagnosed by MSK-US.

Clinical outcome

Conservative management consisted of patient education about the anatomical variant, physical therapy emphasizing muscle stretching and strengthening,

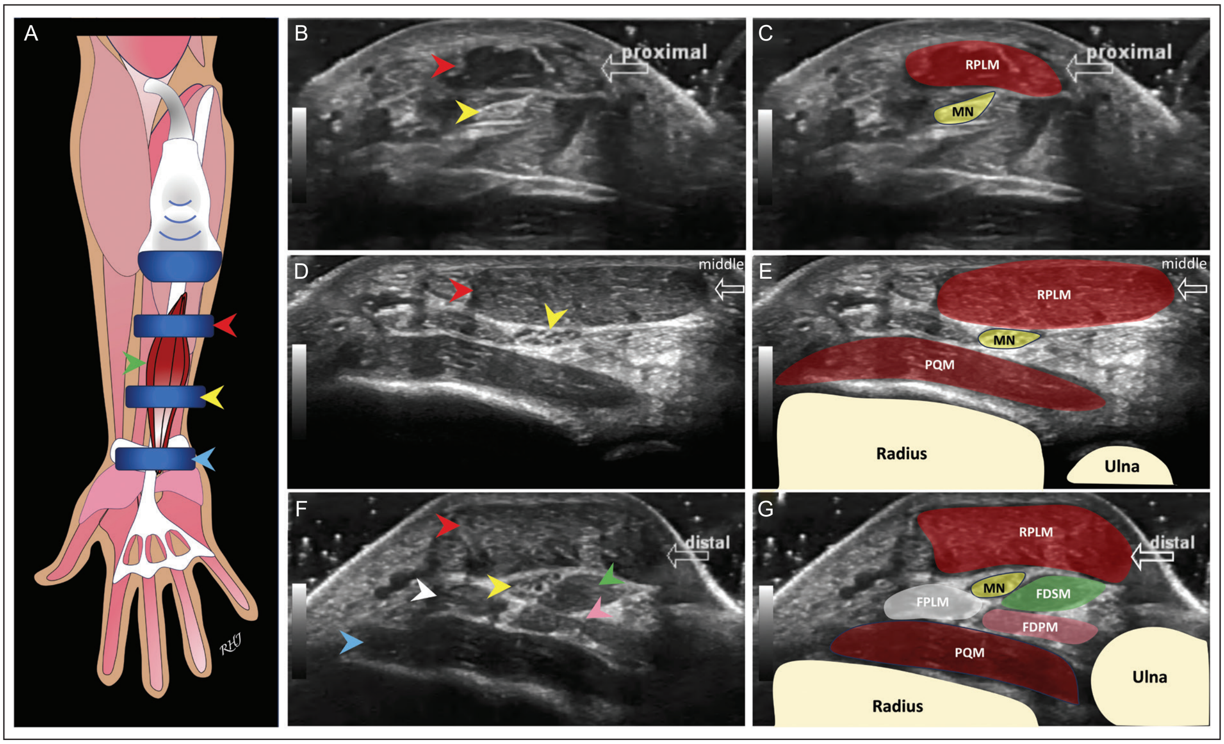

Figure 2. A 13-year-old boy with a painful palpable mass in the right distal forearm diagnosed with RPLM. **A:** illustration of the MSK-US approach to the pronated forearm, tracing the RPLM (green arrow) along its proximal (red arrowhead), middle (yellow arrowhead), and distal (blue arrowhead) segments. **B-C:** grayscale MSK-US transverse view shows the RPLM at the proximal segment (void arrow); a fusiform, hypoechoic, mildly fibrillar structure is seen, with an echoic texture similar to adjacent muscles (red arrowhead), in direct relation to the MN (yellow arrowhead). **D-E:** grayscale MSK-US transverse view shows the RPLM (red arrowhead) in the middle segment (void arrow) exerting mild compression on the MN (yellow arrowhead). **F-G:** grayscale MSK-US transverse view of the RPLM (red arrowhead) at the distal segment (void arrow) with mild compression of the MN (yellow arrowhead); the FPLM (white arrowhead), FDSM (green arrowhead), FDPM (pink arrowhead), and PQM (blue arrowhead) exhibit preserved morphology.

RPLM: reversed palmaris longus muscle; MN: median nerve; FPLM: flexor pollicis longus muscle; FDSM: flexor digitorum superficialis muscle; FDPM: flexor digitorum profundus muscle; PQM: pronator quadratus muscle; MSK-US: musculoskeletal ultrasound.

and a temporary reduction of sport intensity. Clinical follow-up at 3 months had a favorable outcome, with the patient reporting complete resolution of pain and paresthesia.

DISCUSSION

This case report describes a symptomatic RPLM diagnosed with high-resolution MSK-US in a pediatric patient with a painful palpable mass in the right distal forearm. MSK-US provided a precise characterization of the anomalous muscle, an evaluation of its relationship with the MN, and the diagnosis of RPLM. This report highlights the expanding role of MSK-US in characterizing forearm anatomy and its value in the differential diagnosis of soft tissue masses.

Anatomically, the RPLM is part of the broad spectrum of PLM variants, ranging from congenital absence to duplications and aberrant insertions[10,11]. MRI has been the standard diagnostic tool, but it has limitations in differentiating muscle planes and identifying muscle isointensity[6]. Schuurman et al.[6] reported four patients – three women aged 18, 24, and 51, and a 22-year-old man – with effort-related MN compression due to RPLM diagnosed by wrist MRI. Despite its resolution, MRI remains vulnerable to tissue mimicry, as the RPLM is isointense to the surrounding muscles. In contrast to MRI, which provides a static anatomical depiction, MSK-US allows dynamic characterization of the RPLM, while MRI faces intrinsic difficulties in differentiating individual muscle planes and may misidentify the variant as other flexors or expansive processes due to its isointense signal. MSK-US facilitates continuous tracking of the tendinous axis and real-time assessment of mechanical interaction with the MN. In our case report, MSK-US revealed an ovoid muscular structure, isoechoic relative to adjacent muscles, with a typical fibrillar pattern, anomalously located in the distal third

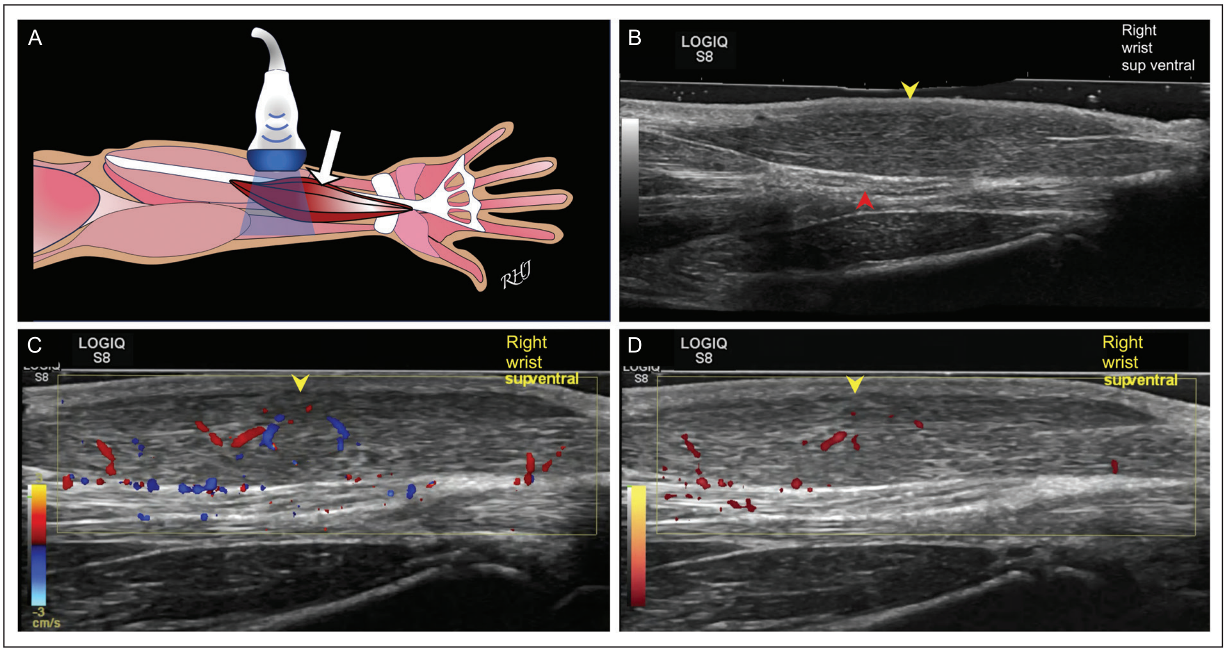

Figure 3. A 13-year-old boy with a painful palpable mass in the right distal forearm diagnosed with RPLM. **A:** illustration of the MSK-US approach to the pronated forearm, tracing the course of the RPLM (white arrow). **B:** extended field-of-view grayscale MSK-US showing the RPLM (yellow arrowhead) positioned over the MN, exerting compression (red arrowhead). **C:** longitudinal view and color Doppler MSK-US, and **D:** power Doppler view of the RPLM (yellow arrowhead) with normal vascularization, with no sign of inflammation or pathological neovascularization.

RPLM: reversed palmaris longus muscle; MN: median nerve; MSK-US: musculoskeletal ultrasound.

of the forearm. Additionally, examination of the contralateral left forearm in our patient showed a normal palmaris longus tendon. This case report aligns with recent trends positioning MSK-US as a technique of choice. Visualization of an ovoid, isoechoic muscular structure with a fibrillar pattern was possible by high spatial resolution. The use of color and power Doppler US together with real-time evaluation, allowed the exclusion of neoplasms by observing normal intrinsic vascularity. The dynamic capability of MSK-US, which permits observation of muscle thickening during contraction, is a diagnostic advantage that MRI does not offer.

The most common manifestation of RPLM is the appearance of an asymptomatic or slightly tender mass on the anterior aspect of the distal forearm or wrist. The radiologist may initially misinterpret this as a hemangioma, nerve sheath tumor, or soft-tissue tumor such as a lipoma, sarcoma or ganglion (synovial cyst), which, as reported in the literature, can lead to unnecessary surgical interventions[11]. The clinical peculiarity is that symptoms are often dynamic and related to physical exertion, as the space within the carpal canal or distal forearm is compromised by the additional volume of the muscle belly during activity[6]. Symptoms tend to worsen in individuals who perform repetitive upper-limb activities or contact sports. In these cases, RPLM hypertrophy or overuse-related inflammation increases space occupying effects, transforming a previously silent anatomical variant into a symptomatic condition that requires precise diagnostic evaluation to differentiate it from acute traumatic or inflammatory lesions[3]. RPLM may be asymptomatic, but muscle hypertrophy or intense exercise can trigger pain and neurovascular compression[3,4]. Our patient's symptoms, exacerbated by physical activity, highlight the mechanism of dynamic entrapment, in which muscle contraction increases distal belly volume, thereby raising compartment pressure. Precise identification of PLM variants does not require histological confirmation when an anatomical correlation is confirmed, suggesting that comparing the symptomatic forearm with the healthy contralateral side serves as an essential internal control[1,11]. Identifying a normal palmaris longus tendon on the opposite side or documenting muscular asymmetry reinforces the congenital and variant nature of the finding, effectively differentiating it from systemic or inflammatory processes[3,11]. Therefore, a systemic, bilateral MSK-US evaluation, combined with a clinical correlation, allows a conclusive diagnosis without resorting to MRI or biopsy.

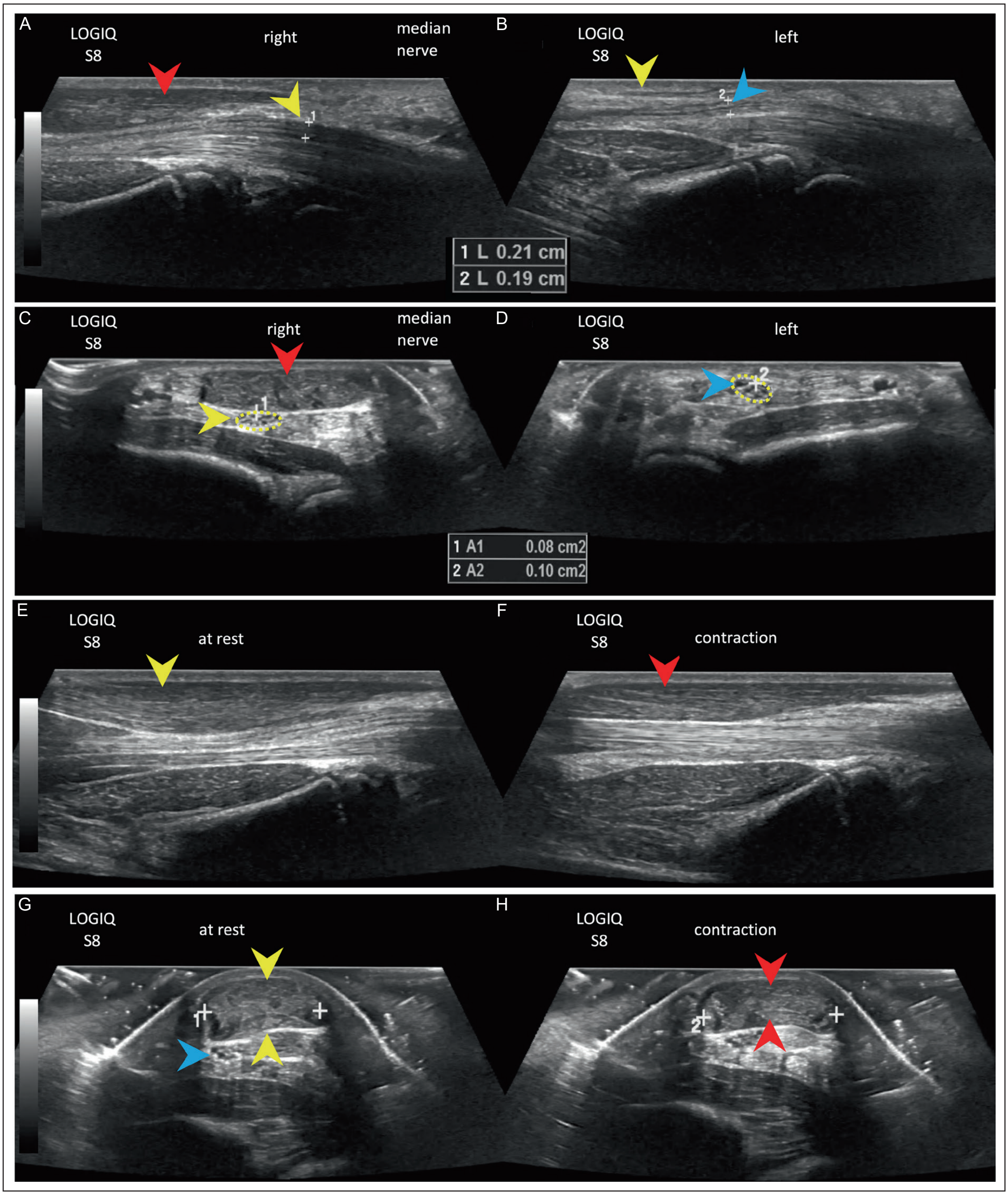

Figure 4. A 13-year-old boy with a painful palpable mass in the right distal forearm diagnosed with RPLM. **A:** grayscale MSK-US longitudinal shows the right-sided RPLM (red arrowhead) extending toward the carpal line over the MN (yellow arrowhead). The MN has an increased anteroposterior diameter of 0.21 cm. **B:** contralateral, left forearm, shows the MN with an anteroposterior diameter of 0.19 cm (blue arrowhead), normal palmaris longus tendon is shown (yellow arrowhead). **C:** grayscale MSK-US transverse of the middle third of the right RPLM (red arrowhead) compressing the MN (dotted circle). The cross-sectional area is 0.08 cm² (dotted line). **D:** grayscale transverse MSK-US of the left MN with an area of 0.10 cm² (dotted circle). **E:** grayscale longitudinal MSK-US of the RPLM at rest, showing muscle thickness (yellow arrowhead). **F:** grayscale longitudinal MSK-US of the RPLM during eccentric contraction, showing reduced muscle thickness (red arrowhead). **G:** grayscale transverse MSK-US of the RPLM at rest showing muscle thickness (yellow arrowheads) and MN compression (blue arrowhead). **H:** grayscale transverse MSK-US of the RPLM during eccentric contraction, confirming decreased muscle thickness (red arrowheads).

RPLM: reversed palmaris longus muscle; MN: median nerve; MSK-US: musculoskeletal ultrasound.

The radiologist must identify the key landmarks of the RPLM in the distal forearm. Once it is confirmed that the mass is isoechoic and maintains a typical fibrillar architecture of striated muscle, the need for a biopsy is eliminated, as this pattern is pathognomonic of an anatomical PLM variant[11].

CONCLUSION

In our case report, high-resolution MSK-US enabled an accurate, non-invasive diagnosis of a RPLM in a pediatric patient with a painful, palpable mass in the right distal forearm. Early identification helps prevent diagnostic errors and unnecessary invasive procedures, reinforcing MSK-US as a first-line imaging modality for soft tissue masses of the forearm due to its high spatial resolution, cost-effectiveness, and dynamic evaluation. This modality offers unique advantages for establishing a conclusive RPLM diagnosis.

Acknowledgment

We thank Professor Ana M. Contreras-Navarro for her guidance in preparing and writing this scientific paper.

Funding

The authors declare that they have not received funding.

Conflicts of interest

The authors declare no conflicts of interest.

Ethical considerations

Protection of human subjects and animals. The authors declare that the procedures followed were in accordance with the ethical standards of the responsible committee on human experimentation and with the World Medical Association and the Declaration of Helsinki (1964) and its amendments.

Confidentiality, informed consent, and ethical approval. The authors have obtained approval from the Ethics Committee for the analysis of routinely collected and anonymized clinical data; therefore, individual informed consent was not required. Relevant ethical recommendations have been followed.

Declaration on the use of artificial intelligence. The authors declare that no generative artificial intelligence was used in the writing or creation of the content of this manuscript.

REFERENCES

1. Andring N, Kennedy SA, Iannuzzi NP. Anomalous forearm muscles and their clinical relevance. J Hand Surg Glob. 2018;43(5):455-463. doi: 10.1016/j.jhsa.2018.02.028.
2. Al Risi AM, Al Busaidi S, Al Aufi H, Al Hashmi L, Sirasanagandla SR, Das S. Anatomical study of the palmaris longus muscle and its clinical importance. Diagnostics. 2025;15(3):304. doi: 10.3390/diagnostics15030304.
3. Longhurst G, Stone D, Mahony N. Bilateral reversed palmaris longus muscle: a case report and systematic literature review. Surg Radiol Anat. 2020;42(3):289-295. doi: 10.1007/s00276-019-02363-z.
4. Hashem M, Alatassi R, Narinder K, Emran F. Hypertrophied reversed palmaris longus muscle (pseudotumor) of the forearm causing median nerve compression: a case report. J Med Case Rep. 2020;14(1):60. doi: 10.1186/s13256-020-02368-y.
5. Regan P, Roberts J, Bailey B. Ulnar nerve compression caused by a reversed palmaris longus muscle. J Hand Surg Br. 1988;13(4):406-407. doi: 10.1016/0266-7681(88)90167-2.
6. Schuurman AH, Van Gils APG. Reversed palmaris longus muscle on MRI: report of four cases. Eur Radiol. 2000;10(8):1242-1244. doi: 10.1007/s003300000314.
7. Twoon M, Jones CD, Foley J, Davidson D. Reversed palmaris longus muscle: a report of two cases. Case Reports. Plast Surg Hand Surg. 2017;4(1):73-76. doi: 10.1080/23320885.2017.1353424.
8. Billone LM, Allred SJ, Flores DV. US of acute tendon tears. Radiographics. 2024;44(12):e240060. doi: 10.1148/rg.240060.
9. Ruiz F, Moyano S, Ruiz F. Claves para el diagnóstico ecográfico del músculo palmar largo invertido. Radiología. 2006;48(6):391-393. doi: 10.1016/s0033-8338(06)75155-4.
10. Yammine K. Clinical prevalence of palmaris longus agenesis: A systematic review and meta-analysis. Clin Anat. 2013;26(6):709-718. doi: 10.1002/ca.22289.
11. Martinoli C, Perez MM, Padua L, Valle M, Capaccio E, Altafini L, et al. Muscle variants of the upper and lower limb (with anatomical correlation). Semin Musculoskelet Radiol. 2010;14(2):106-121. doi: 10.1055/s-0030-1253155.

JMeXFRI

Journal of the Mexican Federation
of Radiology and Imaging

IMAGES IN RADIOLOGY

Imaging findings of undifferentiated squamous cell carcinoma in a patient with epidermolysis bullosa

*Adriana M. Ruiz-Delgado** and Gabriela M. Salinas-Moreno*

Department of Radiology and Imaging, Centro Universitario de Imagen Diagnostica, Hospital Universitario "Dr. Jose Eleuterio Gonzalez", Universidad Autonoma de Nuevo Leon, Monterrey, Nuevo Leon, Mexico

A 27-year-old woman with epidermolysis bullosa presented with a three-month history of a bleeding exophytic lesion on her left forearm. Physical examination revealed a large exophytic ulcerative lesion on the posterior surface of her left forearm and a "mitten" deformity, caused by flexion contracture and

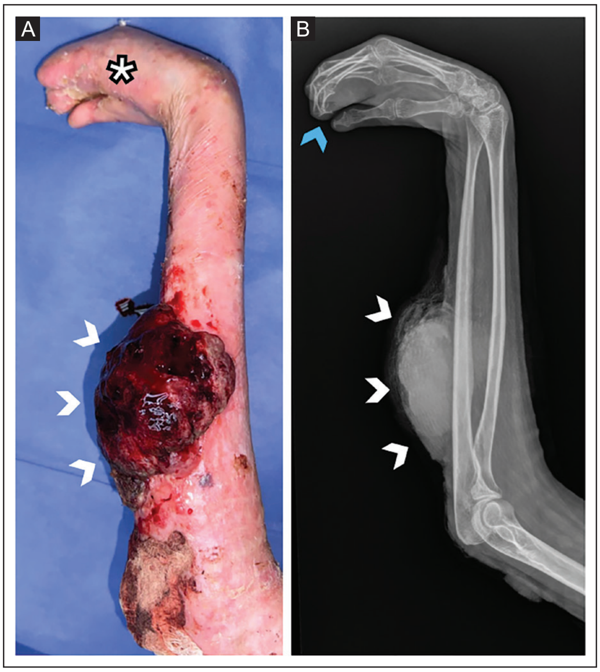

Figure 1. A 27-year-old woman with epidermolysis bullosa and a bleeding exophytic lesion on her left forearm. **A:** a clinical photograph of the posterior left forearm showing an exophytic lesion with active bleeding (white arrowheads). The hand exhibits a "mitten hand" deformity characteristic of epidermolysis bullosa (asterisk). **B:** a lateral X-ray of the forearm reveals a large, soft exophytic mass on the left posterior forearm with no bone involvement (white arrowheads). The hand deformity caused by flexion contracture and pseudosyndactyly gives the appearance of a "mitten hand," with hook-like distal phalangeal deformities (blue arrow).

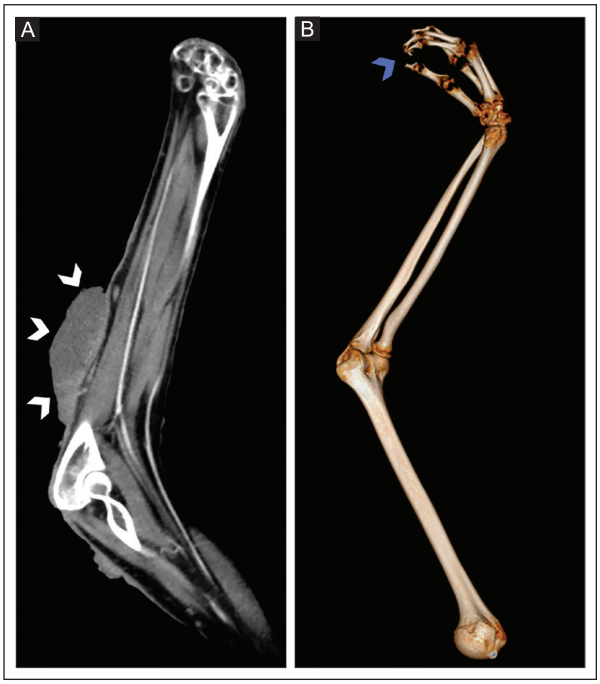

Figure 2. A 27-year-old woman with epidermolysis bullosa and a bleeding exophytic mass on her left forearm. **A:** a venous phase contrast-enhanced CT of the upper limb exhibits an irregular heterogeneous, predominantly hypodense exophytic lesion of the posterior forearm, with well-defined borders and no invasion of deep planes. Bone and muscle structures are preserved. The lesion is enhanced after contrast administration (white arrowheads). **B:** a 3D volume-rendered CT shows no deep plane invasion with preservation of bone and muscle, and a hook deformity of the distal phalanges (blue arrowhead). The histopathological diagnosis was undifferentiated squamous cell carcinoma.

CT: computed tomography.

***Corresponding author:**
Adriana M. Ruiz-Delgado
Email: mitsiruiz14@gmail.com

Received for publication: 02-10-2025
Accepted for publication: 18-11-2025
DOI: 10.24875/JMEXFRI.M26000120

Available online: 16-04-2026
J Mex Fed Radiol Imaging. 2026;5(1):81-82
www.JMeXFRI.com

pseudosyndactyly of the distal phalanges with a hook-like appearance (Figure 1). A lateral X-ray showed a large soft-tissue exophytic lesion on the posterior left forearm without bone involvement.

Venous phase contrast-enhanced computed tomography (CT) of the left upper limb shows a heterogeneous, with predominantly hypodense areas, well-defined borders of an irregular exophytic lesion on the posterior forearm (Figure 2). The lesion showed enhancement after contrast administration, with no invasion of underlying bone or muscle. The histopathologic diagnosis was undifferentiated squamous cell carcinoma with acantholytic features and perineural invasion.

Squamous cell carcinoma is a long-term skin complication of scarred epidermolysis bullosa[1]. Some lesions are flat ulcers that invade subcutaneous tissue, with poorly defined deep tumor margins and peritumoral fat stranding. These features reflect the locally aggressive behavior of the lesion[2]. Imaging evaluation can begin with X-ray. CT findings show nonspecific soft tissue density. The risk of metastasis for squamous cell carcinoma in patients with epidermolysis bullosa is relatively low; therefore, routine imaging studies are not recommended[3].

Acknowledgements

The authors thank Professor Ana M. Contreras-Navarro for her guidance in preparing and writing this scientific paper.

Funding

The authors declare that they have not received funding.

Conflicts of interest

The authors declare no conflicts of interest.

Ethical considerations

Protection of human subjects and animals. The authors declare that the procedures followed were in accordance with the ethical standards of the responsible committee on human experimentation and with the World Medical Association and the Declaration of Helsinki (1964) and its subsequent amendments.

Confidentiality, informed consent, and ethical approval. The authors have obtained approval from the Ethics Committee for the analysis of routinely collected and anonymized clinical data; therefore, individual informed consent was not required. Relevant ethical recommendations have been followed.

Declaration on the use of artificial intelligence. The authors declare that no generative artificial intelligence was used in the writing or creation of the content of this manuscript.

REFERENCES

1. McGrath JA, Schofield OM, Mayou BJ, McKee PH, Eady RA. Epidermolysis bullosa complicated by squamous cell carcinoma: report of 10 cases. J Cutan Pathol. 1992;19(2):116-123. doi: j.1600-0560.1992.tb01352.x.
2. Kawaguchi M, Kato H, Noda Y, Kobayashi K, Miyazaki T, Hyodo F, et al. Imaging findings of malignant skin tumors: radiological-pathological correlation. Insights Imaging. 2022;13(1):52. doi: 10.1186/s13244-022-01205-8.
3. Bander TS, Nehal KS, Lee EH. Cutaneous squamous cell carcinoma: Updates in staging and management. Dermatol Clin. 2019;37(3):241-251. doi: 10.1016/j.det.2019.03.009.

PHILIPS

Ultrasound

Affiniti

Designed for your everyday

Stepping up to today's Philips Affiniti Ultrasound System means stepping up to the next level of performance to help with a confident diagnosis using streamlined workflow.

Upgrade to the latest Affiniti capabilities

Intuitive use

Experience a user interface and workflow that helps increase your productivity.

- Enhances user workflow with **system-guided protocols** that can be easily customized to suit your needs
- **Tablet-like 30.48 cm (12 in) touchscreen** with workflow-related controls for ease of use
- **Next Gen AutoSCAN reduces button pushes by up to 54%** with pixel-by-pixel real-time optimization and reduces the need for user adjustment while also enhancing transducer plunkability.*
- At just 83.5 kg (184 lb), the system is **16% lighter** than its predecessor system**
- **Shared transducer family** across Affiniti and Compact 5000*** series systems helps maximize your investment
- **Wireless networking** aids workflow

Battery backup with sleep mode allows the system to **sleep in 2 seconds and return to full functionality in 20 seconds**

Consumes nearly 40% less power compared to our legacy predecessor system*

---

* When comparing VM10 performance to VM7.
** HD15.
*** R.S. #1437E2024 SSA.

Intelligent imaging

Flow Viewer

Defines vasculature with a 3D-like appearance using both the velocity and power of the Doppler signal to accurately represent vascular flow topography

MicroFlow Imaging (MFI)

Provides remarkable sensitivity and detail in assessing blood flow

Find out more at

www.philips.com.mx/healthcare/solutions/ultrasound

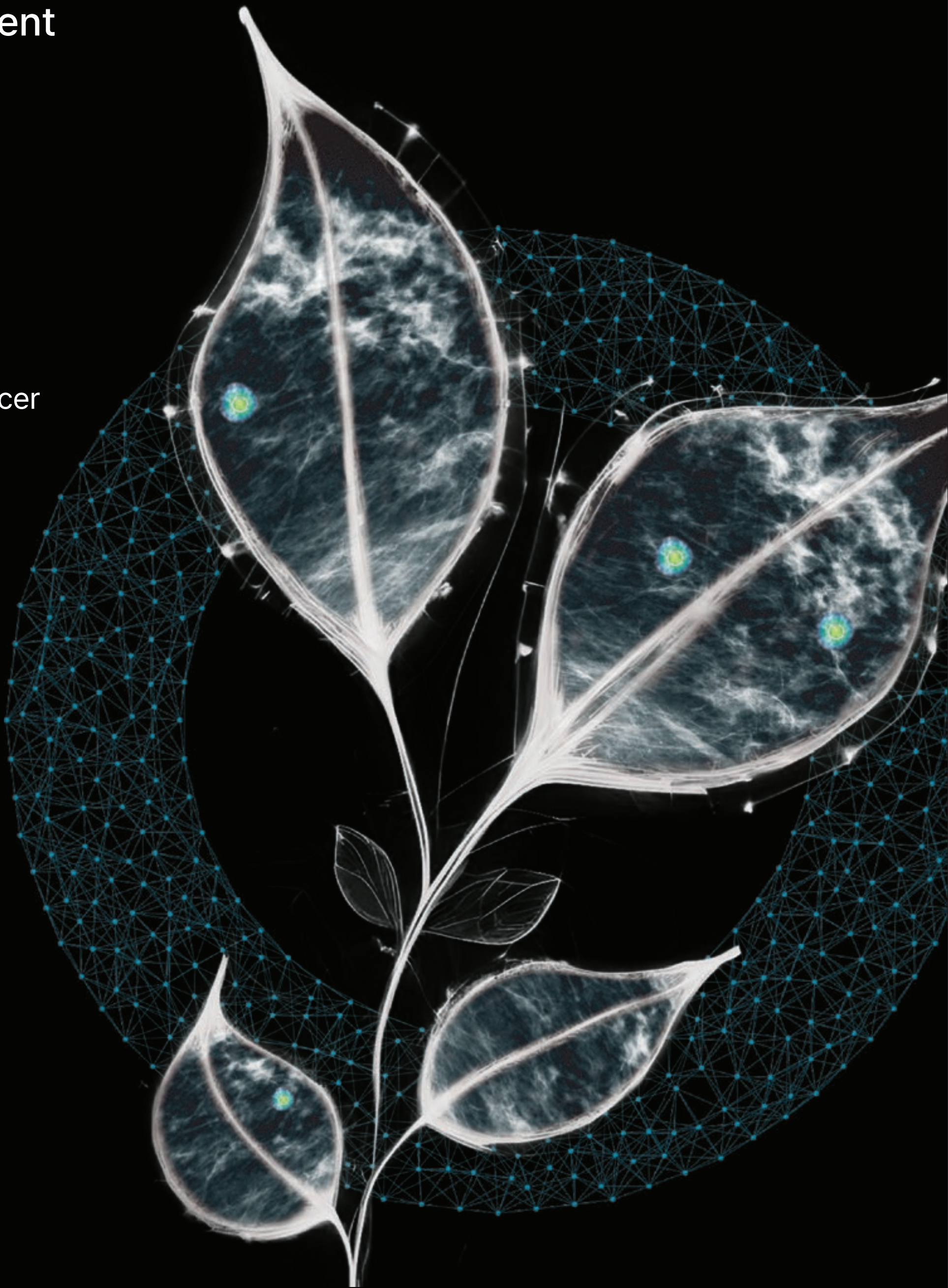

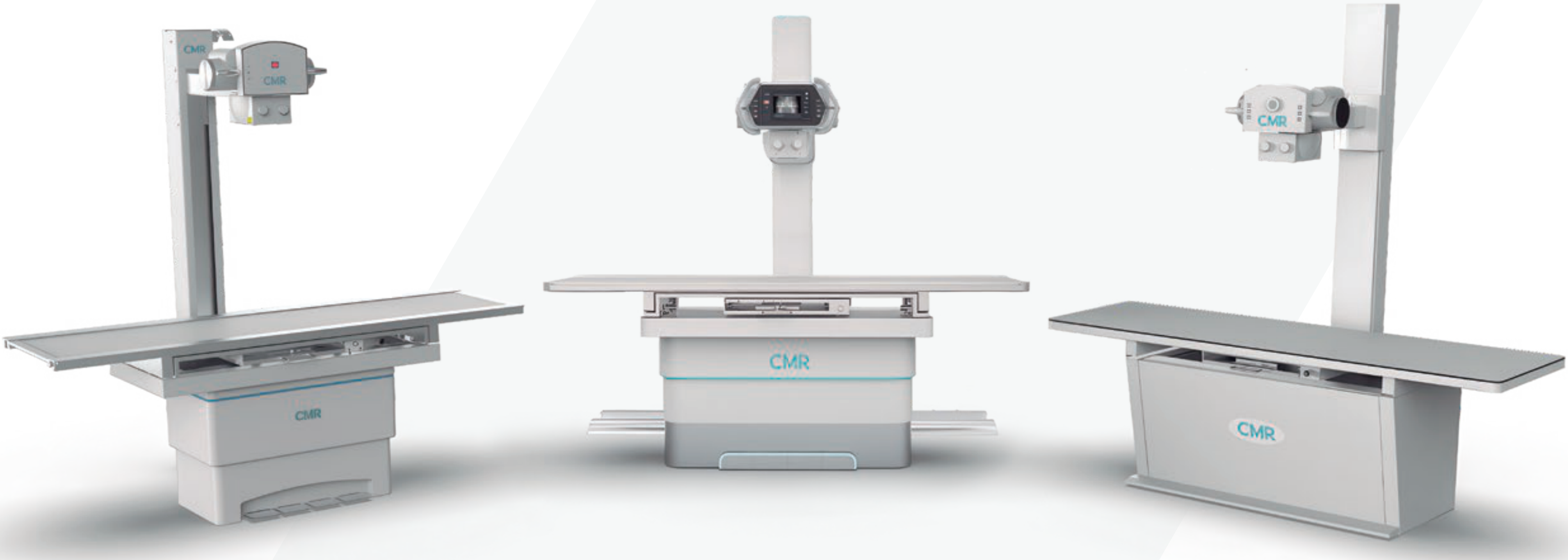
CMR
CMR
CMR
CMR
CMR
CMR

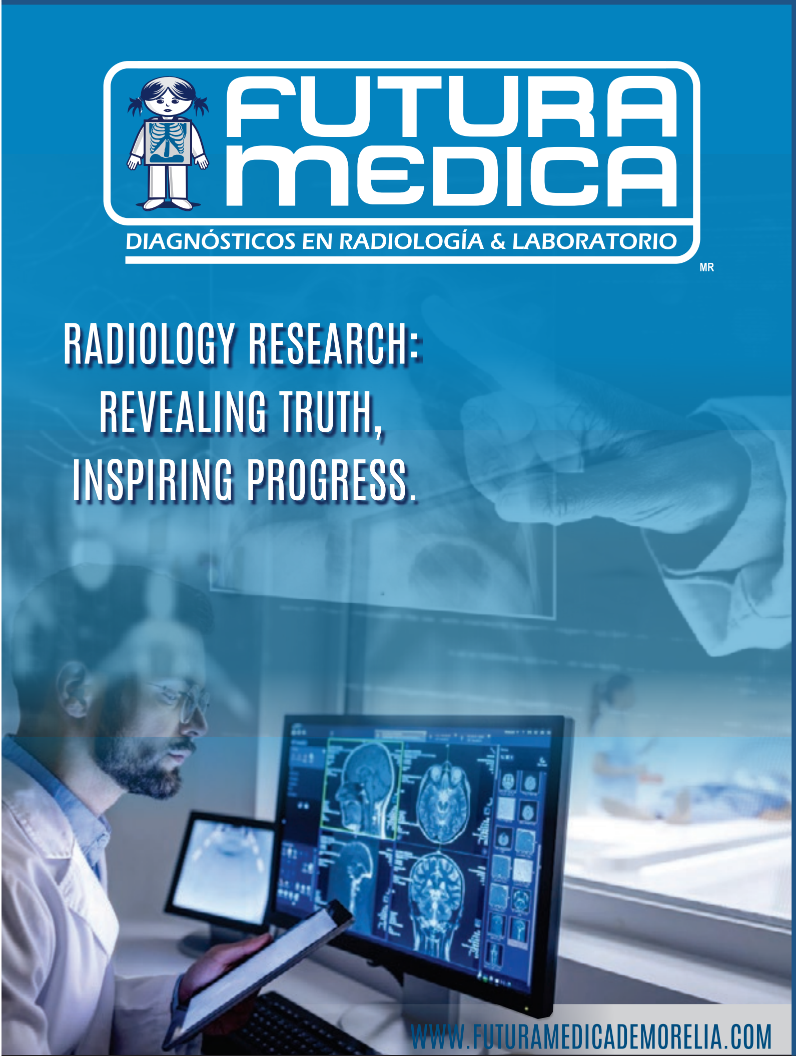
FUTURA
MEDICA
DIAGNÓSTICOS EN RADIOLOGÍA & LABORATORIO
MR
RADIOLOGY RESEARCH:
REVEALING TRUTH,
INSPIRING PROGRESS.
WWW.FUTURAMEDICADEMORELIA.COM